UNIVERSITÀ DEGLI STUDI DI SALERNO

DIPARTIMENTO DI INGEGNERIA CIVILE

Dottorato di Ricerca in Ingegneria delle Strutture e del Recupero Edilizio ed Urbano

XIV Ciclo N.S. (2013-2015)

INNOVATIVE GFRP SECTIONS SHAPE AND PROPORTIONS IN CIVIL ENGINEERING STRUCTURES

Marco Lamberti

Tutor
Prof. Francesco Ascione

Coordinatore
Prof. Ciro Faella

Co-Tutor
Prof. Luciano Feo

Who overcomes crisis, overcomes himself, without getting overcome…

A.E.

ACKNOLWLEDGEMENTS

I would like to express my highest gratitude to my academic tutor and mentor, Professor Francesco Ascione.
He guided me during my p.h.d. course with unlimited availability and cordiality.
I look forward to collaborating with him on future research projects.
A special thanks I would like to express to Professor Luigi Ascione whose advices and knowledge during this investigation were fundamental.
I am grateful to my co-tutor Professors Luciano Feo precious guide that have enriched and enhanced my thesis. His devotion to work and to research has been of great inspiration for me.
I would also like to thank Professor Geminiano Mancusi whose advices and support during this research were essential.
Another thanks I would to say to Professor Frèdèric Lebon and Aurelien Maurel Pantel. Thanks for giving me the opportunity to spend three wonderful months at Laboratory of Mechanics and Acoustics of CNRS in Marseille.
An important thanks goes to Professor Ghani Razaqpur. Working with him it was a brillant opportunity to improve myself.

INDEX

LIST OF FIGURES

INTRODUCTION

PART I: THE MECHANICAL BEHAVIOUR OF GFRP PULTRUDED BEAMS IN THE LATERAL BUCKLING EQUILIBRIUM PROBLEM

CHAPTER I: AN INNOVATIVE MECHANICAL APPROACH FOR STUDYING GFRP PULTRUDED BEAMS

CHAPTER II: INFLUENCE OF WEB/FLANGE CONNECTION IN THE LATERAL-TORSIONAL BUCKLING PROBLEM

CHAPTER III: MODIFICATIONS OF STANDARD GFRP SECTIONS SHAPE AND PROPORTIONS FOR IMPROVED STIFFNESS AND LATERAL-TORSIONAL STABILITY

PART II: NEW GFRP PULTRUDED BEAMS

CHAPTER IV: GFRP BEAMS OBTAINED BY BONDING SIMPLE PANELS: THE I CROSS SECTION CASE

APPENDIX A

LIST OF TABLES

CHAPTER III: MODIFICATIONS OF STANDARD GFRP SECTIONS SHAPE AND PROPORTIONS FOR IMPROVED STIFFNESS AND LATERAL-TORSIONAL STABILITY

PART II: NEW GFRP PULTRUDED BEAMS

CHAPTER IV: GFRP BEAMS OBTAINED BY BONDING SIMPLE PANELS: THE I CROSS SECTION CASE

CHAPTER V: DIFFERENT SHAPES OF THE WEB/FLANGE REINFORCEMENT IN PULTRUDED "BONDED" BEAMS

APPENDIX A

INTRODUCTION

Although traditional materials (steel, concrete, timber and masonry) still dominate the building industry, new materials are constantly being explored by engineers and scientists. For instance, the use of the so-called FRPs (Fibre-Reinforced Polymers) is gradually spreading worldwide [1-4].
The main idea of FRPs is the combination, on a macroscopic scale, of two different long continuous fibres and a polymeric resin. More specifically, high strength fibres (glass, carbon, aramid or ultra-thin steel wires) provide strength and stiffness while the resin (polyester, vinylester or epoxy) protects the fibres and guarantees the stress transfer between them. As a result, enhanced final properties are obtained with respect to those exhibited by the individual constituents.
Among several type of fibers, Glass Fibre Reinforced Polymers (GFRP) are widely used due to their relatively low cost, although glass fibres exhibit much lower elastic modulus and ultimate strength than carbon fibres. In addition, some additional issues emerge with regard to durability in alkaline environments and long-term response under sustained stresses. FRP pultruded beams take advantage of their principal features [5-6].
Since the late 1990s, among the FRPs elements, those frequently used in civil engineering are the pultruded ones.
They are obtained by the pultrusion process that make possible to produce such profiles with both closed or open cross sections; the only limitation is that the same cross section is required over the length.
Pultruded profiles reinforced with glass fibers (GFRP) present many advantages, including very high stiffness and strength to weight ratios, magnetic transparency, corrosion resistance, and an effective manufacturing process.

For these features they can be qualified as non-corrosive, high mechanical strength and lightweight materials.

In the last few years, they have been used in several different civil structures, acquiring a relevant role as primary bearing structural elements for applications such as cables, stands, truss members, footbridges, boardwalks, high voltage electricity poles, small buildings and emergency-oriented solutions [7-9].

Examples of relevant structures consisting of FRP profiles include a number of bridges and footbridges, where both open and closed shapes are usually used. Examples are I-, L-, H- and tubular profiles.

The first applications of FRP were recorded in China at the beginning of 80's. Nowadays in this Country it can be counted numerous bridges made from fiber reinforced composite materials, among them the most important are the Miyun Bridge in Beijing [Fig.1] and the Xiangyong Bridge recently built in Chengdu.

Figure 1. The Composite "Miyun Bridge" in Beijing, China.

The same is happened in the U.S.A. where the most important bridge realized are the Tom's Creek Bridge (1996) [Fig.2], the Clear Creek Bridge

(1996) [Fig.3], the Laurel lick Bridge (1997), the Wickwire Run Bridge (1997), the Bentley Creek Bridge (2000) and the Deer Creek (2001).
In particular, in the bridge over Deer Creek in Maryland State, USA, the deck on a steel trough-truss bridge was replaced by FRP composite deck. The weight of the new deck was about 40% less than a conventional concrete deck, resulting in increased live load capacity for the bridge [Fig.4].
Advanced applications of FRP composite tubes can be found also in North America, where hybrid configurations of FRP/lightweight concrete have been proposed for arch members. Furthermore, composite piles have also been proposed for marine installations.

Figure 2. The Composite "Tom's Creek" Bridge in U.S.A.

Figure 3. The Composite "Clear Creek" Bridge in U.S.A.

Figure 4. The bridge over Deer Creek; Maryland State, U.S.A.

In Europe the first application of structures in fiber reinforced material was realized by means an innovative systems through in the United Kingdom and called ACCS (Advanced Composite Construction System). The ACCS

developed by Maunsells Structural Plastic Ltd is an example of connection method, in which plank units (multi-cellular box sections) are assembled by sliding a toggle section into the groove of each panel. The most important structures are some bridges in Scotland, in Galles and England, in particular the Aberfeldy Bridge (1992), [Fig.5] the Bonds Mill Lift Bridge (1992) [Fig.6], the Bromley South Bridge (1992) and the Parson's Bridge (1995).

The Aberfeldy Bridge was the first suspension bridge realized completely of composite materials: the deck and the columns are realized with the ACCS systems while the rods are made by Aramid fiber (Kevlar)[10].

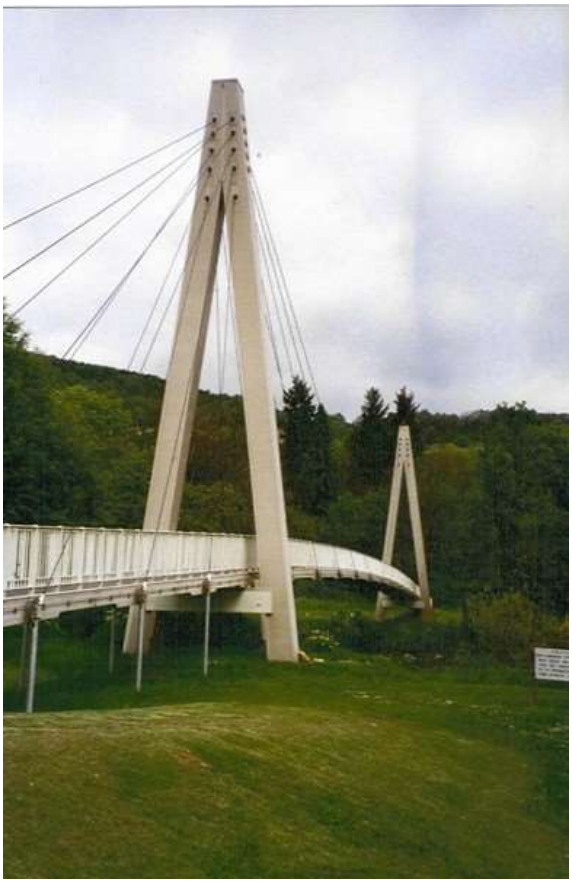

Figure 5. The Composite "Aberfeldy Bridge" Bridge in Scotland, U.K.

Figure 6. The Composite "Bonds Mill Lift" Bridge in Gloucestershire, U.K.

It is impossible not remember the pedestrian Fiberline Bridge in Kolding, Denmark, open on 18 June, 1997 as the first composite bridge in Scandinavia. The Fiberline pedestrian and cyclist bridge was the first of its kind to cross a railway line. The busy railway line restricted installation work to only a few hours during nights. The short installation time has illustrated the clear advantages of composites [Fig. 7].

Figure 7. The Fiberline All-Pultruded Composites Cable Stayed; Kolding, Denmark.

Another important application is the composite pedestrian bridge Ooypoort that was officially opened in Nijmegen, the Netherlands. The bridge structure consists purely of glass fiber-reinforced polyester. With its span of 56m it is among the longest single-span composite bridges in the world [Fig.8].

Figure 8. The Composite "Ooypoort" pedestrian Bridge in Nijmegen, Netherlands.

Meaningful is the 38 m span Lleida Footbridge in Spain, consisting of a double-tied arch crossing an existing roadway and a high-speed railway line. The arches and the tied longitudinal bridge deck girders were made of a rectangular hollow FRP cross-section obtained from two U-profiles joined together with two bonded flat plates to form the rectangular tubular section [Fig. 9].

Figure 9. Lleida Footbridge in Spain.

Other relevant applications of composite material in the Civil Engineering regarded some experimental building.
The first buildings made from FRP profiles were single-storey gable frames used in the electronics industry for Electromagnetic Interference (EMI) test laboratories.
Two important examples are the Compaq Computer Corporation and the Apple Computer building in California. In both cases the choice was motivated by the need to avoid possible interference between the internal and external electromagnetic fields.
One of the most famous, full-composite structures was the five-storey GFRP Eyecatcher Building erected in Basel, Switzerland in 1998 for the Swiss Building Fair. It is also the tallest FRP structure constructed until now [Fig. 10].

Figure 10. The All-Composite "Eyecatcher" Building in Switzerland.

In all these structures, pultruded profiles were not used in their original shape but were joined together to form more complex cross-sections, not available on the market.

In fact, in order to make pultruded members more appealing to the construction industry, most manufacturers produce profiles that imitate standard structural steel members (e.g. I-, H-, C-, and angle profiles), but in the field of composite research, the belief that these "steel-like" profiles do not represent the optimum geometry for composite sections is gradually gaining currency. Considering that standard engineering guidelines developed for conventional materials are not applicable to FRP shapes, several technical documents dealing with the design equations and methods, material properties, and safety factors for pultruded elements have been developed or under development.

Starting from the EuroComp Design Code and Handbook [11], published in 1996, that provided, for the first time, an independent, practical guidance on structural design of polymer composites.
Following in 2002, the EN 13706 standard [12] defined two different classes of materials, associated with minimum values of material properties and although provides many specifications for pultruded profiles, no design guidance was provided in this document.
In 2007, the Italian National Research Council (CNR) published the first Italian design guide (DT 205/2007) for the design and construction of structures made of FRP pultruded elements [13] which is not a binding regulations and is still rather incomplete.
In 2011, the Construction Institute of the American Society of Civil Engineers (ASCE) published the Manuals of Practice (MOP) #102 for the design of FRP composite connections [14]. This manual covers major issues related to the analysis and design of composite joints and frame connections manufactured from fibre-reinforced polymer composites in general and pultruded composites in particular. Currently, a joint effort between the Pultrusion Industry Council (PIC) and the ASCE Structure Institute for developing American Standards for PFRP structures is underway and will be published in the near future.
Finally, the Technical Committee 250 of CEN (Comité Européen de Normalization), responsible for the structural Eurocodes, appointed a specific Working Group (WG4: Fibre Reinforced Polymer Structures) to draw up a scientific and technical report on the design and verification of full composite structures. The report, recently published, represents the first step toward a Structural Eurocode on this subject and his main goal is to stimulate the debate about the topic of full composite structures.
The actual state of knowledge allowed WG4 to give answers to many questions relating to the design and verification of FRP structures.
In all these documents, the pultruded elements could be considered as linear elastic, homogeneous, and transversely isotropic in the case of

aligned fibers, with the plane of isotropy being normal to the longitudinal axis (i.e. the axis of pultrusion) [15].

It is has been assessed that the mechanical behavior, especially in the case of open profiles, is highly affected by warping strains [16-17]. Moreover, the low values of the shear moduli (more or less the same as those of polymeric resin), coupled with their time dependency, can provoke non-negligible increases in lateral deflections, thus affecting both the local and global buckling loads. In particular, a long slender beam under bending about the strong axis may buckle through combined twisting and lateral bending of the cross section, a phenomenon known as flexural–torsional buckling.

As a consequence, FRP members exhibit complex behavior related to the multi-interaction between shear deformability, warping, non-uniform torsional rigidity and creep.

Furthermore the low elastic moduli make often design for serviceability and stability the governing limit states and they inhibit taking greater advantage of the high strength of FRP.

In order to ensure the structural reliability of load bearing pultruded composite members, the shape and fibre architecture of PFRP profiles must be optimized and designed properly.

Because the industrial process is optimized for mass pultrusion of a limited number of shapes, it is difficult to produce complex shapes with standard cost targets.

As a consequence, these unconventional cross-sections represent a critical point relative to the mechanical response in terms of buckling, deformability and adhesive layer resistance of such elements.

The first objective of the present thesis was to develop an innovative mechanical model in order to study the behavior of pultruded elements with complex (not conventional) cross section shapes able to take into account for the shear deformability, the warping effects and the possible discontinuities at the web/flange connections.

The above introduced model was translate into a finite element code which results, in terms of possible new cross section shapes and their mechanical response are reported in Part I of the present document.
The best technique to join together two GFRP profiles is without doubts the adhesion.
This choice is motivated by the fact that bonding technology permits to reduce the cost and the weight of structures as well as to limit high stress concentrations, typical of bolted joints, due to the presence of several holes. Furthermore, under this point of view, the bonding technique represent an excellent instrument in order to obtain complex shape in FRP material.
Although the bonding technique is nowdays a custom, relative to the bonding of pultruded plates and/or to the bonding of pultruded lamina to concrete, mansonry and steel substrates [18-24], there is a lack of knowledge with respect to bonding together two pultruded profiles to form more complex shapes. This lack of confidence has inspired the second object of present research, focused on the possibility of achieving a GFRP profile with a complex cross-sectional shape, not available on the market with a cost lower then the pultrusion process, by bonding an appropriate number of simple pultruded plates with a common epoxy glue.
Substantially, the idea is to identify a design strategy based on modularity.
For example, a generic I-profile may be obtained by bonding three rectangular panels (the top/bottom flanges and the web panel), rather than via a unique pultrusion application.
In order to achieve this second purpose a comprehensive experimental campaign was developed followed by a wide numerical analysis.
The results are reported in the Part II of the present document.

Finally, the outline of the thesis is the following one in which two parts have been individuated and several chapters at each of them:

PART I - THE MECHANICAL BEHAVIOUR OF GFRP PULTRUDED BEAMS IN THE LATERAL BUCKLING EQUILIBRIUM PROBLEM

> **CHAPTER I** - An Innovative mechanical approach for studying GFRP pultruded beams;
> **CHAPTER II** - Influence of Web/Flange connection in the Lateral-Torsional buckling problem;
> **CHAPTER III** - Modifications of Standard GFRP Sections Shape and Proportions for Improved Stiffness and Lateral-Torsional Stability;

PART II – NEW GFRP PULTRUDED BEAMS

> **CHAPTER IV** - GFRP beams obtained by bonding simple panels: the I- Cross Section Case;
> **CHAPTER V** - Different shapes of the web/flange reinforcement in pultruded "bonded" beams.

The topic related to the Part I and Part II were developed in collaboration with professor Ghani Razaqpur of McMaster University in Hamilton (Canada) and professor Frédéric Lebon of Aix Marseille University (Laboratory of Mechanics and Acoustics of CNRS) in Marseille (France).

PART I

THE MECHANICAL BEHAVIOUR OF GFRP PULTRUDED BEAMS IN THE LATERAL BUCKLING EQUILIBRIUM PROBLEM

Object of the research showed in this Part I was to improve the mechanical behavior of composite beams reinforced with glass fibers against flexural-torsional stresses through the introduction of innovative geometric cross sections shapes.

Within this line of research, the study was divided into three chapters. The aim of the Chapter I to develop a mechanical as well as a practical approach to predicting the nonlinear pre-buckling behavior of generic composite beams with complex open or closed cross sections.

In the Chapter II the Influence of Web/Flange connection in the Lateral-Torsional buckling problem was investigated.

Finally, the aim in the Chapter III was devote to identify, via detailed analysis, appropriate geometric parameters for GFRP sections that can be judiciously selected to improve their overall resistance, stability and serviceability when subjected to axial–flexural–torsional actions. The improvements can be judged by comparing the response of the GFRP sections with enhanced properties to those of similar existing sections available commercially.

The topic related to the Part I was developed in collaboration with Professor Ghani Razaqpur of McMaster University in Hamilton (Canada).

CHAPTER I

AN INNOVATIVE MECHANICAL APPROACH FOR STUDYING GFRP PULTRUDED BEAMS

1. INTRODUCTION

In this Chapter a geometrically nonlinear model for studying the lateral global buckling problem of a complex thin-walled composite beam is presented. The model is based on full second-order deformable beam theory and accounts for axial, flexural, shear, torsional and warping displacements.

The complex cross section can be obtained by an appropriate number of simple rectangular panel interconnected each other by means of springs.

This peculiarity of the present model permits to study the mechanical behavior of complex FRP beams obtained joining rectangular pultruded plates by means of an adhesive layer.

Moreover, the web/flange junctions can be supposed to be deformable.

Governing nonlinear equations are derived from the principle of virtual displacements. Comparisons with numerical and experimental results available in the literature are also discussed.

1.1 STATE OF THE ART ON THE LATERAL BUCKLING PROBLEM

The lateral buckling behavior of FRP beams has been widely investigated in the literature from theoretical, numerical, and experimental points of view. The first study on thin-walled open/closed sections was developed by Vlasov [25] and Gjelsvik [26], who limited their investigations to the field of isotropic materials. Three years later, Bauld and Tzeng [27] extended Vlasov's thin-walled beam theory. They developed linear and nonlinear theories for the bending and twisting of thin-walled composite beams. Twelve years later, Davalos et al. [28], from both an experimental perspective and a numerical point of view, studied the bending response of pultruded composite beams with different I and box sections.

Ascione L. et al. [29] and Feo and Mancusi [30] examined the static behavior of FRP thin-walled beams taking into account the effects of shear deformations. These studies present many comparisons with Vlasov's classical solution. The flexural–torsional behavior of I-section composite beams has recently been analyzed by Lee and Lee [31], who developed a one-dimensional finite element model specifically dedicated to this topic. More recently, Vo and Lee [32] developed an analytical study of thin-walled composite box beams subjected to vertical and torsional loads. Their model was based on a first-order shear-deformation beam theory and accounted for an arbitrary stacking sequence configuration. The same authors, two years later, developed a geometrically nonlinear model for thin-walled composite beams with arbitrary lay-ups under various loading configurations [33].

Recently, Mancusi and Feo [34] investigated the nonlinear pre-buckling behavior of thin-walled composite beams considering both the shear deformability and second-order displacement field formulation. The proposed approach highlights how relevant it is to account for the coupling between shear deformations and nonlinear kinematics. On the same topic, Ascione L. et al. investigated the local and global buckling of glass FRP I-beams by using the mechanical approaches presented in [35–37].

1.2 KINEMATICS

Two coordinate systems which are mutually interrelated are introduced: i) the global orthogonal system (x, y, z) shown in Figure 1.1 a, with *x* and *y* axes lying in the plane of the cross section while *z* is aligned to the longitudinal axis of the beam; ii) the local coordinate system (n, s, z) shown in Figure 1.1 b, with *n* being normal to the middle line and *s* being tangential to the middle of the cross section. As can be seen, the local and global systems can be superimposed on each other.

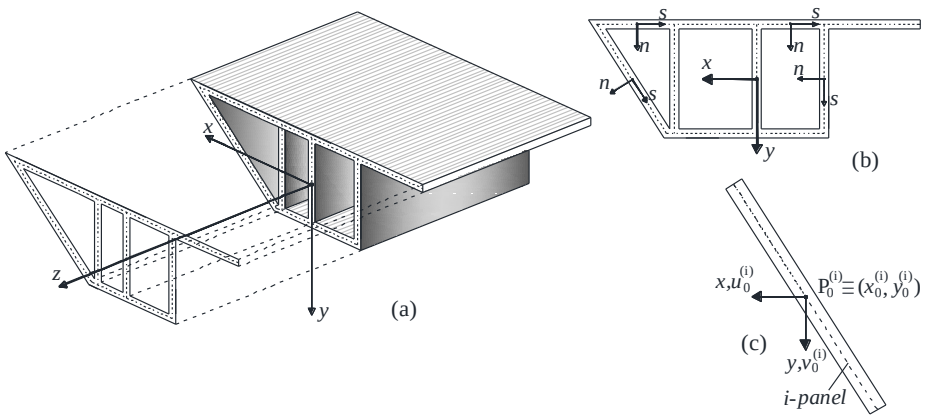

Figure 1.1. Generic beam (a); cross section (b); generic *i*-panel (c).

As above mentioned, the thin-walled beam is composed of a defined number of thin panels (rectangles) interconnected to each other (Figure 1.1). Let *N* be this number. The generic *i*-panel ($1 \le i \le N$) is modeled according to a full second-order deformable beam theory, accounting for both the warping effects and possible displacement discontinuities at the web/flange nodes. This last point will be discussed in detail in the following sections.

With reference to the generic *i*-panel, the displacement field is given by the following equations:

$$u^{(i)}(x,y,z) = u_o^{(i)}(z) - \varphi_3^{(i)}(z)\left(y - y_o^{(i)}\right) \tag{1.1.a}$$

$$v^{(i)}(x,y,z) = v_o^{(i)}(z) + \varphi_3^{(i)}(z)\left(x - x_0^{(i)}\right) \tag{1.1.b}$$

$$w^{(i)}(x,y,z) = \overline{w}_h^{(i)}(z)\, f_h^{(i)}(s) - \varphi_s^{(i)}(z)\, n \tag{1.1.c}$$

In Eqs. (1.a–c) the symbols $u_o^{(i)}$ and $v_o^{(i)}$ represent the displacement components of the point $P_o^{(i)} \equiv \left(x_0^{(i)}, y_0^{(i)}\right)$ along the *x* and *y* axes, respectively (Figure 1.1c); usually this point coincides with the centroid of the panel. Furthermore, the symbol $\varphi_3^{(i)}$ denotes the twisting rotation of the panel. In Eq. (1.1.c) the displacement component $w^{(i)}$ (axial displacement) is modeled as the sum of two parts: the first is a linear combination of the kinematical unknowns $\overline{w}_h^{(i)}$, which represent the axial displacements of the defined points $P_h^{(i)}$ lying on the mid-line of the panel, with the interpolating polynomials $f_h^{(i)}$ depending on the curvilinear abscissa *s*; the second accounts for the flexural rotation, $\varphi_s^{(i)}$, around the mid-line of the panel being *n* the normal coordinate to the mid-line.
In brief, the kinematics of the generic panel is given by:

i) a rigid transformation of the cross section in its own plane;
ii) a flexural rotation around the mid-line;
iii) warping terms introduced as a function of the curvilinear abscissa. Due to the low thickness of the panel, no additional warping effects are considered out of the mid-line.

It is important to note that the maximum order of the polynomials $f_h^{(i)}$ is related to the number $M^{(i)}$ of the kinematical unknowns $\overline{w}_h^{(i)}$ fixed to simulate the warping effects ($1 \le h \le M^{(i)}$) on the generic panel.
As described in detail in Section 1.3 the generic connection between two panels is simulated by means of nonlinear springs.
Finally, as a feature, the proposed model allows very generic boundary conditions, which can deal with the entire cross section as well as with a single panel, to be simulated.

1.3 INTERNAL CONNECTIONS

Due to the low thickness, it is assumed that two generic panels can be connected at a defined point of their mid-lines. This requires establishing which points of the two mid-lines are linked to each other.
Let *i* and *j* be the indexes of these two panels. It is easy to represent the position of the internal connection by introducing two specific points, $P_h^{(i)}$ and $P_k^{(j)}$, lying on the mid-lines of the two panels ($1 \le h \le M^{(i)}, 1 \le k \le M^{(j)}$). This way of representing the internal connection is very general and helpful in order to simulate the behavior of a generic thin-walled profile.
In Figure 1.2, the approach proposed for the description of the internal connections has been exemplified. In particular, the example concerns a profile composed of four thin panels, interconnected via three internal nodes.

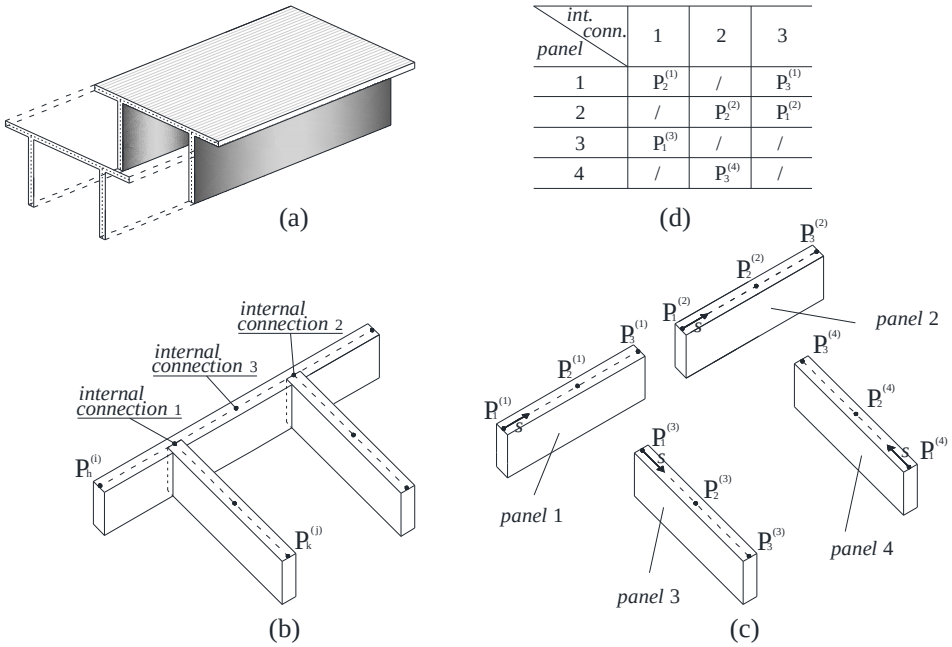

Figure 1.2. Generic open cross section (a); positions of the internal connections (b); axonometric exploded view (c); connections scheme (d).

The internal connections have been modeled by means of four nonlinear continuous distributions of springs, able to contrast the relative translational displacements and the relative rotation between two generic panels. The behavior of the internal connection has been modeled according to the relationship shown in Figure 1.3.

In more detail, the proposed approach generalizes the one already highlighted in [29], which is based on the experimental evidence presented by Mosallam et al. [38-39], and concerns the web/flange rotational stiffness only.

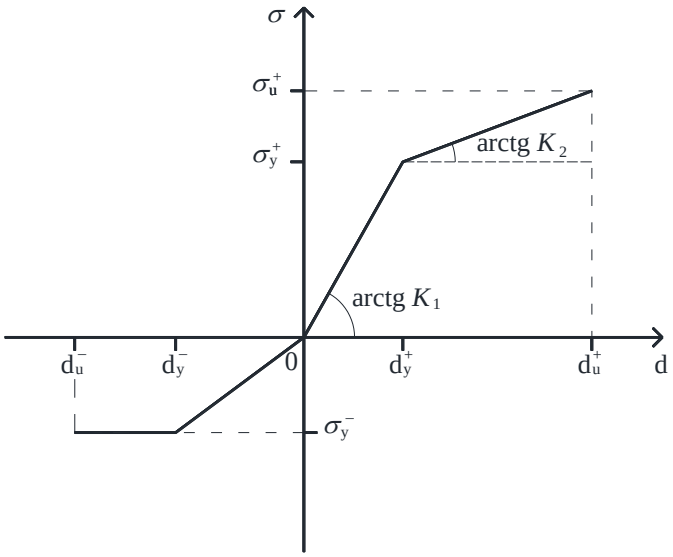

Figure 1.3. Generic relationship between web/flange discontinuities, d, and the corresponding interaction, σ.

The symbols introduced in Figure 1.3 assume the following meanings:

- σ is the generic interaction. Depending on the spring considered, this symbol represents the web/flange interaction per unit surface along the *x* axis (σ_u), the *y* axis (σ_v) and the *z* axis (σ_w) or the web/flange torsional interaction per unit length around the *z* axis (μ_3);
- d is the displacement discontinuity conjugated with σ; it represents the web/flange relative displacement along the *x* axis (d_u), the *y* axis (d_v) and the *z* axis (d_w) or the web/flange relative torsional rotation around *z* axis (d_{φ_3});

Further symbols, which depend on the sign of the discontinuity, are:

- σ_y the maximum elastic value of the considered web/flange interaction;
- σ_u the ultimate value of the considered web/flange interaction;
- d_y the maximum elastic value of the considered discontinuity;
- d_u the ultimate value of the considered discontinuity;
- K_1 the elastic stiffness parameter (tangent);
- K_2 the post-elastic stiffness parameter (tangent).

1.4 WARPING TERMS

As is easy to understand, the higher the number $M^{(i)}$ of points fixed on the mid-line of a generic i-panel, the better the accuracy of the warping simulation. In order to adequately simulate the warping behavior on the mid-line, it can be assumed that $M^{(i)} \geq 3$. This implies the need to introduce several points on the mid-line of the generic i-panel, including the two points placed at the ends of the panel itself. Moreover, the condition $M^{(i)} = 3$ ensures second-order interpolation accuracy; on the other hand, this also requires that at least an internal point is present on the mid-line of the i-panel. The following developments are derived by assuming $M^{(i)} = 3$ as a default choice.

Figure 1.4 indicates the notations adopted. It is assumed $P_1^{(i)} \equiv \left(x_1^{(i)}, y_1^{(i)}\right)$ and $P_3^{(i)} \equiv \left(x_3^{(i)}, y_3^{(i)}\right)$ are placed at the ends of the *i*-panel, while $P_2^{(i)} \equiv \left(x_2^{(i)}, y_2^{(i)}\right)$ is internal.

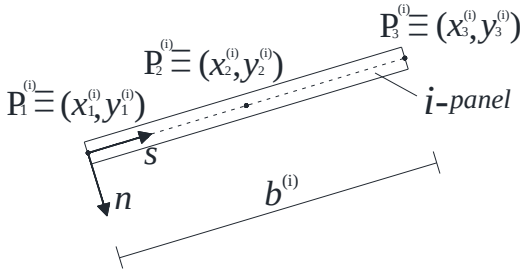

Figure 1.4. Generic *i*-panel.

It is important to underline that $P_1^{(i)}$ is assumed to be the origin of the curvilinear abscissa, *s*, on the mid-line of the *i*-panel. As a result, $0 \le s \le b^{(i)}$ where the following position exists:

$$b^{(i)} = \sqrt{\left(x_3^{(i)} - x_1^{(i)}\right)^2 + \left(y_3^{(i)} - y_1^{(i)}\right)^2} \tag{1.2}$$

Once the points $P_h^{(i)}$ ($h = 1, 2, 3$) have been fixed, it is easy to rewrite the warping term as follows:

$$\bar{w}_h^{(i)} f_h^{(i)} = \alpha^{(i)} + \beta^{(i)} s + \gamma^{(i)} s^2 \tag{1.3}$$

where

$$\alpha^{(i)} = \bar{w}_1^{(i)} \tag{1.4.a}$$

$$\beta^{(i)} = \frac{\left(\bar{w}_2^{(i)} - \bar{w}_1^{(i)}\right)\left(s_3^{(i)}\right)^2 - \left(\bar{w}_3^{(i)} - \bar{w}_1^{(i)}\right)\left(s_2^{(i)}\right)^2}{\Delta} \tag{1.4.b}$$

$$\gamma^{(i)} = \frac{-\left(\bar{w}_2^{(i)} - \bar{w}_1^{(i)}\right)\left(s_3^{(i)}\right) + \left(\bar{w}_3^{(i)} - \bar{w}_1^{(i)}\right)\left(s_2^{(i)}\right)}{\Delta} \tag{1.4.c}$$

In Eqs. (1.4a–c) the symbol Δ assumes the following expression:

$$\Delta = s_2^{(i)} \left(s_3^{(i)} \right)^2 - s_3^{(i)} \left(s_2^{(i)} \right)^2 \tag{1.5}$$

where $s_2^{(i)}$ and $s_3^{(i)}$ are the abscissas related to $P_2^{(i)}$ and $P_3^{(i)}$ respectively ($s_3^{(i)} = b^{(i)}$), while $\overline{w}_h^{(i)}$ ($h = 1, 2, 3$) indicates the axial displacement attained at the point $P_h^{(i)}$.

Via algebra it is possible to find the following expression of the axial displacements:

$$w^{(i)}(n, s, z) = \overline{w}_1^{(i)}(z)\, f_1^{(i)}(s) + \overline{w}_2^{(i)}(z)\, f_2^{(i)}(s) + \overline{w}_3^{(i)}(z)\, f_3^{(i)}(s) - \varphi_s^{(i)}(z) n \tag{1.6}$$

where:

$$f_1^{(i)} = 1 + a_1^{(i)} s + b_1^{(i)} s^2 \tag{1.7.a}$$

$$f_2^{(i)} = a_2^{(i)} s + b_2^{(i)} s^2 \tag{1.7.b}$$

$$f_3^{(i)} = a_3^{(i)} s + b_3^{(i)} s^2 \tag{1.7.c}$$

In Eqs. (1.7a–c) the quantities introduced assume the following meanings:

$$a_1^{(i)} = \frac{\left(s_2^{(i)}\right)^2 - \left(s_3^{(i)}\right)^2}{\Delta},\ b_1^{(i)} = \frac{s_3^{(i)} - s_2^{(i)}}{\Delta},\ a_2^{(i)} = \frac{\left(s_3^{(i)}\right)^2}{\Delta},\ b_2^{(i)} = -\frac{s_3^{(i)}}{\Delta},$$
$$a_3^{(i)} = -\frac{\left(s_2^{(i)}\right)^2}{\Delta},\ b_3^{(i)} = \frac{s_2^{(i)}}{\Delta}. \tag{1.8.a,f}$$

1.5 STRAINS

From Eqs. (1.1.a, b) and (1.6), it easy to express the components of the displacement gradient H with reference to the global axes (Figure 1.1a):

$$H_{11} = 0 \tag{1.9.a}$$

$$H_{12} = -\varphi_3^{(i)} \tag{1.9.b}$$

$$H_{13} = u_o'^{(i)} - \varphi_3'^{(i)}\left(y - y_o^{(i)}\right) \tag{1.9.c}$$

$$H_{21} = \varphi_3^{(i)} \tag{1.9.d}$$

$$H_{22} = 0 \tag{1.9.e}$$

$$H_{23} = v_o'^{(i)} + \varphi_3'^{(i)}\left(x - x_0^{(i)}\right) \tag{1.9.f}$$

$$H_{31} = \bar{w}_h^{(i)} g_{1,h}^{(i)}(s) - \varphi_s^{(i)}(z)\frac{dn}{dx} \tag{1.9.g}$$

$$H_{32} = \bar{w}_h^{(i)} g_{2,h}^{(i)}(s) - \varphi_s^{(i)}(z)\frac{dn}{dy} \tag{1.9.h}$$

$$H_{33} = \bar{w}_h'^{(i)} g_{3,h}^{(i)}(s) - \varphi_s'^{(i)}(z)n \tag{1.9.i}$$

where functions $g_{1,h}^{(i)}(s)$, $g_{2,h}^{(i)}(s)$ and $g_{3,h}^{(i)}(s)$ assume the following forms:

$$g_{1,h}^{(i)}(s) = \frac{\partial f_h^{(i)}}{\partial x} = a_h^{(i)}\frac{ds}{dx} + 2b_h^{(i)}\frac{ds}{dx} \tag{1.10.a}$$

$$g_{2,h}^{(i)}(s) = \frac{\partial f_h^{(i)}}{\partial y} = a_h^{(i)}\frac{ds}{dy} + 2b_h^{(i)}\frac{ds}{dy} \tag{1.10.b}$$

$$g_{3,h}^{(i)}(s) = f_h^{(i)}(s) \tag{1.10.c}$$

The Green strain tensor, E, is thereby:

$$\mathbf{E} = \begin{bmatrix} E_{11} & E_{12} & E_{13} \\ E_{12} & E_{22} & E_{23} \\ E_{13} & E_{23} & E_{33} \end{bmatrix} = \frac{1}{2}\left(\mathbf{H} + \mathbf{H}^{\mathrm{T}} + \mathbf{H}^{\mathrm{T}}\mathbf{H}\right) = \boldsymbol{\varepsilon} + \frac{1}{2}\mathbf{H}^{\mathrm{T}}\mathbf{H} \tag{1.11}$$

where $\boldsymbol{\varepsilon} = 1/2\left(\mathbf{H} + \mathbf{H}^T\right)$.

It is worth considering the following comments.

Despite E_{13}, E_{23} and E_{33} being expected to be the only non-trivial strain components, it emerges that so are $E_{11} \neq 0$, $E_{12} \neq 0$, and $E_{22} \neq 0$. This is due to the simplified form of the displacement field. Even if it is easy to satisfy the condition $E_{11} = E_{12} = E_{22} = 0$ via more general kinematic assumptions [34], the simplified kinematic Eqs. (1.1a–c) have been evaluated as appropriate for practical purposes. Without losing accuracy, the terms E_{11}, E_{12} and E_{22} can be ignored, thus reducing the only non-zero components of the Green–Lagrange strain tensor to the following:

$$E_{13} \cong \frac{1}{2}\left[u_0'^{(i)} - \varphi_3'^{(i)}\left(y - y_o^{(i)}\right) + \bar{w}_h^{(i)} g_{1,h}^{(i)} - \varphi_s^{(i)} \frac{dn}{dx} \right] + \frac{1}{2}\left[v_0'^{(i)} \varphi_3{}^{(i)} + \right. \tag{1.12.a}$$
$$\left. + \varphi_3{}^{(i)} \varphi_3'^{(i)}\left(x - x_o^{(i)}\right) + \bar{w}_h^{(i)} \bar{w}_k'^{(i)}\ g_{1,h}^{(i)}\ g_{3,k}^{(i)} \right]$$

$$E_{23} \cong \frac{1}{2}\left[v_0'^{(i)} + \varphi_3'^{(i)}\left(x - x_o^{(i)}\right) + \bar{w}_h^{(i)} g_{2,h}^{(i)} - \varphi_s^{(i)} \frac{dn}{dy} \right] + \frac{1}{2}\left[-u_0'^{(i)} \varphi_3{}^{(i)} + \right. \tag{1.12.b}$$
$$\left. + \varphi_3{}^{(i)} \varphi_3'^{(i)}\left(y - y_o^{(i)}\right) + \bar{w}_h^{(i)} \bar{w}_k'^{(i)} g_{2,h}^{(i)}\ g_{3,k}^{(i)} \right]$$

$$E_{33} \cong \left[\bar{w}_h'^{(i)} g_{3,h}^{(i)} - \varphi_s'^{(i)} n \right] + \frac{1}{2}\left\{ \left(u_0'^{(i)}\right)^2 + \left(v_0'^{(i)}\right)^2 + \left(\varphi_3'^{(i)}\right)^2 \left[\left(x - x_o^{(i)}\right)^2 + \left(y - y_o^{(i)}\right)^2 \right] + \right.$$
$$- 2u_0'^{(i)} \varphi_3'^{(i)}\left(y - y_o^{(i)}\right) + 2v_0'^{(i)} \varphi_3'^{(i)}\left(x - x_o^{(i)}\right) + \left(\bar{w}_h'^{(i)} g_{3,h}^{(i)}\right)^2 + \tag{1.12.c}$$
$$\left. + \left(1 - \delta_{hk}\right) \bar{w}_h'^{(i)} \bar{w}_k'^{(i)} g_{3,h}^{(i)}\ g_{3,k}^{(i)} \right\}$$

The final expression of the Green–Lagrange strain tensor and its first variation are thereby:

$$\mathbf{E} \cong \begin{bmatrix} 0 & 0 & E_{13} \\ 0 & 0 & E_{23} \\ E_{13} & E_{23} & E_{33} \end{bmatrix} \tag{1.13}$$

$$\delta\mathbf{E} = \frac{1}{2}\left(\delta\mathbf{H} + \delta\mathbf{H}^{\mathrm{T}} + \delta\mathbf{H}^{\mathrm{T}}\mathbf{H} + \mathbf{H}^{\mathrm{T}}\delta\mathbf{H}\right) \cong \begin{bmatrix} 0 & 0 & \delta E_{13} \\ 0 & 0 & \delta E_{23} \\ \delta E_{13} & \delta E_{23} & \delta E_{33} \end{bmatrix} \tag{1.14}$$

where:

$$\begin{aligned} \delta E_{13} \cong \frac{1}{2}\Bigg[& \delta u_0'^{(i)} - \delta\varphi_3'^{(i)}\left(y - y_o^{(i)}\right) + \delta\overline{w}_h^{(i)} g_{1,h}^{(i)} - \delta\varphi_s^{(i)}\frac{dn}{dx}\Bigg] + \frac{1}{2}\Big[\delta v_0'^{(i)}\varphi_3^{(i)} + v_0'^{(i)}\delta\varphi_3^{(i)} + \\ & + \delta\varphi_3^{(i)}\varphi_3'^{(i)}\left(x - x_o^{(i)}\right) + \varphi_3^{(i)}\delta\varphi_3'^{(i)}\left(x - x_o^{(i)}\right) + \left(\delta\overline{w}_h^{(i)}\overline{w}_k'^{(i)} + \delta\overline{w}_k'^{(i)}\overline{w}_h^{(i)}\right) g_{1,h}^{(i)}\, g_{3,k}^{(i)}\Big] \end{aligned} \tag{1.15.a}$$

$$\begin{aligned} \delta E_{23} \cong \frac{1}{2}\Bigg[& \delta v_0'^{(i)} + \delta\varphi_3'^{(i)}\left(x - x_o^{(i)}\right) + \delta\overline{w}_h^{(i)} g_{2,h}^{(i)} - \delta\varphi_s^{(i)}\frac{dn}{dy}\Bigg] + \frac{1}{2}\Big[-\delta u_0'^{(i)}\varphi_3^{(i)} + \\ & - u_0'^{(i)}\delta\varphi_3^{(i)} + \delta\varphi_3^{(i)}\varphi_3'^{(i)}\left(y - y_o^{(i)}\right) + \varphi_3^{(i)}\delta\varphi_3'^{(i)}\left(y - y_o^{(i)}\right) + \\ & + \left(\delta\overline{w}_h^{(i)}\overline{w}_k'^{(i)} + \delta\overline{w}_k'^{(i)}\overline{w}_h^{(i)}\right) g_{2,h}^{(i)}\, g_{3,k}^{(i)}\Big] \end{aligned} \tag{1.15.b}$$

$$\begin{aligned} \delta E_{33} \cong & \left[\delta\overline{w}_h'^{(i)} g_{3,h}^{(i)} - \delta\varphi_s'^{(i)} n\right] + \Big\{\overline{w}_h'^{(i)}\delta\overline{w}_k'^{(i)} g_{3,h}^{(i)}\, g_{3,k}^{(i)} + u_0'^{(i)}\delta u_0'^{(i)} + v_0'^{(i)}\delta v_0'^{(i)} + \\ & + \varphi_3'^{(i)}\delta\varphi_3'^{(i)}\left[\left(x - x_o^{(i)}\right)^2 + \left(y - y_o^{(i)}\right)^2\right] - \delta u_0'^{(i)}\varphi_3'^{(i)}\left(y - y_o^{(i)}\right) + \\ & - u_0'^{(i)}\delta\varphi_3'^{(i)}\left(y - y_o^{(i)}\right) + \delta v_0'^{(i)}\varphi_3'^{(i)}\left(x - x_o^{(i)}\right) + v_0'^{(i)}\delta\varphi_3'^{(i)}\left(x - x_o^{(i)}\right)\Big\} \end{aligned} \tag{1.15.c}$$

In Eqs. (1.12a–c) the coupling between the kinematical unknowns $\overline{w}_h^{(i)}$ and $\varphi_s^{(i)}$ has been discarded. Furthermore, in Eq. (1.12.c) the coupling between $\varphi_s^{(i)}$ and its derivative $\varphi_s'^{(i)}$ has been ignored. As a consequence, the same assumption occurs in Eqs. (1.15a–c).

1.6 STRESS-STRAIN RELATIONSHIP

Due to the hypotheses of small deformations and moderate rotations, the second Piola-Kirchhoff stress tensor, which coincides with the classical Cauchy stress tensor, S, is here adopted as a stress measure:

$$\mathbf{S} = \begin{bmatrix} S_{11} & S_{12} & S_{13} \\ S_{11} & S_{22} & S_{23} \\ S_{13} & S_{23} & S_{33} \end{bmatrix} \tag{1.16}$$

It is assumed that the stress components are conjugated with the Green strain components through the classical linear elasticity relationship:

$$\left[S_{13},\ S_{23},\ S_{33}\right]^T = \mathbf{C}\left[2E_{13},\ 2\mathrm{E}_{23},\ \mathrm{E}_L\right]^T = \begin{bmatrix} G_{13} & 0 & 0 \\ 0 & G_{23} & 0 \\ 0 & 0 & E_L \end{bmatrix}\left[2E_{13},\ 2\mathrm{E}_{23},\ \mathrm{E}_{33}\right]^T \tag{1.17}$$

where the symbols E_L, G_{13} and G_{23} denote, respectively, Young's modulus along the beam axis and the shear modulus within the (*x*-*z*) and (*y*-*z*) planes (Figure 1.1) while $\mathbf{C}$ is a diagonal matrix which accounts for the elastic moduli.

1.7 VARATIONAL FORMULATION

In view of the formulation of a finite element approach, it is useful to rewrite the equilibrium problem by means of the principle of virtual displacement.

The virtual work of internal stresses can be expressed as follows:

$$\delta L_{\text{int}} = \sum_{i=1}^{N} \int_0^L dz \int_{\Sigma^{(i)}} \left[2S_{13}\delta E_{13} + 2S_{23}\delta E_{23} + S_{33}\delta E_{33} \right] d\Sigma \tag{1.18}$$

It is worth noting that the internal work δL_{int} accounts for second-order terms.

On the other hand, the virtual work of the external forces assumes the following form:

$$\delta L_{ext} = \sum_{i=1}^{N} \int_{0}^{L} dz \left[\int_{\Sigma^{(i)}} \left(\mathbf{b}\delta\mathbf{u} \right) \mathrm{d}\Sigma + \int_{\partial\Sigma^{(i)}} \left(\mathbf{p}\delta\mathbf{u} \right) \mathrm{ds} \right] + \sum_{i=1}^{N} \int_{\Sigma^{(i,\alpha)}} \left(\mathbf{p}\delta\mathbf{u} \right) \mathrm{d}\Sigma \tag{1.19}$$

where:

- $\mathbf{b} = \left[b_1,\ b_2,\ b_3 \right]^{\mathrm{T}}$ the external force field – per unit volume;
- $\mathbf{p} = \left[p_1,\ p_2,\ p_3 \right]^{\mathrm{T}}$ the external force field acting on the boundary of the beam –per unit surface–;
- $\delta\mathbf{u} = \left[\delta u,\ \delta v,\ \delta w \right]^{T}$ is the first variation of the admissible displacement field given by Eq. (1.1);
- $\alpha = 1,2$ the index which refers to the current end of the beam;
- N the number of panels;
- L the length of the beam axis.

Due to the linear form of the displacement field, the second-order terms do not emerge in Eq. (1.19).

As a result:

$$\begin{aligned} \delta L_{ext} = & \sum_{i=1}^{N} \int_{0}^{L} \left[q_1^{(i)} \delta u_o^{(i)} + q_2^{(i)} \delta v_o^{(i)} + q_{3,h}^{(i)}\ \delta \overline{w}_h^{(i)} + m_3^{(i)} \delta\varphi_3^{(i)} + m_s^{(i)} \delta\varphi_s^{(i)} \right] dz + \\ & + Q_1^{(i,\alpha)} \delta u_o^{(i,\alpha)} + Q_2^{(i,\alpha)} \delta v_o^{(i,\alpha)} + Q_{3,h}^{(i,\alpha)} \delta \overline{w}_h^{(i,\alpha)} + C_3^{(i,\alpha)} \delta\varphi_3^{(i,\alpha)} + C_s^{(i,\alpha)} \delta\varphi_s^{(i,\alpha)} \end{aligned} \tag{1.20}$$

with

$$q_1^{(i)} = \int_{\Sigma^{(i)}} b_1 \mathrm{d}\Sigma + \int_{\partial\Sigma^{(i)}} p_1 \mathrm{d}s \tag{1.21.a}$$

$$q_2^{(i)} = \int_{\Sigma^{(i)}} b_2 \mathrm{d}\Sigma + \int_{\partial\Sigma^{(i)}} p_2 \mathrm{d}s \tag{1.21.b}$$

$$q_{3,h}^{(i)} = \int_{\Sigma^{(i)}} b_3 f_h^{(i)} \mathrm{d}\Sigma + \int_{\partial\Sigma^{(i)}} p_3 f_h^{(i)} \mathrm{d}s \tag{1.21.c}$$

$$m_3^{(i)} = \int_{\Sigma^{(i)}} \left[-b_1 \left(y - y_o^{(i)} \right) + b_2 \left(x - x_o^{(i)} \right) \right] \mathrm{d}\Sigma + \int_{\partial\Sigma^{(i)}} \left[-p_1 \left(y - y_o^{(i)} \right) + p_2 \left(x - x_o^{(i)} \right) \right] \mathrm{d}s \tag{1.21.d}$$

$$m_s^{(i)} = -\int_{\Sigma^{(i)}} b_3 \mathrm{n} \mathrm{d}\Sigma - \int_{\partial\Sigma^{(i)}} p_3 \mathrm{n} \mathrm{d}s \tag{1.21.e}$$

and

$$Q_1^{(i,\alpha)} = \int_{\Sigma^{(i,\alpha)}} p_1 \mathrm{d}\Sigma \tag{1.22.a}$$

$$Q_2^{(i,\alpha)} = \int_{\Sigma^{(i,\alpha)}} p_2 \mathrm{d}\Sigma \tag{1.22.b}$$

$$Q_{3,h}^{(i,\alpha)} = \int_{\Sigma^{(i,\alpha)}} p_3 f_h^{(i)} \mathrm{d}\Sigma \tag{1.22.c}$$

$$C_3^{(i,\alpha)} = \int_{\Sigma^{(i,\alpha)}} \left[-p_1 \left(y - y_o^{(i)} \right) + p_2 \left(x - x_o^{(i)} \right) \right] \mathrm{d}\Sigma \tag{1.22.d}$$

$$C_s^{(i,\alpha)} = -\int_{\Sigma^{(i,\alpha)}} p_3 \mathrm{n} \mathrm{d}\Sigma \tag{1.22.e}$$

Finally, the principle of virtual displacements can be expressed as follows:

$$\delta L_{\mathrm{int}} + \delta L_{\mathrm{con}} = \int_0^L \mathbf{q} \delta \mathbf{v} \, \mathrm{d}z + \mathbf{Q}^{(\alpha)} \delta \mathbf{v}^{(\alpha)} \tag{1.23}$$

where:

$$\mathbf{q} = \left[\ldots, \left(q_1^{(i)}, q_2^{(i)}, \ldots, q_{3,h}^{(i)}, \ldots, m_3^{(i)}, m_s^{(i)} \right), \ldots \right] \tag{1.24.a}$$

$$\delta\mathbf{v} = \left[\ldots,\left(\delta u_o^{(i)},\delta v_o^{(i)},\ldots,\delta\bar{w}_h^{(i)},\ldots,\delta\varphi_3^{(i)},\delta\varphi_s^{(i)}\right),\ldots\right]^{\mathrm{T}} \tag{1.24.b}$$

$$\mathbf{Q}^{(\alpha)} = \left[\ldots,\left(Q_1^{(i,\alpha)},Q_2^{(i,\alpha)},\ldots,Q_{3,h}^{(i,\alpha)},\ldots,C_3^{(i,\alpha)},C_s^{(i,\alpha)}\right),\ldots\right] \tag{1.24.c}$$

$$\delta\mathbf{v}^{(\alpha)} = \left[\ldots,\left(\delta u_o^{(i,\alpha)},\delta v_o^{(i,\alpha)},\ldots,\delta\bar{w}_h^{(i,\alpha)},\ldots,\delta\varphi_3^{(i,\alpha)},\delta\varphi_s^{(i,\alpha)}\right),\ldots\right]^{\mathrm{T}} \tag{1.24.d}$$

$$\begin{aligned}\delta L_{\mathrm{con}} = &\sum_{r=1}^{N_{con}}\int_0^L\left[\sigma_u^{(r)}\delta\left(\mathrm{d}u^{(r)}\right)+\sigma_v^{(r)}\delta\left(\mathrm{d}v^{(r)}\right)+\sigma_w^{(r)}\delta\left(\mathrm{d}w^{(r)}\right)\right]t^{(r)}dz+\\ &+\sum_{r=1}^{N_{con}}\int_0^L\mu_3^{(r)}\delta\left(\mathrm{d}\varphi_3^{(r)}\right)dz\end{aligned} \tag{1.24.e}$$

It is worth noting that the term δL_{con} accounts for the contribution relative to the work done by interaction $\sigma_u^{(r)},\sigma_v^{(r)},\sigma_w^{(r)}$ and $\mu_3^{(r)}$ (the index *r* refers to the *r-th* internal junction, $r=1,2,...,N_{con}$) in the presence of their conjugated admissible displacements: $\mathrm{d}u^{(r)},\mathrm{d}v^{(r)},\mathrm{d}w^{(r)}$ and $\mathrm{d}\varphi_3^{(r)}$.

In Eq. (1.24.e) the symbol $t^{(r)}$ denotes the interfacial width at the *r-th* connection.

The symbols used in Eq. (1.24.e) have already been introduced in Section 1.3.

1.8 FINITE ELEMENT MODEL

A two-node finite element is used, characterized by cubic interpolating Hermitian shape functions.

Let $\mathbf{v}_e$ be a numeric vector collecting the degrees of freedom related to a generic finite *e*-element, with the subscripts "*a*" and "*b*" denoting the first and second nodes, respectively.

$$\mathbf{v}_e = \left[\left(\ldots, u_o^{(i)}, v_o^{(i)}, \ldots, \bar{w}_h^{(i)}, \ldots, \varphi_3^{(i)}, \varphi_s^{(i)}, \ldots \right)_a, \left(\ldots, u_o'^{(i)}, v_o'^{(i)}, \ldots, \bar{w}_h'^{(i)}, \ldots, \varphi_3'^{(i)}, \varphi_s'^{(i)}, \ldots \right)_a, \right.$$
$$\left. \left(\ldots, u_o^{(i)}, v_o^{(i)}, \ldots, \bar{w}_h^{(i)}, \ldots, \varphi_3^{(i)}, \varphi_s^{(i)}, \ldots \right)_b, \left(\ldots, u_o'^{(i)}, v_o'^{(i)}, \ldots, \bar{w}_h'^{(i)}, \ldots, \varphi_3'^{(i)}, \varphi_s'^{(i)}, \ldots \right)_b \right]^T \quad (1.25)$$

The generalized displacements field $\mathbf{v} = \left[\ldots, \left(u_o^{(i)}, v_o^{(i)}, \bar{w}_h^{(i)}, \varphi_s^{(i)}, \varphi_3^{(i)} \right), \ldots \right]^T$ can be interpolated over the generic finite element as follows:

$$\mathbf{v} = \mathbf{N}\mathbf{v}_e \quad (1.26)$$

In Eq. (1.26), the symbol $\mathbf{N}$ denotes the following block matrix:

$$\mathbf{N} = \left[\mathbf{N}_{10}, \quad \mathbf{N}_{11}, \quad \mathbf{N}_{20}, \quad \mathbf{N}_{21} \right] \quad (1.27)$$

where

$$\mathbf{N}_{pq} = \begin{bmatrix} \ddots & & & & & & & \\ & \begin{bmatrix} h_{pq} & 0 & 0 & 0 & 0 & 0 & 0 \\ 0 & h_{pq} & 0 & 0 & 0 & 0 & 0 \\ 0 & 0 & h_{pq} & 0 & 0 & 0 & 0 \\ 0 & 0 & 0 & h_{pq} & 0 & 0 & 0 \\ 0 & 0 & 0 & 0 & h_{pq} & 0 & 0 \\ 0 & 0 & 0 & 0 & 0 & h_{pq} & 0 \\ 0 & 0 & 0 & 0 & 0 & 0 & h_{pq} \end{bmatrix} & & & & & & \\ & & & & & & \ddots \end{bmatrix} \tag{1.28}$$

and h_{pq} are the following cubic Hermitian interpolating functions (p=1,2), (q=0,1):

$$h_{10} = \frac{1}{4}\left(2 - 3\xi + \xi^3\right) \tag{1.29.a}$$

$$h_{11} = \frac{l_e}{8}\left(1 - \xi - \xi^2 + \xi^3\right) \tag{1.29.b}$$

$$h_{20} = \frac{1}{4}\left(2 + 3\xi - \xi^3\right) \tag{1.29.c}$$

$$h_{21} = \frac{l_e}{8}\left(-1 - \xi + \xi^2 + \xi^3\right) \tag{1.29.d}$$

being ξ the normalized axial coordinate ($-1 \le \xi \le 1$) and l_e the length of the current finite element.

The internal stresses can be expressed as a function of the nodal displacements by means of:

$$\left[S_{13},\ \mathrm{S}_{23},\ \mathrm{S}_{33}\right]^{\mathrm{T}} = \mathbf{C}\begin{bmatrix} 2\left(\mathbf{B}_{\mathrm{L},13} + \mathbf{v}_{\mathrm{e}}^{T}\mathbf{B}_{\mathrm{NL},13}\right) \\ 2\left(\mathbf{B}_{\mathrm{L},23} + \mathbf{v}_{\mathrm{e}}^{T}\mathbf{B}_{\mathrm{NL},23}\right) \\ \left(\mathbf{B}_{\mathrm{L},33} + \mathbf{v}_{\mathrm{e}}^{T}\mathbf{B}_{\mathrm{NL},33}\right) \end{bmatrix}\mathbf{v}_{\mathrm{e}} \tag{1.30}$$

where S_{13}, S_{23} and S_{33} denote the internal stresses, $\mathbf{C}$ accounts for the elastic moduli as indicated in Eq. (1.17) while $\mathbf{B}_{\mathrm{L},13}$, $\mathbf{B}_{\mathrm{L},23}$, $\mathbf{B}_{\mathrm{L},33}$ and $\mathbf{B}_{\mathrm{NL},13}$, $\mathbf{B}_{\mathrm{NL},23}$, $\mathbf{B}_{\mathrm{NL},33}$ are numerical vectors/matrices which account for the linear and nonlinear parts of the strain field, respectively.
Following the full expressions of the linear and nonlinear parts of $\mathbf{B}$ are reported. With regard to the linear part it assumes the following form:

$$\mathbf{B}_{L,13} = \frac{1}{2}\left[\bar{\mathbf{B}}_{L,13}^{(1,0)}, \bar{\mathbf{B}}_{L,13}^{(1,1)}, \bar{\mathbf{B}}_{L,13}^{(2,0)}, \bar{\mathbf{B}}_{L,13}^{(2,1)}\right] \tag{1.31.a}$$

$$\mathbf{B}_{L,23} = \frac{1}{2}\left[\bar{\mathbf{B}}_{L,23}^{(1,0)}, \bar{\mathbf{B}}_{L,23}^{(1,1)}, \bar{\mathbf{B}}_{L,23}^{(2,0)}, \bar{\mathbf{B}}_{L,23}^{(2,1)}\right] \tag{1.31.b}$$

$$\mathbf{B}_{L,33} = \left[\bar{\mathbf{B}}_{L,33}^{(1,0)}, \bar{\mathbf{B}}_{L,33}^{(1,1)}, \bar{\mathbf{B}}_{L,33}^{(2,0)}, \bar{\mathbf{B}}_{L,33}^{(2,1)}\right] \tag{1.31.c}$$

The dimensions of $\mathbf{B}_{L,13}$, $\mathbf{B}_{L,23}$ and $\mathbf{B}_{L,33}$ are $\left[1 \times \left(7 \times 4 \times N\right)\right]$, where 7 indicates the degrees of freedom of each *i*-panel, 4 accounts for global number of the Hermitian interpolating functions $\mathrm{h}^{(\mathrm{p,q})}$ (p=1,2 and q=0,1), while N is the number of panels.

The generic block, $\bar{\mathbf{B}}_{L,13}^{(\mathrm{p,q})}$, $\bar{\mathbf{B}}_{L,23}^{(\mathrm{p,q})}$ and $\bar{\mathbf{B}}_{L,33}^{(\mathrm{p,q})}$ assumes the following expression depending on the number of panels ($1 \le i \le N$):

$$\bar{\mathbf{B}}_{L,13}^{(\mathrm{p,q})} = \left[\left(\bar{\mathbf{B}}_{L,13}^{(\mathrm{p,q})}\right)^{(i=1)} \quad \cdots \quad \left(\bar{\mathbf{B}}_{L,13}^{(\mathrm{p,q})}\right)^{(i)} \quad \cdots \quad \left(\bar{\mathbf{B}}_{L,13}^{(\mathrm{p,q})}\right)^{(i=N)} \right] \tag{1.32.a}$$

$$\bar{\mathbf{B}}_{L,23}^{(\mathrm{p,q})} = \left[\left(\bar{\mathbf{B}}_{L,23}^{(\mathrm{p,q})}\right)^{(i=1)} \quad \cdots \quad \left(\bar{\mathbf{B}}_{L,23}^{(\mathrm{p,q})}\right)^{(i)} \quad \cdots \quad \left(\bar{\mathbf{B}}_{L,23}^{(\mathrm{p,q})}\right)^{(i=N)} \right] \tag{1.32.b}$$

$$\bar{\mathbf{B}}_{L,33}^{(\mathrm{p,q})} = \left[\left(\bar{\mathbf{B}}_{L,33}^{(\mathrm{p,q})}\right)^{(i=1)} \quad \cdots \quad \left(\bar{\mathbf{B}}_{L,33}^{(\mathrm{p,q})}\right)^{(i)} \quad \cdots \quad \left(\bar{\mathbf{B}}_{L,33}^{(\mathrm{p,q})}\right)^{(i=N)} \right] \tag{1.32.c}$$

The dimension of $\bar{\mathbf{B}}_{L,13}^{(\mathrm{p,q})}$, $\bar{\mathbf{B}}_{L,23}^{(\mathrm{p,q})}$ and $\bar{\mathbf{B}}_{L,33}^{(\mathrm{p,q})}$ is $\left[1 \times \left(7 \times N\right)\right]$. The generic sub-blocks, $\left(\bar{\mathbf{B}}_{L,13}^{(\mathrm{p,q})}\right)^{(i)}$, $\left(\bar{\mathbf{B}}_{L,23}^{(\mathrm{p,q})}\right)^{(i)}$ and $\left(\bar{\mathbf{B}}_{L,33}^{(\mathrm{p,q})}\right)^{(i)}$ assume the following form:

$$\left(\bar{\mathbf{B}}_{L,13}^{(\mathrm{p,q})}\right)^{(i)} = \left[h'_{\mathrm{p,q}} \quad 0 \quad g_{1,1}^{(i)} h_{\mathrm{p,q}} \quad g_{1,2}^{(i)} h_{\mathrm{p,q}} \quad g_{1,3}^{(i)} h_{\mathrm{p,q}} \quad -\left(y - y_0^{(i)}\right) h'_{\mathrm{p,q}} \quad -\frac{dn}{dx} h_{\mathrm{p,q}} \right] \tag{1.33.a}$$

$$\left(\bar{\mathbf{B}}_{L,23}^{(\mathrm{p,q})}\right)^{(i)} = \left[0 \quad h'_{\mathrm{p,q}} \quad g_{2,1}^{(i)} h_{\mathrm{p,q}} \quad g_{2,2}^{(i)} h_{\mathrm{p,q}} \quad g_{2,3}^{(i)} h_{\mathrm{p,q}} \quad \left(x - x_0^{(i)}\right) h'_{\mathrm{p,q}} \quad -\frac{dn}{dy} h_{\mathrm{p,q}} \right] \tag{1.33.b}$$

$$\left(\bar{\mathbf{B}}_{L,33}^{(\mathrm{p,q})}\right)^{(i)} = \left[0 \quad 0 \quad g_{3,1}^{(i)} h'_{\mathrm{p,q}} \quad g_{3,2}^{(i)} h'_{\mathrm{p,q}} \quad g_{3,3}^{(i)} h'_{\mathrm{p,q}} \quad 0 \quad -n\, h'_{\mathrm{p,q}} \right] \tag{1.33.c}$$

The non-linear part of $\mathbf{B}$ assumes the following forms:

$$\mathbf{B}_{NL,13}=\begin{bmatrix} \bar{\mathbf{B}}_{NL,13}^{(1,0,1,0)} & \bar{\mathbf{B}}_{NL,13}^{(1,0,1,1)} & \bar{\mathbf{B}}_{NL,13}^{(1,0,2,0)} & \bar{\mathbf{B}}_{NL,13}^{(1,0,2,1)} \\ \bar{\mathbf{B}}_{NL,13}^{(1,1,1,0)} & \bar{\mathbf{B}}_{NL,13}^{(1,1,1,1)} & \bar{\mathbf{B}}_{NL,13}^{(1,1,2,0)} & \bar{\mathbf{B}}_{NL,13}^{(1,1,2,1)} \\ \bar{\mathbf{B}}_{NL,13}^{(2,0,1,0)} & \bar{\mathbf{B}}_{NL,13}^{(2,0,1,1)} & \bar{\mathbf{B}}_{NL,13}^{(2,0,2,0)} & \bar{\mathbf{B}}_{NL,13}^{(2,0,2,1)} \\ \bar{\mathbf{B}}_{NL,13}^{(2,1,1,0)} & \bar{\mathbf{B}}_{NL,13}^{(2,1,1,1)} & \bar{\mathbf{B}}_{NL,13}^{(2,1,2,0)} & \bar{\mathbf{B}}_{NL,13}^{(2,1,2,1)} \end{bmatrix} \tag{1.34.a}$$

$$\mathbf{B}_{NL,23}=\begin{bmatrix} \bar{\mathbf{B}}_{NL,23}^{(1,0,1,0)} & \bar{\mathbf{B}}_{NL,23}^{(1,0,1,1)} & \bar{\mathbf{B}}_{NL,23}^{(1,0,2,0)} & \bar{\mathbf{B}}_{NL,23}^{(1,0,2,1)} \\ \bar{\mathbf{B}}_{NL,23}^{(1,1,1,0)} & \bar{\mathbf{B}}_{NL,23}^{(1,1,1,1)} & \bar{\mathbf{B}}_{NL,23}^{(1,1,2,0)} & \bar{\mathbf{B}}_{NL,23}^{(1,1,2,1)} \\ \bar{\mathbf{B}}_{NL,23}^{(2,0,1,0)} & \bar{\mathbf{B}}_{NL,23}^{(2,0,1,1)} & \bar{\mathbf{B}}_{NL,23}^{(2,0,2,0)} & \bar{\mathbf{B}}_{NL,23}^{(2,0,2,1)} \\ \bar{\mathbf{B}}_{NL,23}^{(2,1,1,0)} & \bar{\mathbf{B}}_{NL,23}^{(2,1,1,1)} & \bar{\mathbf{B}}_{NL,23}^{(2,1,2,0)} & \bar{\mathbf{B}}_{NL,23}^{(2,1,2,1)} \end{bmatrix} \tag{1.34.b}$$

$$\mathbf{B}_{NL,33}=\begin{bmatrix} \bar{\mathbf{B}}_{NL,33}^{(1,0,1,0)} & \bar{\mathbf{B}}_{NL,33}^{(1,0,1,1)} & \bar{\mathbf{B}}_{NL,33}^{(1,0,2,0)} & \bar{\mathbf{B}}_{NL,33}^{(1,0,2,1)} \\ \bar{\mathbf{B}}_{NL,33}^{(1,1,1,0)} & \bar{\mathbf{B}}_{NL,33}^{(1,1,1,1)} & \bar{\mathbf{B}}_{NL,33}^{(1,1,2,0)} & \bar{\mathbf{B}}_{NL,33}^{(1,1,2,1)} \\ \bar{\mathbf{B}}_{NL,33}^{(2,0,1,0)} & \bar{\mathbf{B}}_{NL,33}^{(2,0,1,1)} & \bar{\mathbf{B}}_{NL,33}^{(2,0,2,0)} & \bar{\mathbf{B}}_{NL,33}^{(2,0,2,1)} \\ \bar{\mathbf{B}}_{NL,33}^{(2,1,1,0)} & \bar{\mathbf{B}}_{NL,33}^{(2,1,1,1)} & \bar{\mathbf{B}}_{NL,33}^{(2,1,2,0)} & \bar{\mathbf{B}}_{NL,33}^{(2,1,2,1)} \end{bmatrix} \tag{1.34.c}$$

The dimension of $\mathbf{B}_{NL,13}, \mathbf{B}_{NL,23}$ and $\mathbf{B}_{NL,33}$ is $\left[\left(7 \times 4 \times N\right) \times \left(7 \times 4 \times N\right)\right]$.

The generic block matrix, $\overline{\mathbf{B}}_{NL,13}^{(\mathrm{p,q,r,s})}$, $\overline{\mathbf{B}}_{NL,23}^{(\mathrm{p,q,r,s})}$ and $\overline{\mathbf{B}}_{NL,33}^{(\mathrm{p,q,r,s})}$ assumes the following expression depending on the number of panels ($1 \le i \le N$):

$$\overline{\mathbf{B}}_{NL,13}^{(\mathrm{p,q,r,s})} = \begin{bmatrix} \left(\overline{\mathbf{B}}_{NL,13}^{(\mathrm{p,q,r,s})}\right)^{(i=1)} & \cdots & \mathbf{0} & \cdots & \mathbf{0} \\ \vdots & \ddots & & & \vdots \\ \mathbf{0} & & \left(\overline{\mathbf{B}}_{NL,13}^{(\mathrm{p,q,r,s})}\right)^{(i)} & & \mathbf{0} \\ \vdots & & & \ddots & \vdots \\ \mathbf{0} & \cdots & \mathbf{0} & \cdots & \left(\overline{\mathbf{B}}_{NL,13}^{(\mathrm{p,q,r,s})}\right)^{(i=N)} \end{bmatrix} \tag{1.35.a}$$

$$\overline{\mathbf{B}}_{NL,23}^{(\mathrm{p,q,r,s})} = \begin{bmatrix} \left(\overline{\mathbf{B}}_{NL,23}^{(\mathrm{p,q,r,s})}\right)^{(i=1)} & \cdots & \mathbf{0} & \cdots & \mathbf{0} \\ \vdots & \ddots & & & \vdots \\ \mathbf{0} & & \left(\overline{\mathbf{B}}_{NL,23}^{(\mathrm{p,q,r,s})}\right)^{(i)} & & \mathbf{0} \\ \vdots & & & \ddots & \vdots \\ \mathbf{0} & \cdots & \mathbf{0} & \cdots & \left(\overline{\mathbf{B}}_{NL,23}^{(\mathrm{p,q,r,s})}\right)^{(i=N)} \end{bmatrix} \tag{1.35.b}$$

$$\overline{\mathbf{B}}_{NL,33}^{(\mathrm{p,q,r,s})} = \begin{bmatrix} \left(\overline{\mathbf{B}}_{NL,33}^{(\mathrm{p,q,r,s})}\right)^{(i=1)} & \cdots & \mathbf{0} & \cdots & \mathbf{0} \\ \vdots & \ddots & & & \vdots \\ \mathbf{0} & & \left(\overline{\mathbf{B}}_{NL,33}^{(\mathrm{p,q,r,s})}\right)^{(i)} & & \mathbf{0} \\ \vdots & & & \ddots & \vdots \\ \mathbf{0} & \cdots & \mathbf{0} & \cdots & \left(\overline{\mathbf{B}}_{NL,33}^{(\mathrm{p,q,r,s})}\right)^{(i=N)} \end{bmatrix}, \tag{1.35.c}$$

The dimension of $\bar{\mathbf{B}}_{NL,13}^{(\mathrm{p,q,r,s})}$, $\bar{\mathbf{B}}_{NL,23}^{(\mathrm{p,q,r,s})}$ and $\bar{\mathbf{B}}_{NL,33}^{(\mathrm{p,q,r,s})}$ is $\left[\left(7 \times N\right) \times \left(7 \times N\right)\right]$. The generic block, $\left(\bar{\mathbf{B}}_{NL,23}^{(\mathrm{p,q,r,s})}\right)^{(i)}$ and $\left(\bar{\mathbf{B}}_{NL,33}^{(\mathrm{p,q,r,s})}\right)^{(i)}$ assumes the following form:

$$\left(\bar{\mathbf{B}}_{NL,13}^{(\mathrm{p,q,r,s})}\right)^{(i)} = \frac{1}{2}\begin{bmatrix} 0 & 0 & 0 & 0 & 0 & 0 & 0 \\ 0 & 0 & 0 & 0 & 0 & 0 & 0 \\ 0 & 0 & h_{\mathrm{p,q}}h'_{\mathrm{r,s}}g_{1,1}^{(i)}\,g_{3,1}^{(i)} & h_{\mathrm{p,q}}h'_{\mathrm{r,s}}g_{1,1}^{(i)}\,g_{3,2}^{(i)} & h_{\mathrm{p,q}}h'_{\mathrm{r,s}}g_{1,1}^{(i)}\,g_{3,3}^{(i)} & 0 & 0 \\ 0 & 0 & h_{\mathrm{p,q}}h'_{\mathrm{r,s}}g_{1,2}^{(i)}\,g_{3,1}^{(i)} & h_{\mathrm{p,q}}h'_{\mathrm{r,s}}g_{1,2}^{(i)}\,g_{3,2}^{(i)} & h_{\mathrm{p,q}}h'_{\mathrm{r,s}}g_{1,2}^{(i)}\,g_{3,3}^{(i)} & 0 & 0 \\ 0 & 0 & h_{\mathrm{p,q}}h'_{\mathrm{r,s}}g_{1,3}^{(i)}\,g_{3,1}^{(i)} & h_{\mathrm{p,q}}h'_{\mathrm{r,s}}g_{1,3}^{(i)}\,g_{3,2}^{(i)} & h_{\mathrm{p,q}}h'_{\mathrm{r,s}}g_{1,3}^{(i)}\,g_{3,3}^{(i)} & 0 & 0 \\ 0 & h'_{\mathrm{p,q}}h_{\mathrm{r,s}} & 0 & 0 & 0 & h'_{\mathrm{p,q}}h_{\mathrm{r,s}}\left(x - x_0^{(i)}\right) & 0 \\ 0 & 0 & 0 & 0 & 0 & 0 & 0 \end{bmatrix} \tag{1.36.a}$$

$$\left(\bar{\mathbf{B}}_{NL,23}^{(\mathrm{p,q,r,s})}\right)^{(i)} = \frac{1}{2}\begin{bmatrix} 0 & 0 & 0 & 0 & 0 & 0 & 0 \\ 0 & 0 & 0 & 0 & 0 & 0 & 0 \\ 0 & 0 & h_{\mathrm{p,q}}h'_{\mathrm{r,s}}g_{2,1}^{(i)}\,g_{3,1}^{(i)} & h_{\mathrm{p,q}}h'_{\mathrm{r,s}}g_{2,1}^{(i)}\,g_{3,2}^{(i)} & h_{\mathrm{p,q}}h'_{\mathrm{r,s}}g_{2,1}^{(i)}\,g_{3,3}^{(i)} & 0 & 0 \\ 0 & 0 & h_{\mathrm{p,q}}h'_{\mathrm{r,s}}g_{2,2}^{(i)}\,g_{3,1}^{(i)} & h_{\mathrm{p,q}}h'_{\mathrm{r,s}}g_{2,2}^{(i)}\,g_{3,2}^{(i)} & h_{\mathrm{p,q}}h'_{\mathrm{r,s}}g_{2,2}^{(i)}\,g_{3,3}^{(i)} & 0 & 0 \\ 0 & 0 & h_{\mathrm{p,q}}h'_{\mathrm{r,s}}g_{2,3}^{(i)}\,g_{3,1}^{(i)} & h_{\mathrm{p,q}}h'_{\mathrm{r,s}}g_{2,3}^{(i)}\,g_{3,2}^{(i)} & h_{\mathrm{p,q}}h'_{\mathrm{r,s}}g_{2,3}^{(i)}\,g_{3,3}^{(i)} & 0 & 0 \\ -h'_{\mathrm{p,q}}h_{\mathrm{r,s}} & 0 & 0 & 0 & 0 & h'_{\mathrm{p,q}}h_{\mathrm{r,s}}\left(y - y_0^{(i)}\right) & 0 \\ 0 & 0 & 0 & 0 & 0 & 0 & 0 \end{bmatrix} \tag{1.36.b}$$

$$\left(\bar{\mathbf{B}}_{NL,33}^{(\mathrm{p,q,r,s})}\right)^{(i)} =$$

$$\frac{1}{2}\begin{bmatrix} h'_{\mathrm{p,q}}h'_{\mathrm{r,s}} & 0 & 0 & 0 & 0 & -2h'_{\mathrm{p,q}}h'_{\mathrm{r,s}}\left(y-y_0^{(i)}\right) & 0 \\ 0 & h'_{\mathrm{p,q}}h'_{\mathrm{r,s}} & 0 & 0 & 0 & 2h'_{\mathrm{p,q}}h'_{\mathrm{r,s}}\left(x-x_0^{(i)}\right) & 0 \\ 0 & 0 & h'_{\mathrm{p,q}}h'_{\mathrm{r,s}}\left(g_{3,1}^{(i)}\right)^2 & 2h'_{\mathrm{p,q}}h'_{\mathrm{r,s}}\,g_{3,1}^{(i)}\,g_{3,2}^{(i)} & 2h'_{\mathrm{p,q}}h'_{\mathrm{r,s}}\,g_{3,1}^{(i)}\,g_{3,3}^{(i)} & 0 & 0 \\ 0 & 0 & 0 & h'_{\mathrm{p,q}}h'_{\mathrm{r,s}}\left(g_{3,2}^{(i)}\right)^2 & 2h'_{\mathrm{p,q}}h'_{\mathrm{r,s}}\,g_{3,2}^{(i)}\,g_{3,3}^{(i)} & 0 & 0 \\ 0 & 0 & 0 & 0 & h'_{\mathrm{p,q}}h'_{\mathrm{r,s}}\left(g_{3,3}^{(i)}\right)^2 & 0 & 0 \\ 0 & 0 & 0 & 0 & 0 & h'_{\mathrm{p,q}}h'_{\mathrm{r,s}}\left(y-y_0^{(i)}\right)^2 + h'_{\mathrm{p,q}}h'_{\mathrm{r,s}}\left(x-x_0^{(i)}\right)^2 & 0 \\ 0 & 0 & 0 & 0 & 0 & 0 & 0 \end{bmatrix} \tag{1.36.c}$$

The interactions per unit length arising at the generic *r-th* connection can be collected in the following numeric vector:

$$\mathbf{s}^{(r)} = \left[\left(t^{(r)}\sigma_u^{(r)}\right),\left(t^{(r)}\sigma_v^{(r)}\right),\left(t^{(r)}\sigma_w^{(r)}\right),\mu_3^{(r)}\right]^T \tag{1.37}$$

The vector $\mathbf{s}^{(r)}$ can be related to the displacement discontinuities by means of the following relationship:

$$\mathbf{s}^{(r)} = \mathbf{K}^{(r)}\mathbf{d}^{(r)} \tag{1.38}$$

where

$$\mathbf{d}^{(r)} = \left[\mathrm{d}u^{(r)},\mathrm{d}v^{(r)},\mathrm{d}w^{(r)},\mathrm{d}\varphi_3^{(r)}\right]^T \tag{1.39.a}$$

$$\mathbf{K}^{(r)} = \begin{bmatrix} k_u^{(r)} & 0 & 0 & 0 \\ 0 & k_v^{(r)} & 0 & 0 \\ 0 & 0 & k_w^{(r)} & 0 \\ 0 & 0 & 0 & k_{\varphi_3}^{(r)} \end{bmatrix} \tag{1.39.b}$$

In Eqs. (1.38) and (1.39) the index r denotes the generic connection, while the symbols $k_u^{(r)}$, $k_v^{(r)}$, $k_w^{(r)}$ and $k_{\varphi_3}^{(r)}$ denote the secant stiffness parameters of the considered connection.

It is useful to express the vector $\mathbf{d}^{(r)}$ as follows:

$$\mathbf{d}^{(r)} = \mathbf{D}^{(r)}\mathbf{v} \tag{1.40}$$

where

$$\mathbf{D}^{(r)} = \begin{bmatrix} \dots & -1 & 0 & 0 & 0 & 0 & \left(y_{con}^{(r)} - y_o^{(i)}\right) & 0 & \dots & 1 & 0 & 0 & 0 & 0 & -\left(y_{con}^{(r)} - y_o^{(j)}\right) & 0 & \dots \\ \dots & 0 & -1 & 0 & 0 & 0 & -\left(x_{con}^{(r)} - x_o^{(i)}\right) & 0 & \dots & 0 & 1 & 0 & 0 & 0 & \left(x_{con}^{(r)} - x_o^{(j)}\right) & 0 & \dots \\ \dots & 0 & 0 & -\delta_{1h} & -\delta_{2h} & -\delta_{3h} & 0 & 0 & \dots & 0 & 0 & \delta_{1k} & \delta_{2k} & \delta_{3k} & 0 & 0 & \dots \\ \dots & 0 & 0 & 0 & 0 & 0 & -1 & 0 & \dots & 0 & 0 & 0 & 0 & 0 & 1 & 0 & \dots \end{bmatrix} \tag{1.41.a}$$

$$\mathbf{v} = \left[\dots, \left(u_o^{(i)}, v_o^{(i)}, \dots, \bar{w}_h^{(i)}, \dots, \varphi_3^{(i)}, \varphi_s^{(i)}\right), \dots, \left(u_o^{(j)}, v_o^{(j)}, \dots, \bar{w}_k^{(j)}, \dots, \varphi_3^{(j)}, \varphi_s^{(j)}\right), \dots\right]^{\mathrm{T}} \tag{1.41.b}$$

In Eq. (1.41.a) symbols *h* and *k*, as highlighted in Section 1.4, are indexes related to two specific points, $P_h^{(i)}$ and $P_k^{(j)}$, lying at the same position (i.e the position of the considered connection) on the mid-lines of the two

panels interconnected to each other ($1 \le h \le M^{(i)}, 1 \le k \le M^{(j)}$), while $x_{con}^{(r)}$ and $y_{con}^{(r)}$ are the coordinates of the connection position within the global reference system shown in Figure 1.1. Moreover, $\delta_{(\cdot,\cdot)}$ indicates the Kronecker symbol.

The secant stiffness matrix $\mathbf{K}_e$ assumes the following final form:

$$\mathbf{K}_e = \frac{l_e}{2}\int_{-1}^{+1} \mathbf{B}^T \mathbf{C} \mathbf{B}^* d\xi + \sum_{r=1}^{N_{con}} \frac{l_e}{2}\int_{-1}^{+1} \mathbf{N}^T \left(\mathbf{D}^{(r)}\right)^T \mathbf{K}^{(r)} \mathbf{D}^{(r)} \mathbf{N} d\xi \,. \tag{1.42}$$

In Eq. (1.42), the following positions have been introduced:

$$\mathbf{B} = \begin{bmatrix} 2\left(\mathbf{B}_{L,13} + \mathbf{v}_e^T \mathbf{B}_{NL,13}\right) \\ 2\left(\mathbf{B}_{L,23} + \mathbf{v}_e^T \mathbf{B}_{NL,23}\right) \\ \left(\mathbf{B}_{L,33} + \mathbf{v}_e^T \mathbf{B}_{NL,33}\right) \end{bmatrix}, \tag{1.43.a}$$

$$\mathbf{B}^* = \begin{bmatrix} 2\left[\mathbf{B}_{L,13} + \mathbf{v}_e^T \left(\mathbf{B}_{NL,13} + \mathbf{B}_{NL,13}^T\right)\right] \\ 2\left[\mathbf{B}_{L,23} + \mathbf{v}_e^T \left(\mathbf{B}_{NL,23} + \mathbf{B}_{NL,23}^T\right)\right] \\ \left[\mathbf{B}_{L,33} + \mathbf{v}_e^T \left(\mathbf{B}_{NL,33} + \mathbf{B}_{NL,33}^T\right)\right] \end{bmatrix} \tag{1.43.b}$$

Previously the full expressions of the matrix $\mathbf{B}$ and $\mathbf{B}^*$ are reported.

By standard procedures, the equilibrium equations of the finite element model can be written as follows:

$$\mathbf{K}_{\mathrm{g}}\mathbf{U}_{\mathrm{g}} = \mathbf{F} \tag{1.44}$$

where $\mathbf{K}_{\mathrm{g}}$ is the global secant stiffness matrix, and $\mathbf{U}_{\mathrm{g}}$ and $\mathbf{F}$ denote the nodal global displacements and external force vectors in the global reference system $\{x, y, z\}$, respectively.

1.4 MODEL ASSESSMENT

In order to assess the reliability of the proposed model, many comparative analyses have been undertaken. They concern four different I-beam problems studied in the literature [40–42].
The geometry and the mechanical properties under investigation are summarized in Table 1.1; the meaning of the geometric symbols is clarified in Figure 1.5.

Table 1.1. Mechanical and geometrical properties.

Reference	**Cross Section Shape**	**Static Scheme**	***E* (Longitudinal Young's Modulus)**	***G* Shear Modulus (x-z, y-z planes)**	***B***	***H***	***bf***	***bw***	***L***
			[MPa]	[MPa]	[mm]	[mm]	[mm]	[mm]	[m]
Vlasov	I	CB	20000	10000	100	195	5.0	5.0	2.0
Lee and Lee.	I	SS	17225	861	204	257	16.0	9.0	10.0
Brooks and Turvey	I	CB	17240	2930	51	102	6.4	6.4	1.5
Cortinez and Piovan	I	SS, CB, CS	144000	4140	100	95	10.0	10.0	2.0

SS = simply supported beam

CB= cantilever beam

CS= clamped-simply supported beam

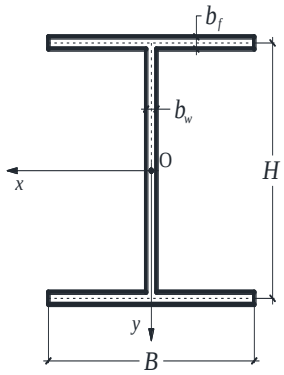

Figure 1.5. Dimensions of the cross section.

A preliminary comparison is relative to the cantilever beam (CB) problem. A torsional load is applied at the free end. In Table 2 the numerical predictions of the present model are compared with the classical Vlasov's solution. In more detail, the comparison deals with the linear response of the beam, in terms of torsional rotations, φ_3, attained at the free end.

The second comparison concerns the lateral buckling load of the laminated composite beam studied by Lee and Kim [40]. In particular, Lee and Kim studied different stacking sequence configurations, accounting for many boundary conditions and positions of the applied external load. They approached the problem by means of a displacement-based one-dimensional finite element model.

The comparison here presented is limited to a simply supported beam (SS) subjected to a uniform unit load, **q**, acting along the centroid vertical line (y axis in Figure 1.5).

A further comparison is relative to the lateral buckling load of the pultruded GFRP CB experimentally investigated by Brooks and Turvey [41]. Although that work dates back many years, their experimental results still represent a valid reference for the purpose of assessing the numerical finite element (FE) model here proposed. The comparison here discussed

concerns a CB subjected to a vertical force, **Q,** at the free end. It also emerges that the experimental pre-buckling displacements [41] substantially agree with the numerical prediction of the present model, as shown in Table 1.3, where the results of a previous work [43] are also reported.

A final comparison focuses on the stability analysis of the composite thin-walled beams with open or closed cross sections studied by Cortinez and Piovan [42]. These results account for the shear deformability, bending and non-uniform warping featured in a consistent way by means of a linearized formulation based on Reissner's variational principle.

The proposed comparison takes into account many structural schemes: SS, CB and a clamped-simply supported beam (CS) axially loaded.

Table 1.2. Comparisons.

Reference paper	**Cross Section Shape**	***q***	***Q***	**φ3**	***P***
		[N/mm]	[kN]	[-]	[kN] x 10^2
Vlasov	I	-	-	0.03195	-
Lee and Lee.	I	3.63	-	-	-
Brooks and Turvey	I	-	1.29	-	-
Cortinez and Piovan	I	-	-	-	1.46 (CB) 5.54 (SS) 10.47 (CS)
Present model	I	3.65	1.35	0.03209	1.43 (CB) 5.20 (SS) 10.40 (CS)

q = uniform unit load along the y axis (acting along the centroid vertical direction)

Q = vertical force applied at the free end of the CB

P = axial force applied at the end.

Table 1.3. Comparisons between the displacement values of Brooks and Turvey and the present model (PM) predictions.

	Load	**Displacement**	
		$v_o^{(2)}$	$\varphi_3^{(2)}$
	[N]	[mm]	[°]
Brooks and Turvey	200	6.80	0.00
Ascione F. [43]		6.98	0.37
PM		6.83	0.38
Brooks and Turvey	390	14.00	0.3
Ascione F. [43]		13.62	0.74
PM		13.31	0.74
Brooks and Turvey	590	21.40	0.50
Ascione F. [43]		20.61	1.12
PM		20.13	1.13
Brooks and Turvey	780	29.10	0.81
Ascione F. [43]		27.26	1.48
PM		26.62	1.49
Brooks and Turvey	970	35.90	1.00
Ascione F. [43]		33.90	1.83
PM		33.10	1.85
Brooks and Turvey	1150	43.20	1.30
Ascione F. [43]		40.20	2.17
PM		39.23	2.20
Brooks and Turvey	1200	-	-
Ascione F. [43]		43.60	2.95
PM		40.93	2.29
Brooks and Turvey	1300	-	-
Ascione F. [43]		-	-
PM		44.34	2.39
Brooks and Turvey	1350	-	-
Ascione F. [43]		-	-
PM		46.04	2.48

The values presented in Table 1.2 in the last row concern the predictions obtained via the PM according to following assumptions:

a) for the purpose of the above listed comparisons the stiffness of the web/flange junctions was increased toward infinity ($K_1 \rightarrow \infty$; $K_2 \rightarrow \infty$), thus enforcing the condition of a rigid transformation of the entire cross section;
b) the buckling loads have been identified as the asymptotic limit of the nonlinear numerical response. An exception, as indicated above, is the first comparison for which a linear analysis has been computed;
c) the mesh details are as in Table 1.4.

Table 1.4 . Mesh details.

Comparison with	***Finite elements*** [-]
Vlasov	1000
Lee and Lee	5000
Brooks and Turvey	750
Cortinez and Piovan	200

1.5 CONCLUSIONS

In order to study the lateral global buckling problem of a new innovative GFRP beam a geometrically nonlinear mechanical model has been presented. The model is capable of predicting the nonlinear pre-buckling behaviour of generic composite beam-columns with open or closed cross-section of arbitrary shape. The model is able to take into account the shear deformability, the warping effects and the possible displacement discontinuities at the web/flange interface.

CHAPTER II

INFLUENCE OF WEB/FLANGE CONNECTION IN THE LATERAL-TORSIONAL BUCKLING PROBLEM

2. INTRODUCTION

The mechanical model presented in Chapter 1 permits to take into account not only the global buckling phenomena but also to investigate the mechanical behavior of web-flange junctions of complex cross section.
In fact, experimental studies by Mosallam et al. [38] and Feo et al. [39] showed that for composite pultruded beams the hypothesis of rigid web/flange connections should be replaced by a more appropriate assumption, primarily due to the anisotropy of the constitutive behavior of the material, but also relating to higher local resin concentration, localized at the web/flange connections, which are suspected to be further responsible for the loss of stiffness, thus requiring more accurate modeling of the web/flange interaction.
Can this loss of stiffness affect the pre-buckling response and, consequently, the buckling loads of composite beams? The influence of the stiffness of the web/flange junction has been recently investigated in [40] by accounting for possible relative rotations, with reference to I-profiles under axial, bending, shear and torsional loads.

In this Chapter numerical results, obtained by means of a finite element approximation, deal with open cross-section composite profiles under flexural/torsional loads, making it possible to identify the relevance of connection stiffness over the pre-buckling range of the mechanical response.

2.1 NUMERICAL SIMULATIONS

The mechanical model discussed in Chapter 1 has been applied to the study of the pre-buckling behavior of a cantilever GFRP I-beam. The load condition deals with an eccentric load applied at the free end of the axis (Figures 2.1 a–b).
Due to the internal features of the model, it is possible to account for the influence of the web/flange stiffness parameters as well as for the position of the load.
In more detail, the influence of the junction stiffness has been simulated according to Section 1.3 of the Chapter 1, in order to investigate the following two cases:

Case (a) rigid connection;

Case (b) semi-rigid connection.

With regard to Case (a), the whole set of stiffness parameters (i.e. eight parameters) were enforced to assume very high values (Table 2.1), thus guaranteeing no discontinuity of the displacement field at the connection point.
Referring to Case (b), the stiffness parameters concerning both the translational spring along the web's mid-line and the rotational spring were given a finite value according to much experimental evidence [38–

39], thus allowing the corresponding discontinuities to emerge. The residual springs are still given very high values.

On the other hand, the influence of the load position has been investigated by considering two choices, as shown in Figure 2.1: The first is relative to an eccentric vertical load applied at the upper flange (Load Position 1 – Figure 2.1a) while the second is relative to a similar eccentric load applied at the lower flange (Load Position 2 – Figure 2.1b).

The geometrical properties of the beam are summarized in Table 2.2 where symbols introduced assume the meaning already clarified in Figure 2.1.

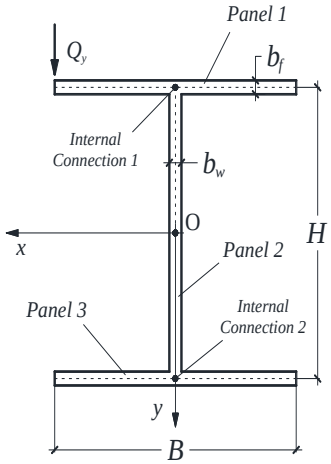

Figure 2.1a. Load position 1: upper flange.

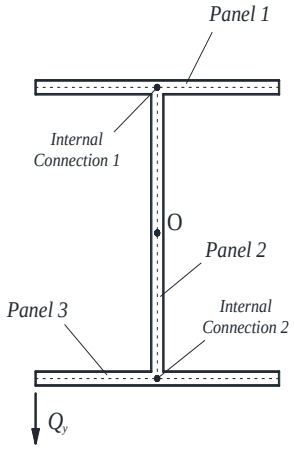

Figure 2.1b. Load position 2: lower flange.

Table 2.1. Mechanical parameters of the web/flange connection relationship.

Web/flange connection	**spring along the web's mid-line**				**rotational spring**			
	Δv_{elas} **[mm]**	Δv_{ult} **[mm]**	K_1 **[N/mm²]**	K_2 **[N/mm²]**	$\Delta\varphi_{3,elas}$ **[rad]**	$\Delta\varphi_{3,ult}$ **[rad]**	K_1 **[Nmm/mm]**	K_2 **[Nmm/mm]**
Case (a)	-	-	→∞	→∞	-	-	→∞	→∞
Case (b)	0.63	0.63	775	775	0.04	0.40	10'000	10'000

Table 2.2. Mechanical and geometrical properties.

Cross section shape	*E* [MPa]	*G* [MPa]	*B* [mm]	*H* [mm]	b_f [mm]	b_w [mm]	*L* [mm]
I	25000	3000	100	190	10	10	4000

After many convergence tests, a mesh composed of 500 finite elements was introduced as a default choice. The convergence was tested for the CB with L=4000 mm subjected to a vertical load applied at the upper flange with the assumption of a semi-rigid connection (Load Position 1 – Case b). The convergence test is reported in Table 2.3.

Table 2.3. Convergence tests for a CB L=4000 mm.

Mesh Refinement	**Convergence Test**	
	Finite elements	$u_o^{(2)}$
#1	50	0.19294
#2	100	0.19189
#3	200	0.19123
#4	300	0.19102
#5	400	0.19094
#6	500	0.19090

The results, in terms of pre-buckling behavior, are reported in Figures 2.2 and 2.3 where the load versus lateral displacement graphs are depicted. In particular, Figure 2.2 is relative to Load Position 1 while Figure 2.3 refers to Load Position 2.

As is easy to understand from Figures 2.2 and 2.3, the following relevant results emerge:

1) The pre-buckling behavior is sensitively affected by the load position. This influence depends on the assumption concerning the stiffness of the internal connections. The stiffer the internal connections, the lower such an effect;
2) No influence seems to be related to the stiffness parameters concerning the vertical spring along the web's mid-line (i.e. y axis);
3) The stiffness of the internal connections (passing from the rigid to the semi-rigid condition) affects the buckling load for a difference more or less equal to 1.5%.

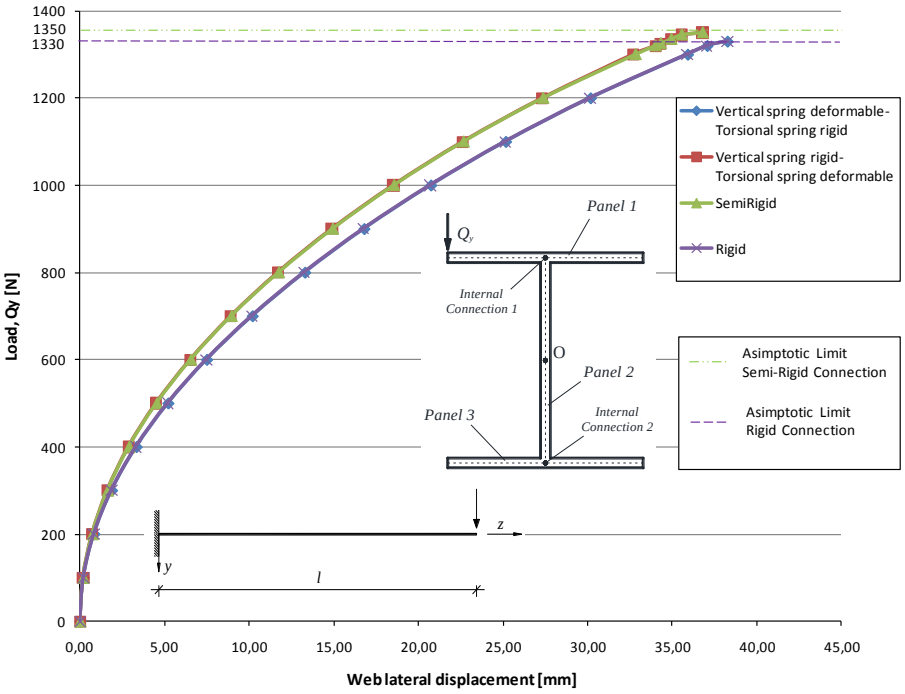

Figure 2.2. Q_y versus $u_o^{(2)}$ - Load Position 1: upper flange, eccentric.

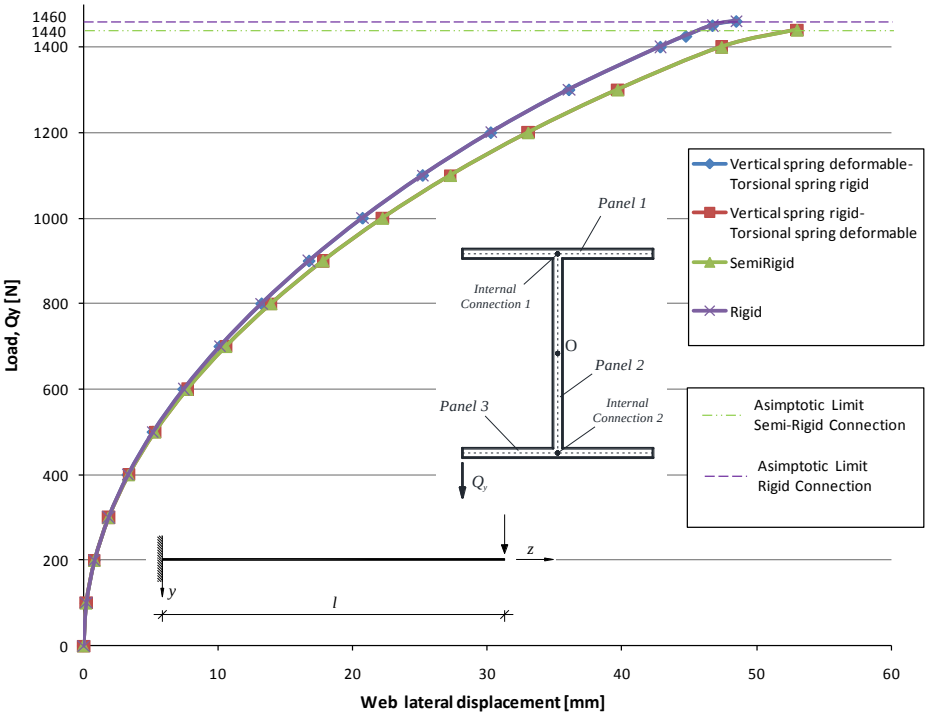

Figure 2.3. Q_y versus $u_o^{(2)}$ - Load Position 2: lower flange, eccentric.

A synoptic comparison is presented in Figure 2.4, where the results already plotted in Figures 2.2 and 2.3 are merged.

As can be seen, the responses for both Load Positions 1 and 2 agree with the same curve if the assumption of a rigid connection is considered (i.e. Case a). Of course, the buckling limits are different. On the contrary, in the presence of semi-rigid connections the corresponding curves are separated showing the opposite behavior. A numerical evaluation of such a trend is presented with reference to a load level of 1.2 kN. In particular, the solution corresponding to ten times the initial stiffness concerning Case b has been marked by dot and asterisk symbols.

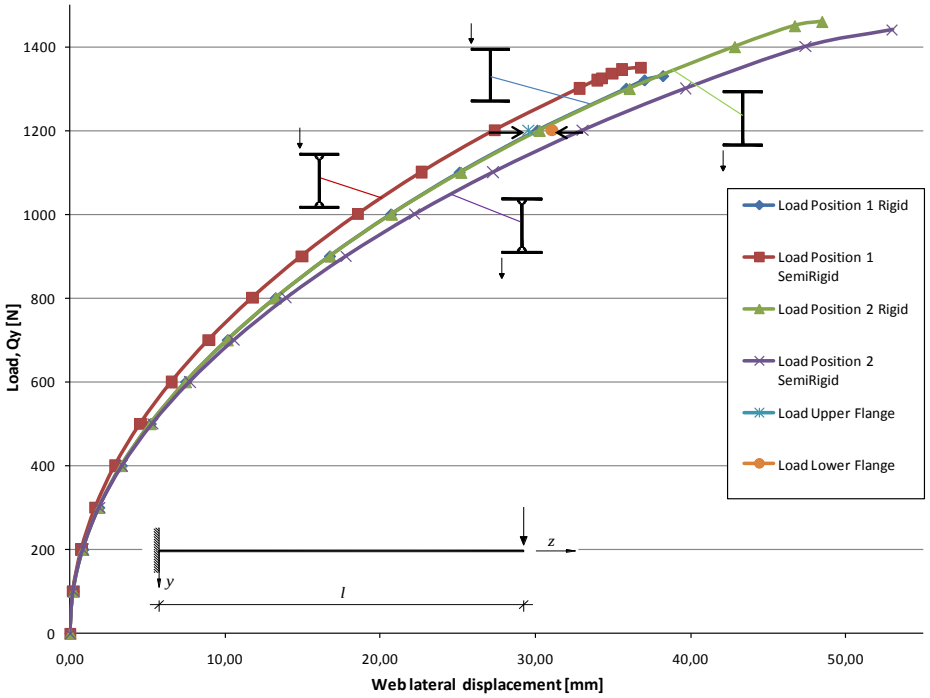

Figure 2.4. Q_y versus $u_o^{(2)}$ – global comparison.

2.2 FUTHER NUMERICAL SIMULATIONS: DEFORMED CONFIGURATION

Under the hypothesis of semi-rigid connections, due to the rotational deformability of the internal junction, the deformed configuration of the beam is attained without preservation of the angular position between two adjacent panels. This result is exemplified in Figures 2.5 and 2.6. The most relevant difference has been found to be equal to about 1.0° and it does not seem to be affected by the load position considered.

In Table 2.4, the absolute values of the centroid displacement projections along the x and y axes of each panel (upper flange, web and lower flange) relative to the deformed free end cross section are reported for both the load position and internal connection stiffness considered. The load level is equal to 1200 N, quite close to the buckling limit. Finally, Figure 2.7 shows a three-dimensional view of the deformed beam configuration relative to the hypotheses of eccentric vertical load (1200 N) applied at the upper flange and semi-rigid internal connections.

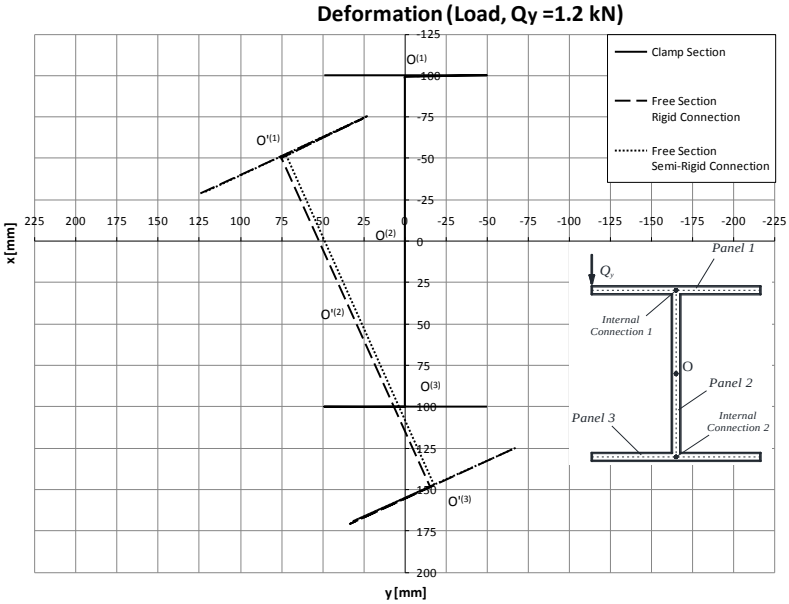

Figure 2.5. Deformed configuration: end cross section (Load Position 1).

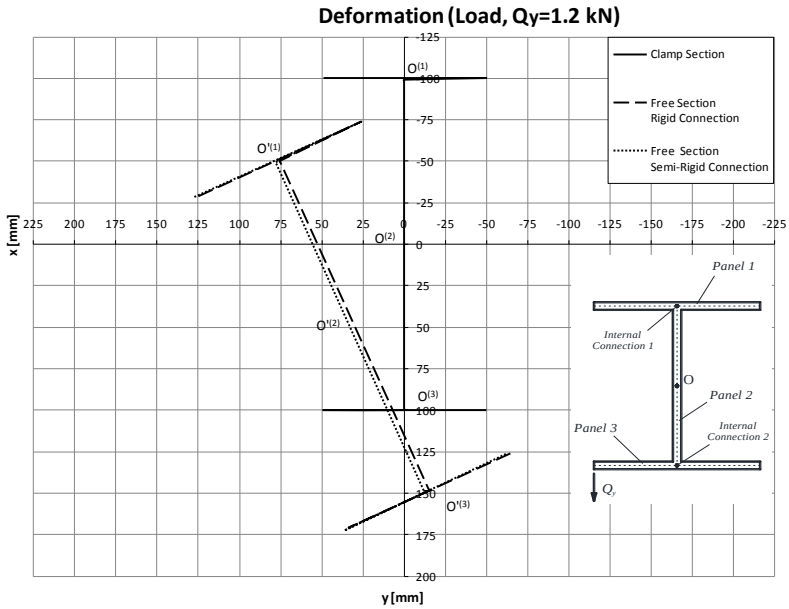

Figure 2.6. Deformed configuration: end cross section (Load Position 2).

Table 2.4. Centroid displacement projections along the x and y axes of all panels at the free end cross section.

	Centroid displacements	**Load Position 1**		**Load Position 2**	
		$\left\|\left(\overline{O^{(i)}O'^{(i)}}\right)_x\right\|$	$\left\|\left(\overline{O^{(i)}O'^{(i)}}\right)_y\right\|$	$\left\|\left(\overline{O^{(i)}O'^{(i)}}\right)_x\right\|$	$\left\|\left(\overline{O^{(i)}O'^{(i)}}\right)_y\right\|$
		[mm]	**[mm]**	**[mm]**	**[mm]**
Rigid Connection	Upper flange (panel 1)	75.70	48.57	75.87	48.56
	Web (panel 2)	30.14	48.51	30.27	48.56
	Lower flange (panel 3)	15.46	48.51	15.32	48.56
Semi-Rigid Connection	Upper flange (panel 1)	72.43	47.43	78.61	49.57
	Web (panel 2)	27.37	47.35	33.04	49.58
	Lower flange (panel 3)	17.74	47.35	12.52	49.58

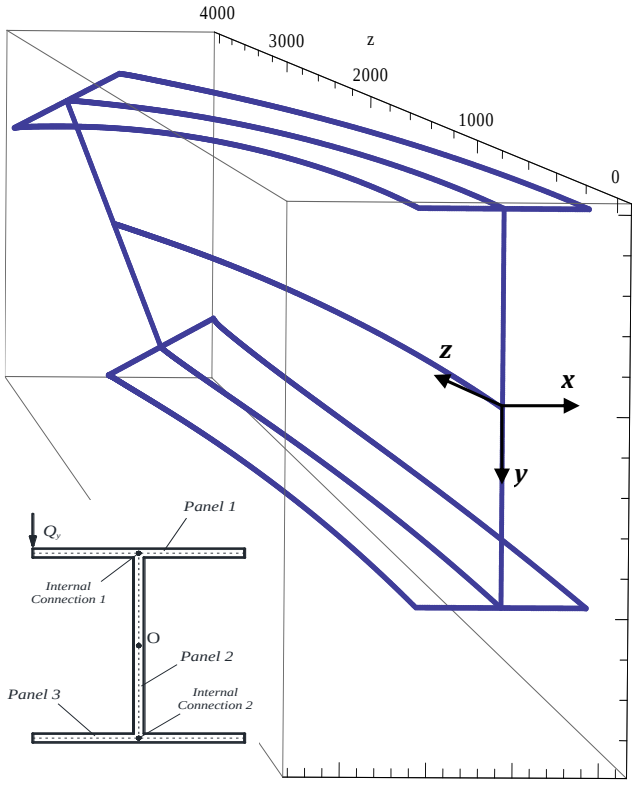

Figure 2.7. Deformed beam configuration: three-dimensional view.

2.3 CONCLUSIONS

Numerical results obtained by means of a finite element model realized *ad hoc* are relative to a cantilever beam subjected to an eccentric load (flexural/torsional coupled problem). The aforementioned results have highlighted that the pre-buckling behavior is sensitively affected by the load position in the case in which the internal connection is not perfectly rigid (the stiffer the internal connections, the lower such an effect).

Furthermore, in terms of buckling load limit, no influence seems to be related to the stiffness parameters concerning the translational spring along the web's mid-line, while a dependence emerges on the torsional stiffness parameters.
Passing from the rigid to the semi-rigid condition, the buckling load varies with a difference more or less equal to 1.5% within the numerical simulations here.

CHAPTER III

MODIFICATIONS OF STANDARD GFRP SECTIONS SHAPE AND PROPORTIONS FOR IMPROVED STIFFNESS AND LATERAL-TORSIONAL STABILITY

3. INTRODUCTION

In this Chapter the results of a comprehensive numerical investigation regarding the axial–flexural–torsional response of pultruded slender beams is presented. The goal is to propose GFRP standard cross-sections of such proportions and shapes that would possess improved strength, stability and deformational characteristics compared to the corresponding existing sections whose proportions are generally based on standard steel sections. As GFRP sections are thin-walled but are significantly less stiff than similar steel sections, the study focuses on enhancing their appropriate stiffness and buckling strength. The novel and efficient numerical model described in Chapter 1 and can be used to trace the complete pre-buckling geometrically nonlinear response of any GFRP or

steel thin-walled member with open or closed cross-section. Furthermore, the previous model is here enhanced by endowing it with the capability to predict failure initiated by instability or insufficient material resistance. For predicting material failure, the well known Tsai–Hill failure criterion is adopted.

The bucking load is computed by the asymptotic value of the load-displacement curve. Members with I-, L-, T- and box sections are analyzed, considering different loading and boundary conditions.

The new cross sections shapes were obtained identifying, via detailed analysis, appropriate geometric parameters for GFRP sections that can be judiciously selected to improve their overall resistance, stability and serviceability when subjected to axial–flexural–torsional actions. The improvements can be judged by comparing the response of the GFRP sections with enhanced properties to those of similar existing sections available commercially.

It is demonstrated that due to their unsuitable proportions, available standard GFRP sections do not have adequate stiffness and buckling strength. Consequently, recommendations are made for new sectional proportions and modified shapes, and some graphical results are presented to demonstrate how the results of the proposed method could be utilized in practical design situations.

The superiority of the proposed sections is quantified by an efficiency factor, defined in terms of ratio of strength gain to material volume increase.

Towards this end, a section efficiency factor, η, is introduced which is defined as the ratio of the increase in strength to the increase in material volume ratio. While any $\eta > 1.0$ indicates increase in efficiency, it will be shown that the proposed changes can achieve η values greater than 2. Hence, the proposed modifications can lead to more economical sections with higher mechanical performance than the standard sections currently on the market. It should be pointed out that for general shapes and boundary conditions the determination of the buckling load of thin-walled

section and the shape and proportions of the ideal section can be very complicated and may not lend itself to closed-form solution.

3.1 NUMERICAL SIMULATIONS

In this section a comprehensive numerical investigation is conducted and the foregoing model is applied to the geometrically non-linear axial–flexural–torsional equilibrium and stability of slender pultruded beam-columns. The aim is to analyse the response of such members having any of the common cross-sectional shapes available on the market, such as T-, I-, L-, and box shapes, and to recommend typical changes to their proportions or shape, with the goal of enhancing their strength, stiffness and/or stability. Based on the results of the presented analyses, improved cross-sectional proportions or alternative efficient modified shapes are proposed. It should be pointed out that the stability of a thin-walled section depends on a large number of material and geometric properties, and loading configuration of the member. The geometric properties include the section torsional, polar, and warping constants as well as its cross-sectional area, second moments of area, and the member unsupported length. These parameters cannot be optimized for every loading and geometric scenario using only one section type or proportions; nevertheless, it is possible, as shown in this investigation, to significantly improve their resistance by judicious choices of section shape and proportions.

Members with two typical support conditions are investigated, viz. cantilever (encastre) and simple supports but restrained against twisting. The members are subjected to different types of loading, including eccentrically applied concentrated and uniformly distributed vertical, or gravity, loads and eccentric axial load. Figure 3.1 depicts the various cross-sectional shapes, boundary conditions and loading cases analyzed. The mechanical properties of the analyzed steel and GFRP sections are reported in Table 3.1, while the geometric characteristics of each cross section are

summarised in Table 3.2, and the symbols in Table 3.2 are identified in Figure 3.1. Given that the focus of the present study is on the member cross-sectional shape and its proportions, for simplicity, the member length is taken as 3000 mm for all the investigated cases.

In each case the member is discretized by a mesh comprising 500 two-node finite elements. As demonstrated in [44], this mesh is deemed satisfactory for the purpose of the current analyses.

Case	Loading and Supports Cross Sections
A	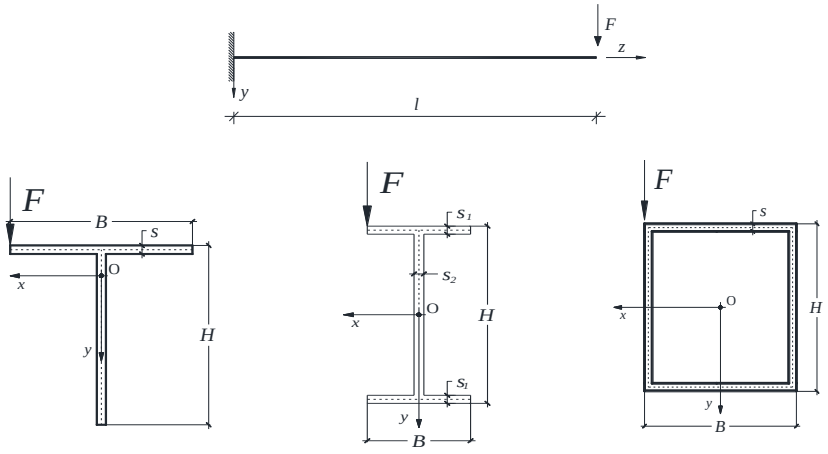
	*A*1 *A*2 *A*3
	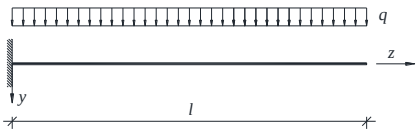
B	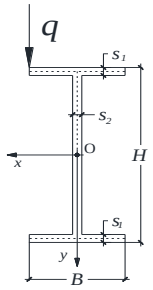
	*B*1

follow...

continue…

Case	Loading and Supports Cross Sections
C	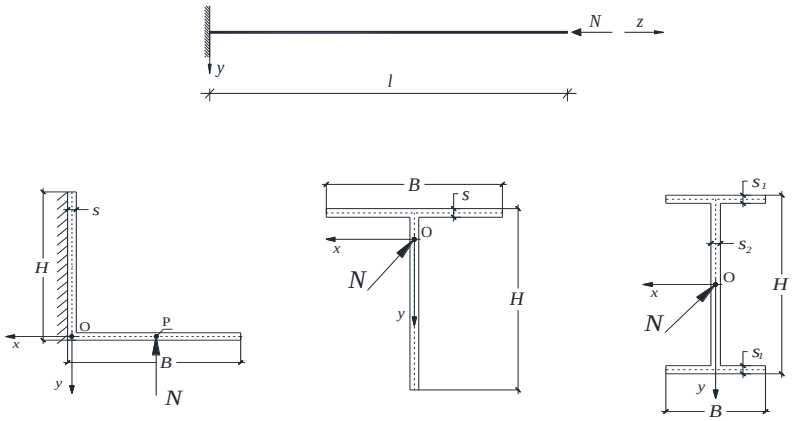
	*C*1 *C*2 *C*3
	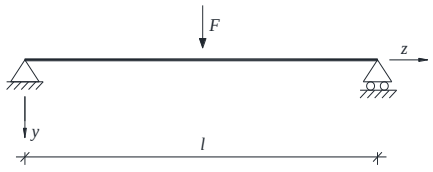
D	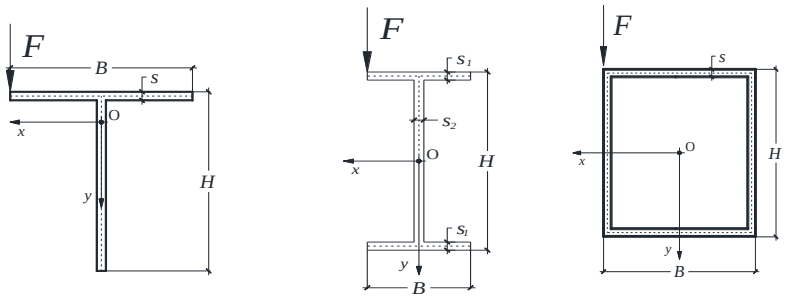
	*D*1 *D*2 *D3*

follow…

continue…

Case	Loading and Supports Cross Sections
	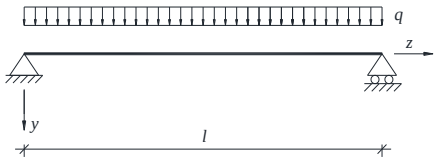
E	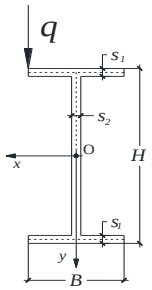
	*E*1
F	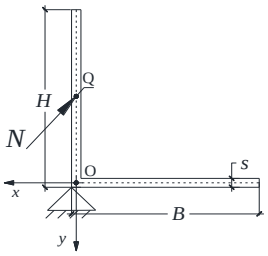
	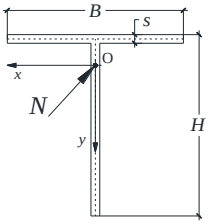
	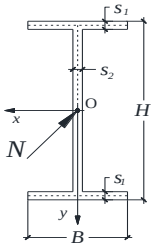
	*F*1 *F*2 *F*3

Figure 3.1. Geometry, loading and boundary conditions investigated.

Table 3.1. Steel and GFRP mechanical properties.

Steel mechanical properties			
Young's modulus of elasticity	E	MPa	210,000
Shear modulus of elasticity	G	MPa	81,000
Yield strength	f_y	MPa	275
Ultimate strength	f_u	MPa	430

GFRP mechanical properties			
Young's modulus of elasticity(*)	$E_{0°}$	MPa	23,000
Shear modulus of elasticity	G_{xz}, G_{yz}	MPa	3,000
Flexural strength(*)	$f_{b,0°}$	MPa	240
Tensile strength(*)	$f_{t,0°}$	MPa	240
Compressive strength(*)	$f_{c,0°}$	MPa	240
Shear strength	f_τ	MPa	25

(*) pulling direction during pultrusion process (axis of pultrusion)

Table 3.2. Cross section shapes and relative geometrical parameters.

Cross section shape	T		
Geometrical dimensions		measure unit	value
Flange panel width	B	mm	80.0
Flange panel thickness	s	mm	9.0
Web panel thickness	s	mm	9.0
Whole cross section height	H	mm	80

follow…

continue…

Cross section shape	I		
Geometrical dimensions		measure unit	value
Flange panel width	B	mm	100.0
Flange panel thickness	s_1	mm	8.5
Web panel thickness	s_2	mm	5.6
Whole cross section height	H	mm	200.0

Cross section shape	L		
Geometrical dimensions		measure unit	value
Horizontal panel width	B	mm	100.0
Horizontal panel thickness	s	mm	10.0
Vertical panel thickness	s	mm	10.0
Vertical panel height	H	mm	100.0

Cross section shape	Box		
Geometrical dimensions		measure unit	value
Horizontal panel width	B	mm	100.0
Horizontal panel thickness	s	mm	8.0
Vertical panel thickness	s	mm	8.0
Vertical panel height	H	mm	100.0

For each case studied the following results are reported:

- buckling load – this value was obtained as the asymptotic limit of the non-linear response predicted by the numerical model discussed in Chapter 1;
- load versus lateral and vertical displacement curves (pre-buckling behaviour);
- 3D deformation view;
- for a selected GFRP cross section the computation of the stress field for several load levels up to failure and comparison with Tsai–Hill failure criterion. This was accomplished by using Eq. (3.1) in conjunction with the computed values of the tangential stresses τ_{nz} and τ_{tz} and the normal stress σ_n.

Although the described model is able to account for panel internal connections deformability, the web–flange junctions in the current study are treated as rigid to allow comparison with similar steel sections which are deemed to possess rigid connections. However, the influence of the connection deformability has been examined and quantified in [44].
In the following subsection, for brevity only the results for the cantilever beam-columns (case A of Figure 3.1) are discussed in detail. The results pertaining to all other cases investigated can be found in Appendix A. It should be emphasized that the following comments and discussion presented for the cantilever case also apply generally to the members with other types of boundary conditions, albeit the achieved efficiency may not be the same.

3.2 CASE A: -T, -I AND BOX CROSS SECTIONS

For the cantilever beam-columns, the results for cases A1, A2, and A3 in Figure 3.1, including the magnitude of the critical applied load, F_{crit}, for each cross section, are reported in Table 3.3. In each case, the table lists the selected commercially available standard steel and GFRP sections and their dimensions, followed by a number of analogous GFRP shapes with modified dimensions, and finally a similar but more efficient shape proposed based on the results of the current analyses. The standard sections are simply termed Steel and GFRP while the modified GFRP sections are dubbed "GFRP*i*". Note, in the table for each cross section the dimensions that are altered, compared to the corresponding standard section dimensions, are underlined. Finally, in each case the ratios of the volume and critical load of each modified section to the volume and critical load of the corresponding standard section are computed and shown in columns 5 and 4 of Table 3.3. Section efficiency factor η, defined as the ratio of increase in volume to increase in critical load, is indicated in the last column of the table. Note that η values greater than one indicate more efficient section than the corresponding standard section.

Table 3.3. Cantilever beam-columns: cross sectional shape, dimensions and relative buckling loads.

Case studied		Cross-section Dimensions [mm]	Load^{crit}	$\frac{L^{crit}_{GFRPi}}{L^{crit}_{GFRP}}$	$\frac{V_{GFRPi}}{V_{GFRP}}$	η
		(H x B x s)	**F^{crit}**			
			[kN]	**[-]**	**[-]**	**[-]**
	Steel	(80 x 80 x 9)	2.40	-	-	-
	GFRP	(80 x 80 x 9)	0.34	1.00	1.00	1.00
	GFRP*1*	(80 x 80 x 18)	0.65	1.91	1.88	1.02
A1	GFRP*2*	(160 x 80 x 9)	0.40	1.17	2.94	0.40
(T-section)	GFRP*3*	(80 x 80 x 27)	0.90	2.65	2.64	1.00
	GFRP*4*	(120 x 80 x 13.5)	0.80	2.35	1.85	1.27
	GFRP*5*	(80x 120 x 9)	0.40	1.17	1.26	0.92
	GFRP*6*	(80 x 120 x 13.5)	0.80	2.35	1.85	1.27
	GFRP*7*	(proposed new shape, see Figure 5)	1.80	5.29	3.22	1.64
		(H x B x s_1 x s_2)	**F^{crit}**			
			[kN]	**[-]**	**[-]**	**[-]**
	Steel	(200 x 100 x 8.5 x 5.6)	12.00	-	-	-
	GFRP	(200 x 100 x 8.5 x 5.6)	1.05	1.00	1.00	1.00
	GFRP*1*	(200 x 100 x 17 x 11.2)	5.00	4.76	1.93	2.47
A2	GFRP*2*	(400 x 100 x 8.5 x 5.6)	1.00	0.95	1.41	0.67
(I-section)	GFRP*3*	(200 x 100 x 25.5 x 16.8)	10.00	9.52	2.79	3.41
	GFRP*4*	(200 x 200 x 8.5 x 5.6)	4.00	3.80	1.62	2.34
	GFRP*5*	(200 x 200 x 17 x 11.2)	14.00	13.33	3.18	4.19
	GFRP*6*	(proposed new shape, see Figures 6)	5.50	5.24	3.74	1.40

follow…

continue…

Case studied	Cross-section Dimensions [mm]		Load^{crit}	$\frac{L_{GFRPi}^{crit}}{L_{GFRP}^{crit}}$	$\frac{V_{GFRPi}}{V_{GFRP}}$	η
		(H x B x s)	**F^{crit} [kN]**	**[-]**	**[-]**	**[-]**
A3 (Box-section)	Steel	(100 x 100 x 8)	14.00	-	-	-
	GFRP	(100 x 100 x 8)	1.00	1.00	1.00	1.00
	GFRP*1*	(100 x 100 x 16)	3.75	3.75	1.83	2.05
	GFRP*2*	(100 x 200 x 8)	2.00	2.00	1.54	1.30
	GFRP*3*	(200 x 100 x 8)	2.00	2.00	1.54	1.30
	GFRP*4*	(200 x 200 x 10)	6.50	6.50	2.58	2.52

In Figures 3.2 to 3.4 the load versus displacement curves for each analysed case are reported. In Figure 3.2a the applied load *F*-lateral displacement, *u*, curve for point P on the flange, and in Figure 3.2b the load *F*-vertical displacement, *v*, curve for point O on the web are plotted. The above displacements are at the free end of the cantilever.

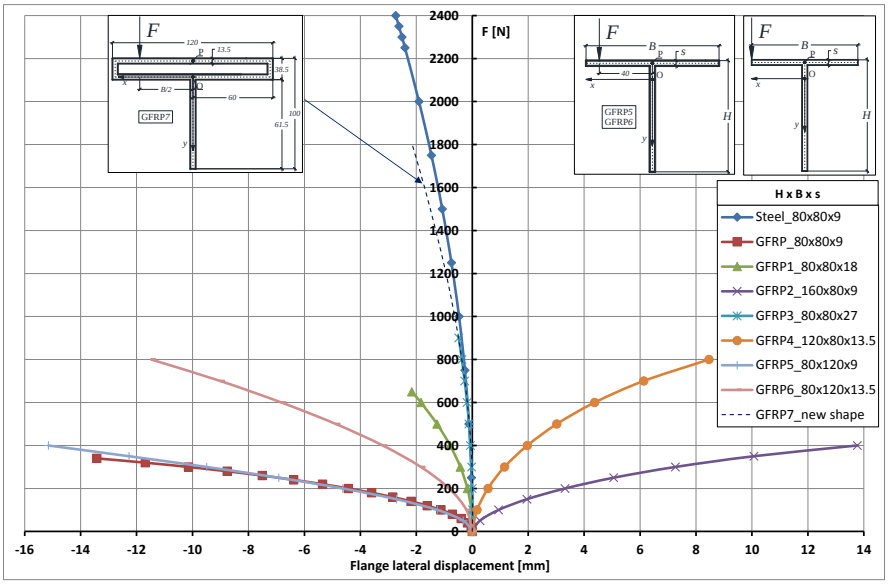

Figure 3.2a. Case A1 – Load *F* versus lateral displacement, *u,* at point P on the flange.

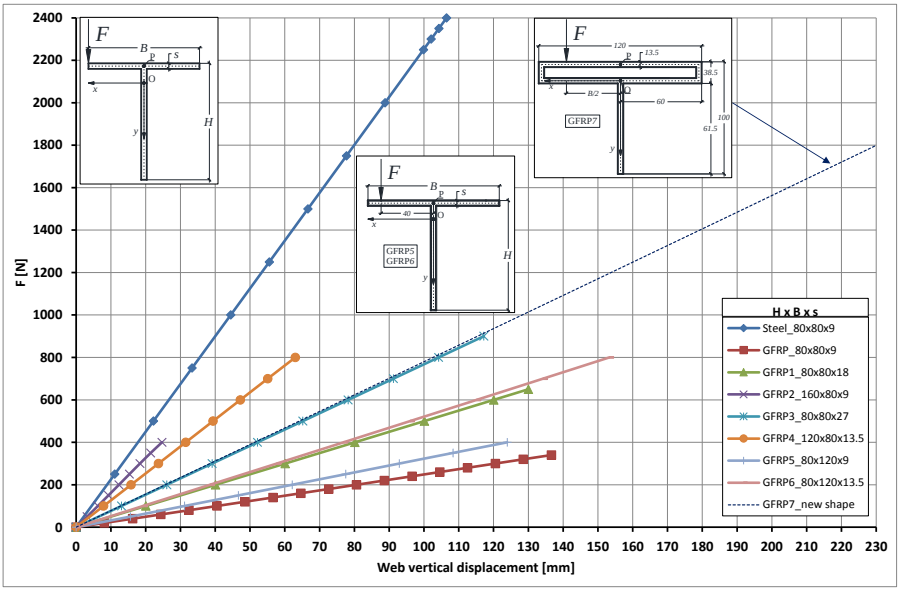

Figure 3.2b. Case A1 – Load *F* versus vertical displacements, *v,* at point O on the web.

Notice the nearly fivefold increase in F_{crit} and the threefold increase in stiffness of the proposed new T-shape compared to the standard section. The new section uses approximately three times more material than the standard section but has over five times higher critical load, with η=1.64.
The modified section GFRP4 uses instead two times more material than the standard section but has two times higher critical load, hence its η=1.27. Furthermore, compared to modified section GFRP4, the proposed section contains 74% more material, but its critical load is 225% higher. In fact, it is worth noting that F_{crit} for the new shape is 75% of the critical load of the companion steel section while F_{crit} for the GFRP4 shape is 33% of that of steel section. This is possible because the new cross section presents an innovative shape where the torsional and flexural stiffness are both increased in a balanced manner. Note that Figure 3.2a and 3.2b may be also used to examine the effects of certain changes in the standard T-section dimensions on its deformation, stiffness and stability.
Figures 3.3 and 3.4 show results for I- and box-section, respectively, similar to the results in Figure 3.2 for the T-section, with improved stiffness, strength and critical load for each proposed new section. For the I-section a 424% increase in the buckling load can be observed compared to the standard section. For the box section, no new shape is proposed but the section dimensions are modified to allow achieving different buckling loads.

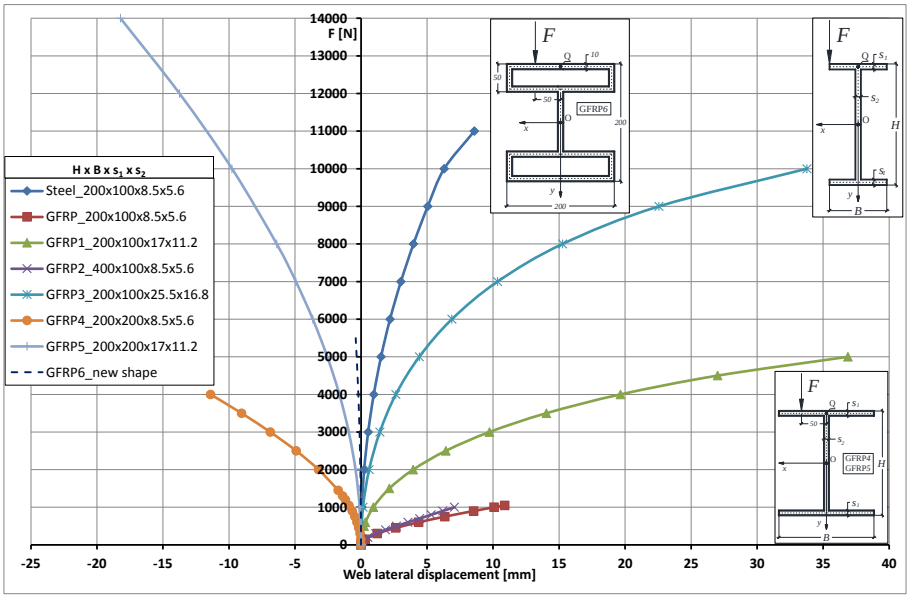

Figure 3.3a. Case A2 Force F versus lateral displacements *u* at point O on the web.

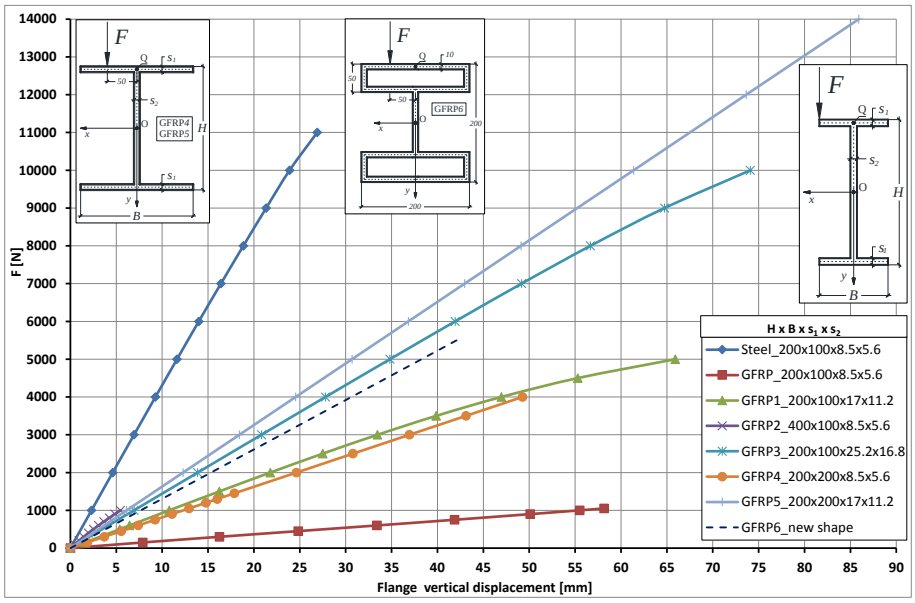

Figure 3.3b. Case A2 – Force F versus vertical displacements *v* of point Q on the flange.

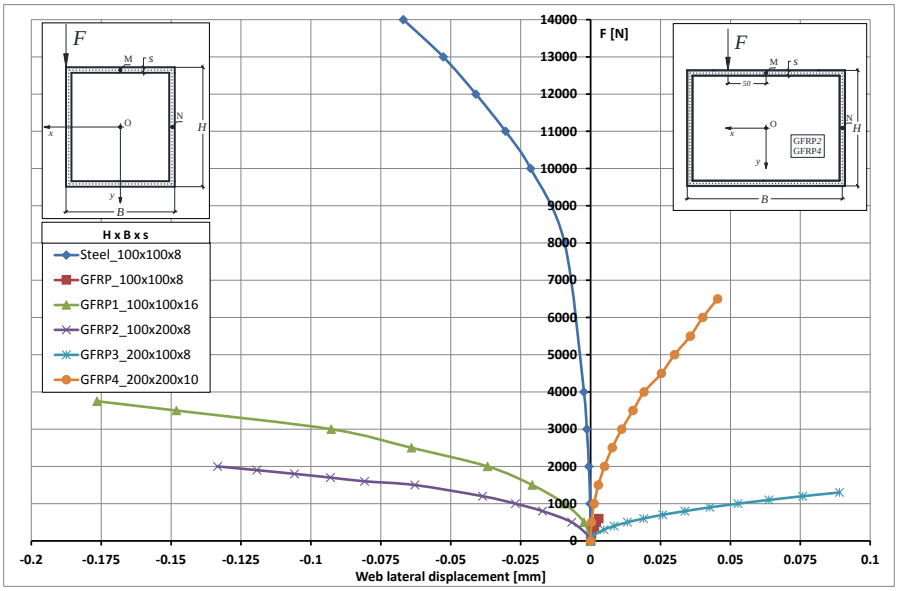

Figure 3.4a. Case A3 – Force F versus lateral displacements *u* of point N on the right web.

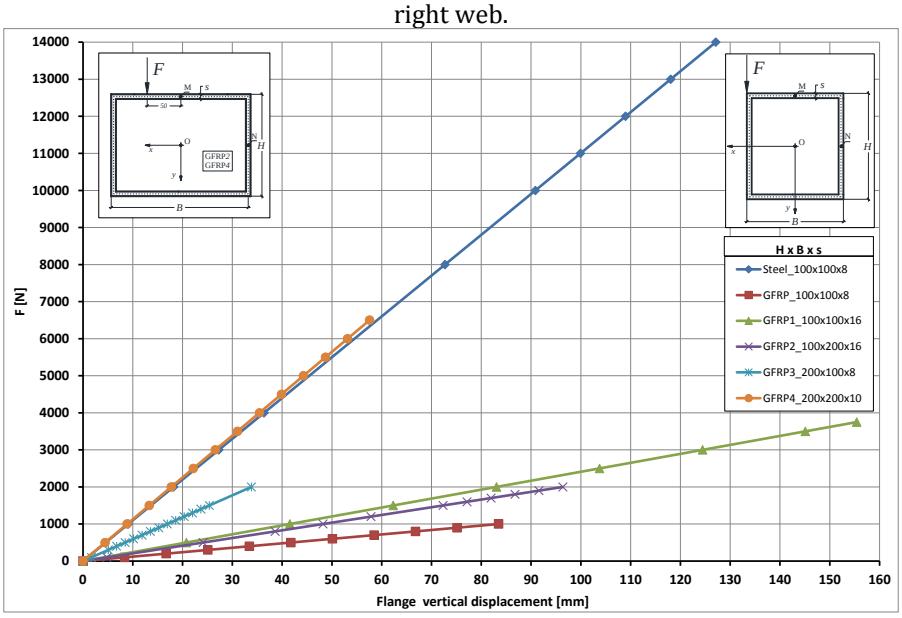

Figure 3.4b. Case A3 – Force F versus vertical displacements *v* of point M on upper flange.

It is worth noting that compared to the standard steel section, in each case the worst response, in terms of strength and stiffness, is exhibited by the companion standard GFRP section, which supports the argument that the current commercially available GFRP sections are not properly shaped or proportioned, at least from the perspective of lateral-torsional stability. If the intent of the current selection of GFRP standard sections is to mimic analogous steel sections, they fall dramatically short of having comparable performance insofar as buckling strength and stiffness are concerned. For example, the numerical results presented in Figures 3.2 show that in the case of the T-cross section, deformation control is governed by the vertical displacement *v*, which appears to be about 10 times higher than the horizontal displacement *u*. The global buckling is instead governed, as expected, by the second moment of area about the minor axis of bending. Thus, the numerical results lead one to state that with reference to the standard GFRP T-section:

- increasing thickness, *s*, decreased vertical displacement, *v* , but increased both the buckling load (approximately 165% when *s* is increased threefold) and horizontal displacement, *u,* although the increase in *u* has marginal effect on the deflection limit.
- increasing the width, *B*, 150% increased the buckling load by 17% while neither displacement, *u*, nor and *v* changed significantly;
- increasing the height, *H,* 200% increased the buckling load 17% and reduced the vertical displacement, *v,* dramatically as it approached the corresponding displacement of the companion steel section.

The other modification to the standard cross sectional dimensions investigated in this study involves changes to more than one geometric parameter (*s* and *B*, or *s* and *H*) concurrently, which result in varying degrees of improvement in the section performance as shown in Figures 3.2. Overall, increasing thickness *s* may be the best choice. Alternatively, if

possible, it is advantageous to modify the cross-sectional shape as illustrated by the shape GFRP7 in the current study.
The results in Figures 3.3 for the I-cross section show that deformability is equally governed by the vertical and horizontal displacement, *v* and *u*, respectively. As in the previous case, the results for case A2 lead one to state that:

- increasing the thicknesses s_1 and s_2, threefold increased the buckling load approximately nine times.
- increasing the width *B* of the flanges by making them equal to the height *H* of the cross section increased the buckling load fourfold and led to improvement in the member deformability;
- increasing the section height *H* 200% did not change the buckling load noticeably, but it led to significant reduction in the member's vertical and lateral deformations, approaching the corresponding deformations of the standard steel section.

In contrast to case A1, where it was not possible to identify the optimum cross sectional geometry that would yield the best combination of strength and stiffness for a pultruded slender beam, in this case, by varying both the width, *B*, of the flanges as well as thicknesses s_1 and s_2 simultaneously, it was possible to obtain the cross section "GFRP*5*", which significantly enhances the forgoing characteristics of the section with respect to flexural–torsional behaviour. Alternatively, "GFRP*6*" in Figures 3.3 shows a complete redesign of the I-shape, where the original I-cross section is changed to an H- section. As noted earlier, this change resulted in a dramatic increase in the buckling load and a similarly large reduction in the member displacements, without proportional increase in the amount of material used. Finally, the results in Figures 3.4 indicate that compared to the standard box section, the member deformations are substantially governed by the vertical displacement, *v*, which appears to be about 1,000 times bigger than the horizontal displacement, *u* while global buckling is

governed, as expected, by the second moment of area about minor axis of bending.
With reference to the case A3 results, the following comments are pertinent:

- increasing the thickness *s*, increased the buckling load and reduced the member horizontal and vertical displacements. For example, doubling *s* increased the buckling load 275%, hence, it can be claimed that η for the new section is 2.05;
- increasing the width, *B*, and height, *H*, of the box, as well as its walls thickness modestly, led to dramatic increase in the buckling load and equally dramatic reduction in displacements. For example, doubling the box height and width and increasing their thickness by 25%, for a total increase of 158% in material volume, increased the buckling load 550% and reduced vertical deflection by 842%. In other word, the section efficiency was 2.52 and 3.26 with respect to the buckling load and vertical deflection, respectively.

It is important to remark that the curves in Figure 3.2a, with specific reference to the cross sections "GFRP*2*" and "GFRP*4*", show a reversal in the direction of lateral displacement, *u*, when compared to the other cross-sections in the same case. This reversal is expected and is caused by the increase in the value of the height H. This circumstance is clarified by the 3D illustrations of the deformed shape of sections "GFRP" and "GFRP*4*" close to their critical loads.

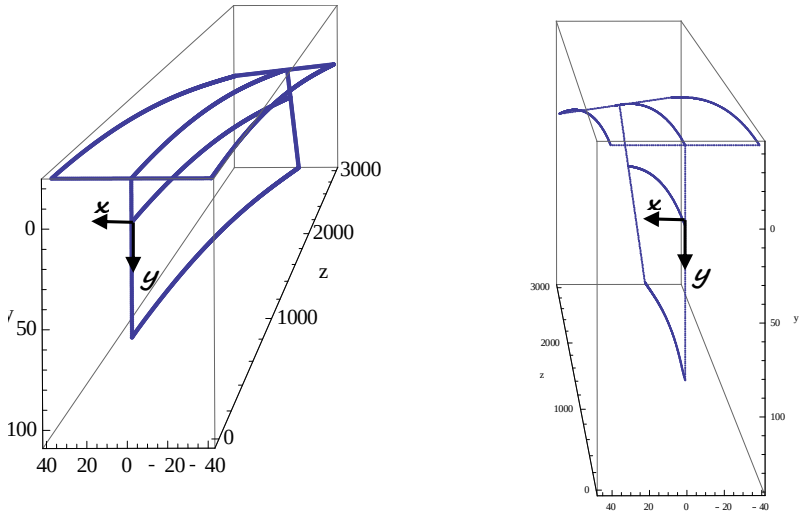

a) "GFRP" – F=120 N b) "GFRP*4*" – F=700 N

Figure 3.5. Case A1 – 3D view of the deformed beam near buckling.

The above comments related to deformation reversal also apply to the curves in Figure 3.3a and 3.4a, which illustrate the results for sections "GFRP*4*" and "GFRP*5*" for case A2, and for sections "GFRP", "GFRP3", and "GFRP*4*" for case A3, respectively. In case A2 the change in sign of the horizontal displacement, *u*, is due to a decrease of the height, *H* (Figure 3.6), while in case A3 (Figure 3.7) it is caused by the increase in the same quantity.

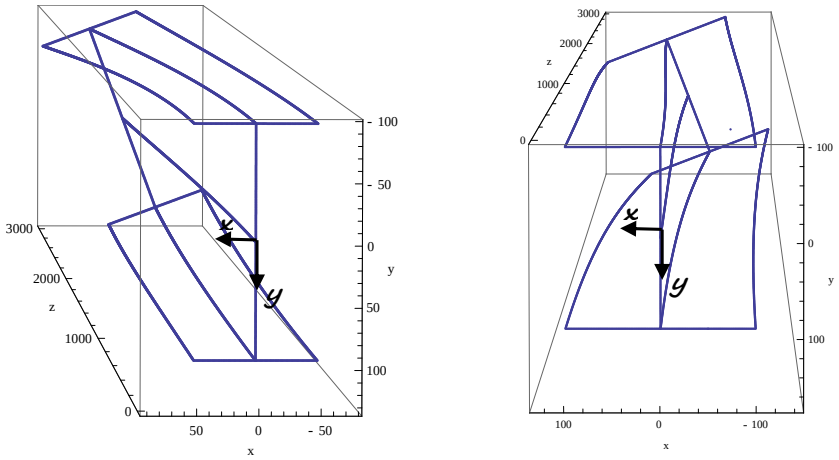

a) "GFRP" – F=0.75kN b) "GFRP*5*"– F= 3 kN

Figure 3.6. Case A2 – 3D view of the deformed beam near buckling**.**

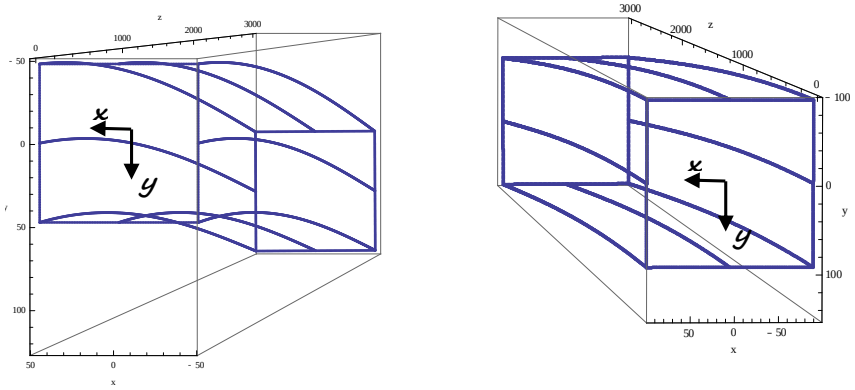

a) "GFRP" – F=0.9 kN b) "GFRP*4*" – F=6.0 kN

Figure 3.7. Case A3 – 3D view of the deformed beam near buckling**.**

Finally, in Figures 3.8 and 3.9 the failure envelope based on Tsai-Hill criterion and the associated stresses for the "GFRP*3*" (case A1) and "GFRP*5*" sections (case A2) are presented. This information for case A3 is not presented because the optimized GFRP shape in this case is already available on the market. With reference to the latter figures, on the horizontal axis the shear stress, $\left(\tau_{nz}+\tau_{tz}=\tau\right)$, and on the vertical axis the flexural stress, σ_n , are plotted. The points on the envelope represents the locus of τ and σ_n, which satisfy Eq. (3.1).

$$\left(\frac{\sigma_n}{f_{b,0}}\right)^2+\frac{\left(\tau_{nz}^2+\tau_{tz}^2\right)}{f_\tau^2}=1 \tag{3.1}$$

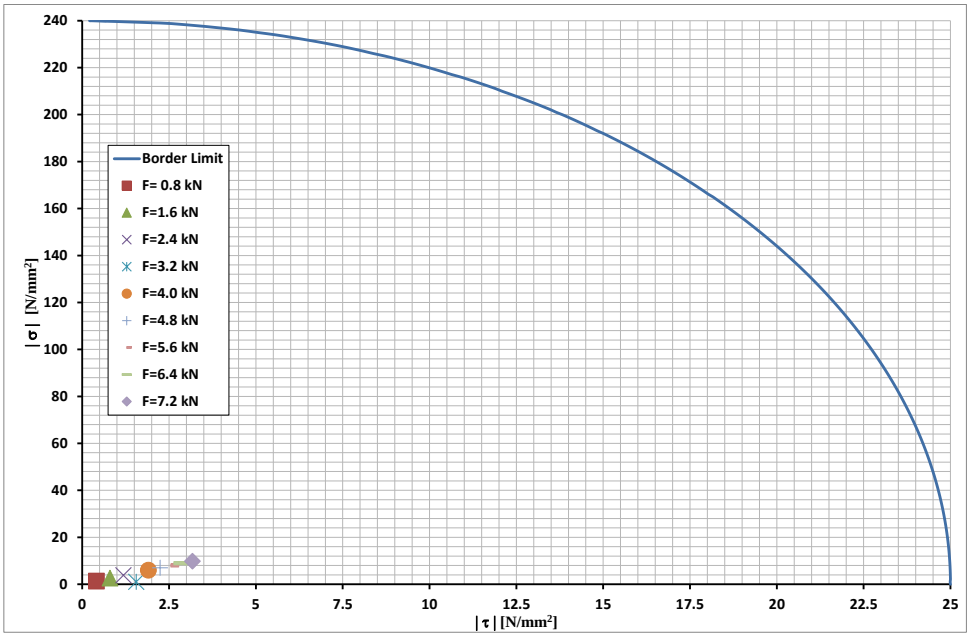

Figure 3.8. Case A1 – Actual stress at buckling and the failure envelope of the "GFRP*3*" section.

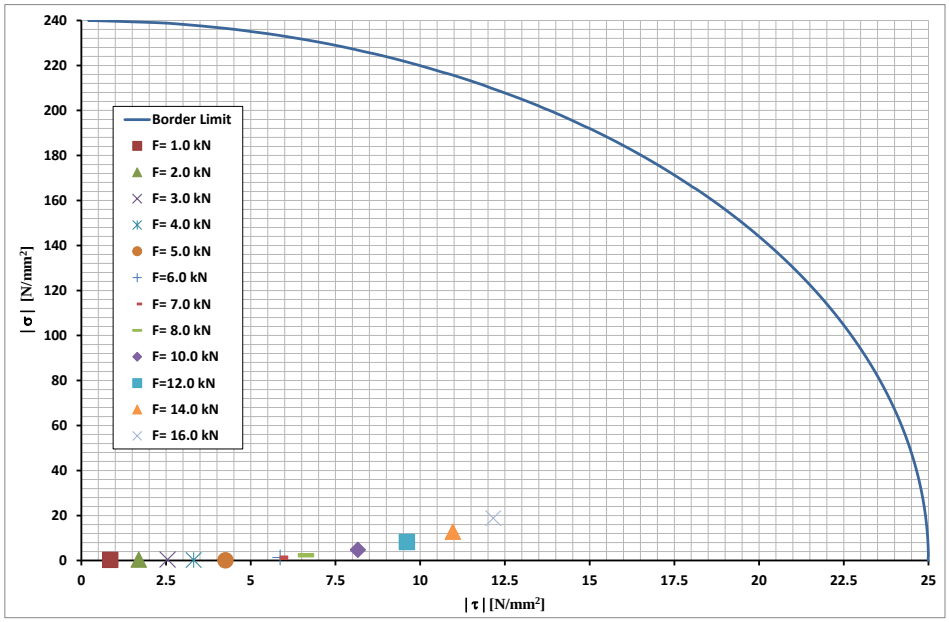

Figure 3.9. Case A2 – Actual stresses at buckling and the failure envelope of the "GFRP*5*" section.

Notice that the actual stresses in these sections, indicated in Figures 3.8 and 3.9 by the relevant symbols, are much less than those required causing failure of the GFRP due to overstress. This finding is not entirely unexpected, for it is well known that failure of slender GFRP sections is governed by buckling and instability rather than loss of material strength. Accordingly, optimization of GFRP sections dimensions and shapes should be based on increasing their buckling load and stiffness as demonstrated in the current study.

In addition to the above results, other possible cross section modifications and their results are presented for some typical sections in Appendix A. For example, the standard T- section was changed to a section with its web unchanged but its flange converted to a box; the I-cross section was changed to an H-cross section, with the same web and flanges but made into a box shape. Finally, the L-cross section was modified to a section that

consisted of a closed section made by connecting the two flanges by means of another rectangular panel. In all of these cases the section efficiency is greatly increased and its responses are characterised by limited deformability and a high safety margin with respect to buckling.

3.3 CONCLUSIONS

In this chapter a comprehensive numerical investigation is performed to analyze the deformations and stability of pultruded slender beams subjected to combined axial–flexural–torsional actions and how changes in the dimensions and shape of their cross-sections affect their stability and stiffness. The overall objective was to identify several GFRP cross section geometries by modifying the current standard GFRP shapes available on the market (i.e. those similar to steel cross section shapes), in order to improve their mechanical behaviour. The sections analyzed includes pultruded slender T-, I-, L- and box shapes. Cantilever and simply supported beam-columns (with torsional restraint at the supports) were analyzed subjected to the following loading conditions: eccentric gravity concentrated or uniformly distributed load, producing bending shear and torsion, and eccentric axial load. The numerical analyses were performed using a new numerical model, developed by the authors. The model is capable of predicting the nonlinear pre-buckling behaviour of generic composite beam-columns with open or closed cross-section of arbitrary shape. The numerical results lead to the following general conclusions irrespective of the loading and boundary conditions:

- standard GFRP T-section is not a suitable choice for full scale FRP structures; however, increasing the flange thickness thicknesses (e,g. doubling) and making the width of the flange, *B*, and the height, *H*, of the whole cross section equal, increases the buckling

load by only 20% but causes noticeable reduction in the relevant deformations;

- for higher efficiency and improved performance, the GFRP I-section should be converted to an H-section with the thicknesses of the flanges and web made approximately 30 mm (three times the current values). This modification could lead to a buckling load about 13 times greater than that of a similar existing GFRP cross sections as well as a sensible reduction in member deformations;
- the GFRP L-section is not suitable for applications in structures within civil infrastructure. Varying the thickness as well as the width of the flanges produces no major advantages in terms of buckling load and reduction of deformations.

Part of the goal of this investigation is to initiate discussion about the right shape and proportions of GFRP pultruded cross-sections. We believe that section shapes and dimensions should be selected based on the mechanical properties of FRP and not by mimicking steel sections. Therefore, we hope that this would eventually lead to radical changes and rethinking in the production of pultruded composite sections, giving them their appropriate place within the constellation of structural shapes available to structural designers.

PART II

NEW GFRP PULTRUDED BEAMS

A low-cost design strategy inspired by modularity, able to exploit the immediate availability of "ready-to-use" standard components, plays a crucial role for the large-scale viability of FRP structures. The idea discussed in the Chapter IV and V is focused exactly on the possibility of achieving a complex FRP shape by bonding an appropriate number of simple pultruded shapes with a common epoxy glue.

The Part II has been developed within a multi-phase comprehensive joint research program between University of Salerno and the Laboratory of Mechanics and Acoustics of CNRS (Aix Marseille University), in Marseille, France.

CHAPTER IV

GFRP BEAMS OBTAINED BY BONDING SIMPLE PANELS: THE I- CROSS SECTION CASE

4. INTRODUCTION

Nowadays, because the industrial process is optimized for mass pultrusion of a limited number of shapes, it is difficult to produce complex shapes with standard cost targets.

Furthermore as mentioned previously in the summary, in the civil structures, pultruded profiles were joined together to form more complex cross-sections. For example, in the Fiberline bridge, the arches and the tied longitudinal bridge deck girders were made of a rectangular hollow FRP cross-section obtained from two U-profiles joined together with two bonded flat plates to form the rectangular tubular section.

The idea discussed in this Chapter is focused exactly on the possibility of achieving a complex FRP shape by bonding an appropriate number of simple pultruded shapes with a common epoxy glue. For example, a generic

I-profile may be obtained by bonding three rectangular panels (the top/bottom flanges and the web panel), rather than via a unique pultrusion application. In addition, web-to-flange junctions may also be strengthened by bonding appropriate angle profiles. In this view, the possibility of considering composite profiles of a generic cross-section from simple rectangular panels would be an interesting constructive simplification.

Therefore, the aim of this study is to answer the following two questions.

The first is "what performance level can be achieved for bonded composite beams compared to similar pultruded ones?". As mentioned in the Summary, from a mechanical point of view, both FRP pultruded beams and bonded ones can be considered as linear elastic, homogeneous and transversely isotropic, with the plane of isotropy being normal to the longitudinal axis (i.e. the axis of pultrusion) [45-46]. Moreover, the mechanical behaviour of pultruded profiles, especially in the case of open profiles, is highly affected by warping strains as well as shear deformations [34]. Finally, the low values of the shear moduli (more or less the same as polymeric resin), coupled with the time-dependent nature of the mechanical behaviour, can cause non-negligible increases in lateral deflections, thus affecting both the local and global buckling loads [47-49]. As a consequence, FRP beams exhibit a complex behaviour related to a multi-interaction between shear deformability, warping, non-uniform torsional rigidity and creep. Other topics in the literature deal with possible rotations and/or sliding at panel-to-panel interfaces [43],[50]. A possible consequence is the decrease of the flexural stiffness. The second question is: "can this loss of stiffness affect the pre-failure response and the failure loads of bonded beams?".

Even though many efforts have been made to study the behaviour of full-FRP structures from the numerical and theoretical point of view, the experimental findings available in the literature on this topic are still very limited [51-52].

For this reason, was born the necessity of initiating an experimental investigation in order to compare the flexural behaviour of pultruded FRP

profiles with that of bonded FRP profiles. The results have shown the possibility of achieving a very good performance, in terms of both failure load and flexural stiffness, allowing us to consider the bonding system proposed as highly competitive in the field of construction of pultruded profiles.

This chapter presents some experimental results dealing with the mechanical performance of composite beams obtained by bonding Glass Fibre Reinforced Polymer (GFRP) rectangular pultruded panels by means of an epoxy structural adhesive. The flexural response of these bonded beams was compared with those obtained by the pultrusion process with the same geometrical and material properties. As a matter of fact, no significant loss of performance emerged in terms of failure load; moreover, an increase of pre-failure stiffness was observed. This result may allow us to consider bonded GFRP beams as a viable simplification within the field of composite structures.

4.1 EXPERIMENTAL PROCEDURES

4.1.1 MATERIALS

The experimental investigation presented in this paper deals with four point bending tests performed on Glass FRP beams. More specifically, the flexural behaviour of two different groups of beams was investigated:

- Type 1 (pultruded I-beams) entirely manufactured by the pultrusion process;
- Type 2 (bonded I-beams) obtained by bonding simple rectangular pultruded panels.

In both cases the *E-glass G967P* reinforcement is considered, with a volume fraction of 60%, whereas the remaining volume is made of an *isophalic polyester P4506 Firereta* matrix. The colour is *light grey RAL 7035* with a veil surface. As concerns the bonding of simple panels (Type 2 beams), the structural adhesive adopted is *Sikadur-30* provided by *Sika Ltd*.

More detailed information about the above-mentioned beams is presented in the next two sections.

4.1.2 PULTRUDED I-BEAMS (TYPE 1)

These beams were obtained entirely by the pultrusion process. The cross-section shape is depicted in Figures 4.1a and 4.1b, and the geometrical dimensions and mechanical properties are reported in Table 4.1, as declared by the producer. A total of four pultruded I-beams were considered in this study.

Table 4.1. Pultruded beam (Type 1) properties provided by the producer.

Cross-section shape	I		
Geometrical dimensions		measure unit	value
Flange width	B	mm	100
Height	H	mm	200
Flange thickness	t_1	mm	10
Web thickness	t_2	mm	10
Radius	R	mm	10
Mechanical properties			
Young's modulus of elasticity(*)	$E_{0°}$	MPa	28000
Shear modulus of elasticity	G_{xz},G_{yz}	MPa	3000
Flexural strength(*)	$f_{b,0°}$	MPa	240
Tensile strength(*)	$f_{t,0°}$	MPa	240
Compressive strength(*)	$f_{c,0°}$	MPa	240
Shear strength	f_τ	MPa	25

(*) pulling direction during pultrusion process (axis of pultrusion)

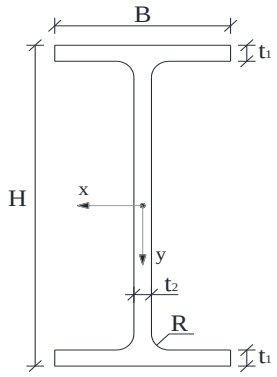

Figure 4.1a. Type 1 beam – cross-section.

Figure 4.1b. Type 1 beam – photo.

4.1.3 BONDED I-BEAMS (TYPE 2)

These beams were created by bonding three simple pultruded panels. It is important to underline that the final shape is essentially the same as that of the previous beams (Type 1 beams), except for the rounded web–flange zones. The cross-section shape is depicted in Figures 4.2a and 4.2b and the geometrical and mechanical properties are reported in Table 4.2.

Table 4.2. Bonded beam (Type 2).

Cross-section shape	I		
Geometrical dimensions (measured by the authors)		measure unit	value
Flange panels width	B	mm	100
Web panels height	h	mm	176
Flange panels thickness	t_1	mm	10
Web panels thickness	t_2	mm	10
Radius	R	mm	10
Glue thickness	t_3	mm	2
Whole cross-section height	H	mm	200
Simple panels mechanical properties (provided by the producer)			
Young's modulus of elasticity(*)	E_{0°	MPa	28000
Shear modulus of elasticity	G_{xz},G_{yz}	MPa	3000

(*) pulling direction during pultrusion process (axis of pultrusion)

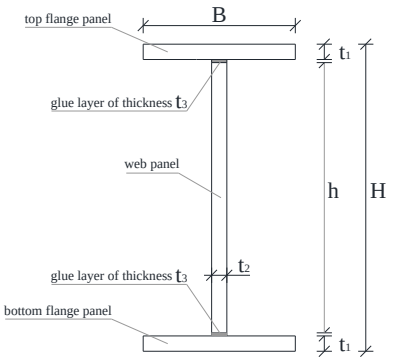

Figure 4.2a. Type 2 beam – cross-section.

Figure 4.2b. Type 2 beam– photo.

4.1.4 PREPARATION OF THE BONDED BEAMS (TYPE 2)

The bonded beams were manufactured in three steps.
The first step deals with the preparation of all components (cleaning and measuring).
Next, the bonding of the first flange to the web panel (Figure 4.3a) is carried out (Step 2). The bonding procedure was assisted by temporary constraints provided by two lateral steel angle profiles (Figure 4.3c), aimed to ensure the orthogonality between the two panels. At this stage, careful control of the adhesive thickness was also performed.
After 24 hours, the other flange was bonded at the opposite side (Figure 4.3b), according to the same sequence described above (Step 3).

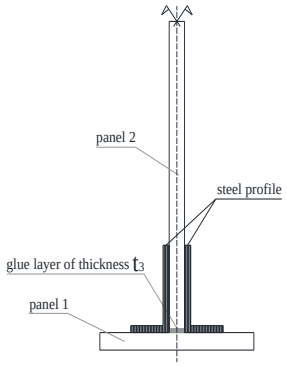

Figure 4.3a. Type 2 beam – step 2**.**

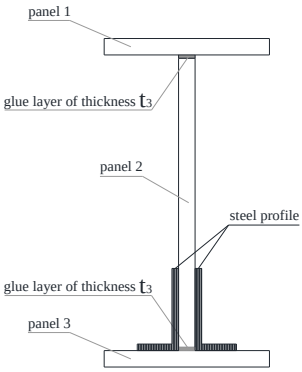

Figure 4.3b. Type 2 beam – step 3.

Figure 4.3c. Type 2 beam – steel angle profiles (photo).

A total of six bonded I-beams were assembled, four of which were further strengthened by adding an adhesive curb (Sikadur-30) at the web-flange junction on both the left and right sides, as shown in Figures 4.4a and 4.4b.

Figure 4.4a. Web–flange reinforcement – cross end view.

Figure 4.4b. Web–flange reinforcement – frontal view.

The dimensions of the curb were 10 mm × 10 mm over the full length of the beam (1400 mm). The main idea was to simulate the role played by the rounded web–flange zones in pultruded beams (Figure 4.5).

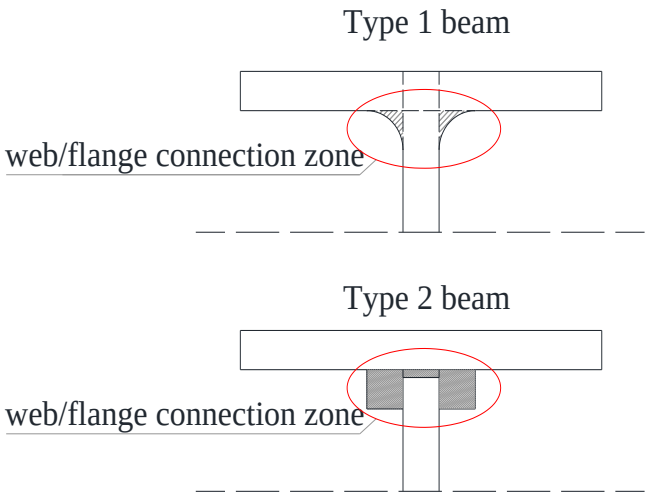

Figure 4.5. Web–flange connection zone in Type 1 and Type 2 beams.

Type 2 beams were cured over 7 days, with the room temperature kept constant at a value falling in the range indicated by the Sikadur-30 datasheet (15°C – 30°C).

4.2 EXPERIMENTA SET-UP

Four-point bending tests were carried out at the Materials and Structural Testing Laboratory of the University of Salerno, by means of a 3000 kN universal testing machine (ITALSIGMA IT2005-026 – frequency range up to 1.0 Hz – maximum displacement ± 75 mm) equipped with a load cell. The vertical load was applied on the simply supported beam by means of a steel frame, connected to the vertical jack of the testing machine as shown in Figure 4.6b. The steel frame permitted us to apply the two active loads at a distance equal to L/4 from the supports (L=1180 mm), as shown in Figure 4.6a.

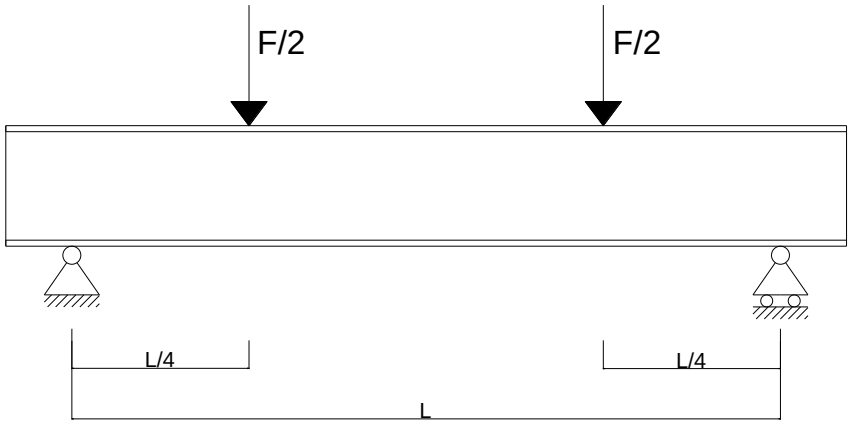

Figure 4.6a. Static scheme.

Figure 4.6b. Load condition.

Quasi-static tests were performed according to a displacement control modality at a constant rate of 5 μm/s (0.3 mm/min).
The mechanical response of each specimen was monitored by:

- ten uniaxial self-compensated strain gauges (SG), model "Vishay MM C2A-06-125LW-120";
- four Linear Variable Differential Transducers (LVDT), measuring range 0–50 mm, resolution 1 μm;
- two Laser Transducers (LT), measuring range 0–100 mm, resolution 1 μm.

In detail, the strain gauges SG were bonded at the mid-span cross-section: SG1, SG2 and SG3 were bonded on the top side of the upper flange, SG4,

SG5 and SG6 at the bottom side of the lower flange, while SG7 and SG9 as well as SG8 and SG10 were bonded on both sides of the web (Figure 4.7b).
The above-described instrumentation was introduced with the following purposes:

- six strain gauges (from SG1 to SG6) were utilized to evaluate the flexural curvature of the whole cross-section (global curvature);
- four strain gauges (from SG7 to SG10) were utilized to evaluate the flexural curvature of the web panel (local curvature);
- the four vertical LVDTs were utilized to evaluate the deflections of the beam at different positions over its length (Figure 4.7a);
- the two laser transducers were appointed on a transversal rigid bar mounted on the mid-span of the beam, in order to evaluate the torsional rotation of the cross-section (Figure 4.7c).

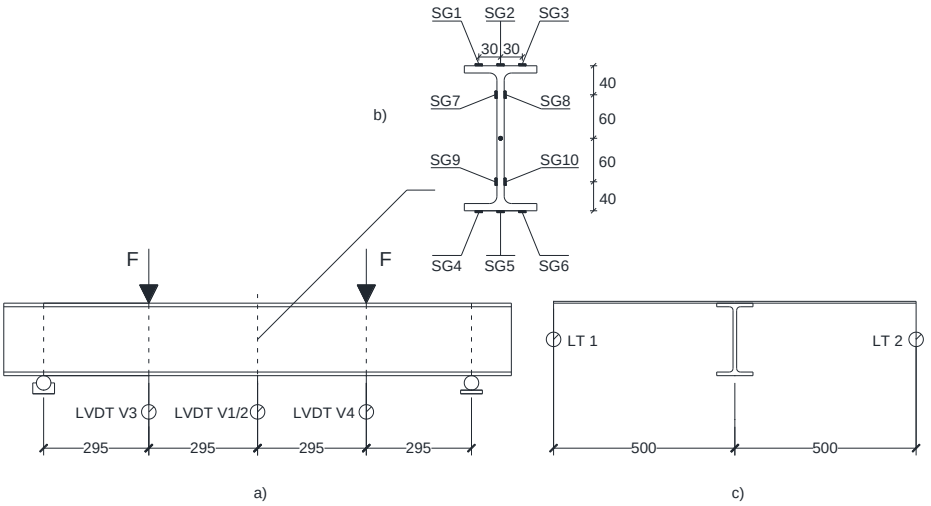

Figure 4.7. Instrumentation: a) LVDTs positioning; b) SGs positioning; c) LTs position and rigid arm.

In order to prevent stress concentrations and consequently undesirable local cracks, the following devices were placed at the location of both active and reactive forces:

- a neoprene pad (with thickness equal to 10 mm) in contact with the beam surface;
- a 100 mm × 100 mm × 10 mm steel plate, between the neoprene pads and the steel rounded surfaces of the testing device.

Moreover, appropriate stiffeners (made of three transverse steel plates grouped together) were placed at both sides of the web panel, as shown in Figure 4.6b.
The signals given by the load cell, LVDTs, LTs and SGs were recorded by an automatic data acquisition system (System 5100 Vishay MM) with a frequency equal to 10 data per second.

4.3 RESULTS AND DISCUSSION

In this section the experimental results of the ten point bending tests performed on Type 1 beams (four tests) and Type 2 beams (six tests) are reported.
The results were post-processed in view of evaluating the failure load, the Young's modulus, the bending curvature and the flexural mid-span deflection as discussed in the following.
In particular, Figure 4.8 shows the load vs mid-span flexural deflection curves reported for all tested specimens. The load P, lying on the vertical axis, is the sum of two vertical forces (F/2) as shown in Figure 4.7a; the deflection, *v*, plotted on the horizontal axis has been evaluated as the mean value of data returned by LVDT1 and LVDT2 (Figure 4.7a).

For a better understanding of Figure 4.7, a simplified notation has been adopted:

- the *i-th* Type 1 beam is indicated as "T1_*i*";
- the *i-th* Type 2 beam is indicated as "T2_*i*";

- the *i-th* Type 2 beam strengthened at the web–flange junction is indicated as "T2r_*i*".

In particular, Figure 4.8a refers to four Type 1 beam specimens, while Figures 4.8b and 4.8c refer to six Type 2 beam specimens respectively cured at 15°C (three specimens) and 28°C (further three specimens).
It is important to remark that the results obtained for beam T1_1 were discarded since local cracks that occurred over the test path compromised its global behaviour. The pultruded beam T1_1 was in fact tested without the interposition of the steel plate between the applied force and the neoprene pad (see Figure 4.9).

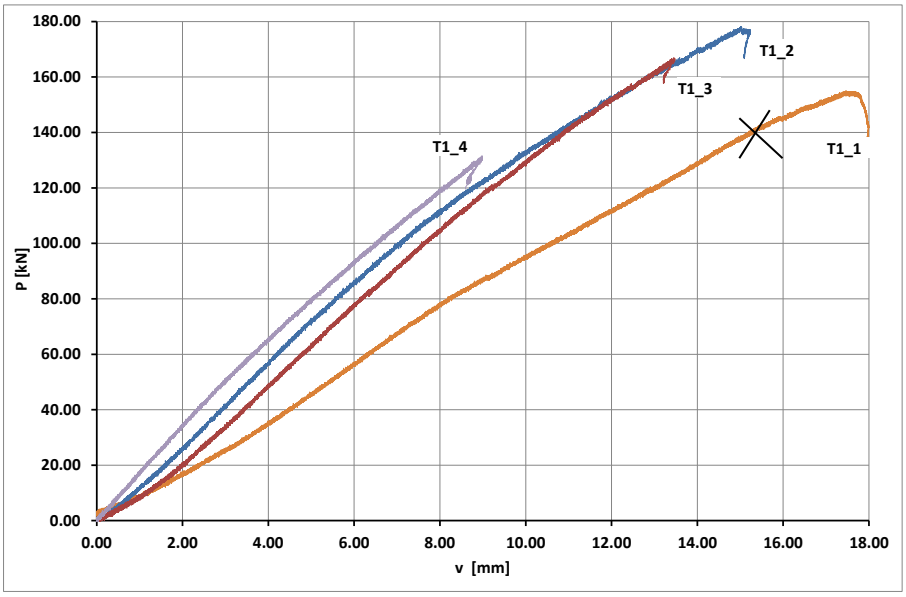

Figure 4.8a. Load vs mid-span flexural deflection curve (pultruded beams – T1_1, T1_2, T1_3, T1_4).

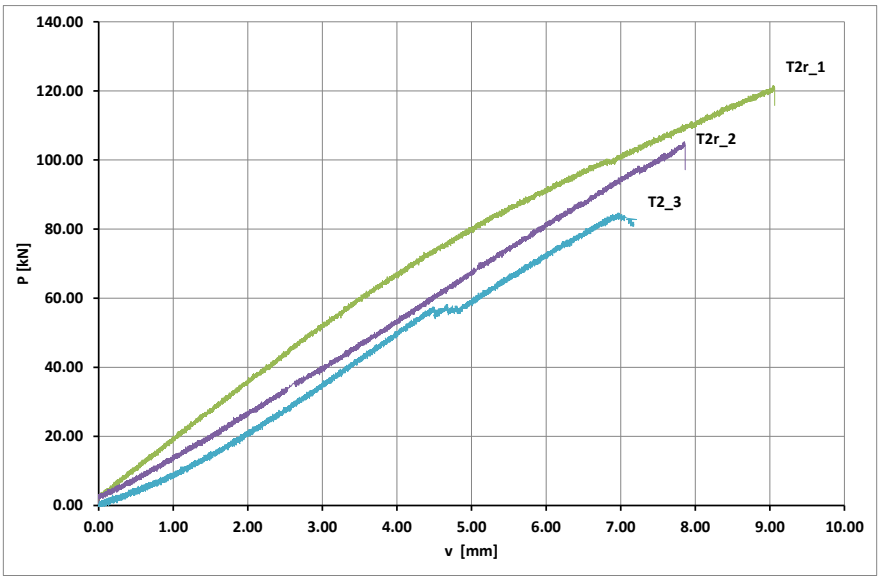

Figure 4.8b. Load vs mid-span flexural deflection curve (bonded beams with curing temperature 15°C - T2r_1, T2r_2, T2_3).

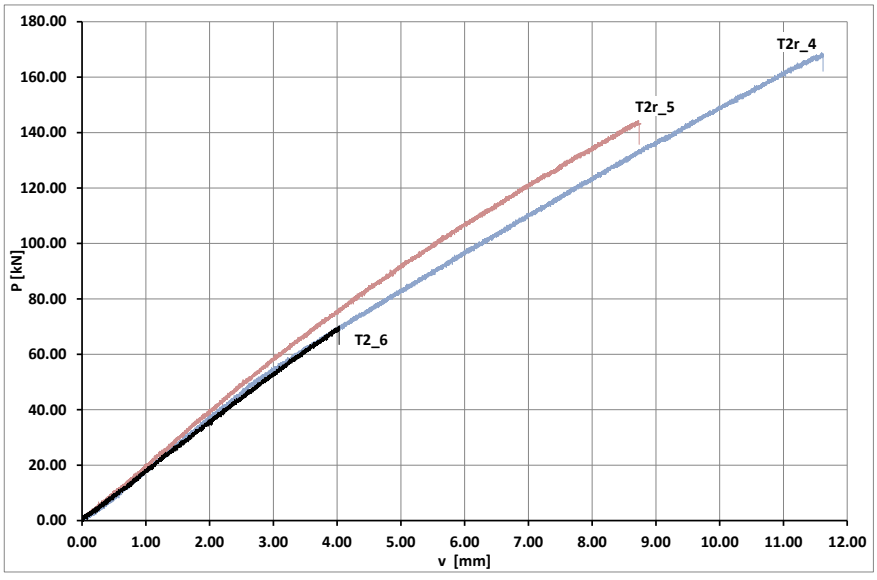

Figure 4.8c. Load vs mid-span flexural deflection curve (bonded beams with curing temperature 28°C - T2r_4, T2r_5, T2_6).

Figure 4.9. Local cracks in T1_1.

The results for all tests, in terms of failure load, P (measured in kN) and flexural mid-span deflection, v (measured in mm) are reported in Table 4.3. Moreover, the curing temperature adopted during the manufacturing of the bonded beams is indicated in the last column.

Table 4.3. Test results: Failure load and deflection at midspan.

# Beam	**Failure load, *P*** kN		**Deflection at midspan, *v*** mm	**Curing temperature** °C
T1_2	178	159 (mean value)	15.24	-
T1_3	167		13.86	-
T1_4	132		9.00	-
T2r _1	121	113 (mean value)	9.06	15
T2r _2	105		7.87	15
T2_3	85		7.80	15
T2r _4	169	157 (mean value)	11.63	28
T2r_5	144		8.77	28
T2_6	70		4.04	28

Table 4.4 presents the evaluation of the global flexural curvature, θ, the local flexural curvature of the web, θ_w, the Young's modulus, E, as well as the flexural mid-span deflection, v. Two different load levels were

considered: 50 kN and 100 kN. The curing temperature is indicated in the last column. Moreover, the strain profiles exhibited by Type 2 beams at mid-span cross-section are shown in Figures 10a and 10b for both the load levels cited above, respectively.

Table 4.4. Test results: bending curvature, Young's modulus, flexural mid-span deflection and curing temperature.

# Beam	Load level	Cross-section bending curvature, θ	Web panel bending curvature, θ_w	Young's modulus, E (UNI)	v	Curing temperature
	kN	$mm^{-1} \times 10^{-4}$	$mm^{-1} \times 10^{-4}$	MPa	mm	°C
T1_2	50	9.162	9.338	20986	3.535	-
	100	17.780	18.030		7.038	
T1_3	50	8.197	9.633	19405	4.090	-
	100	15.410	18.152		7.854	
T1_4	50	7.227	9.094	19885	2.914	-
	100	13.710	18.361		6.462	
T2r_1	50	7.888	8.079	18630	2.823	15
	100	16.001	16.660		6.795	
T2r_2	50	7.597	6.404	18254	3.734	15
	100	14.620	12.361		7.453	
T2_3	50	8.751	8.736	18072	3.976	15
T2r_4	50	8.652	7.892	19810	2.689	28
	100	17.280	15.790		6.216	
T2r_5	50	9.157	8.621	22411	2.512	28
	100	18.081	17.380		5.501	
T2_6	50	8.667	7.895	23724	2.817	28

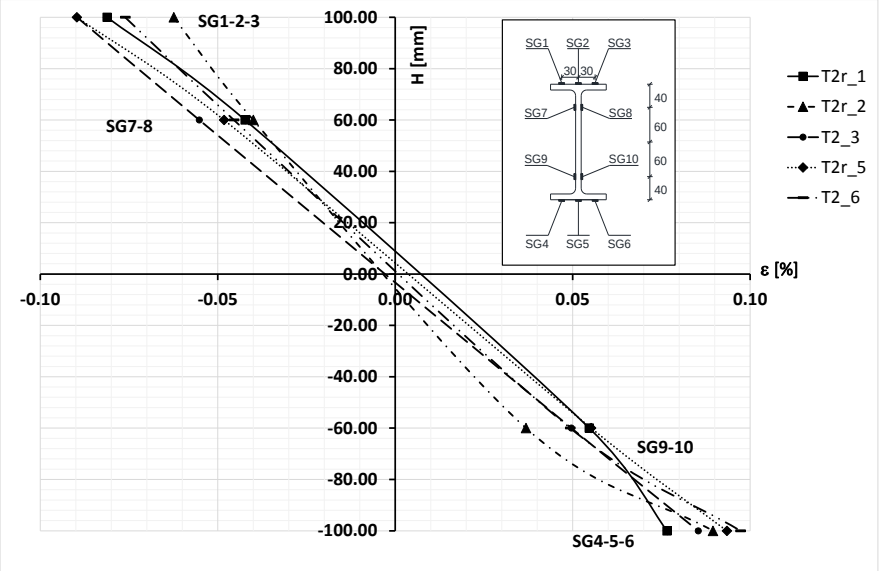

Figure 4.10a. Strain profile at mid-span cross-section for bonded beams for load level 50 kN.

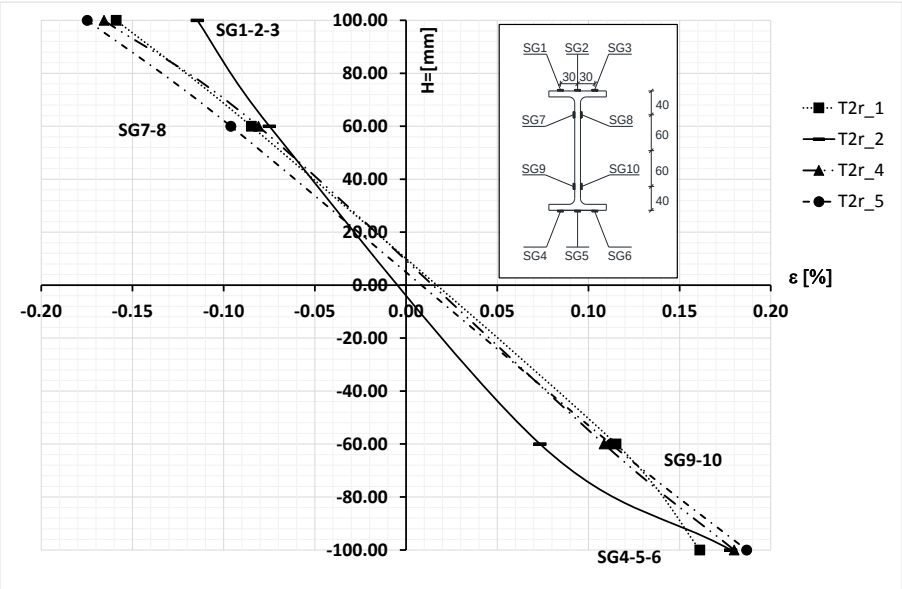

Figure 4.10b. Strain profile at mid-span cross-section for bonded beams for load level 100 kN.

The Young's modulus, *E*, was evaluated in accordance with the European Standard UNI EN 13706-2 indications, considering the following two experimental points of coordinates (v_1, P_1) and (v_2, P_2) with $v_1 = L/500 = 2.36mm$ and $v_2 = L/200 = 5.90mm$. The final formula is as follows:

$$E = \alpha \frac{L^3}{I} \frac{(P_2 - P_1)}{(v_2 - v_1)} \text{ with } \alpha \approx \frac{15}{384} \tag{4.1}$$

In eqn. 4.1, $P_1 = P_1(v_1)$ and $P_2 = P_2(v_2)$ are the loads corresponding to the flexural mid-span deflections v_1 and v_2, respectively; the symbol *I* denotes the second moment of area of the profile. Coefficient α refers to shear deformability according to the Timoshenko beam model and depends on the static scheme considered.
The results reported in Tables 4.3 and 4.4 and Figure 4.10 allow the following remarks:

- Type 1 beams (pultruded) show a substantially linear response up to failure, as expected; on the contrary, Type 2 beams (bonded) clearly show a non-linear behaviour, with constant loss of stiffness as the load increases.

- The mechanical response of the Type 2 beams is significantly influenced by the curing temperature of the bonding interfaces. With reference to the 100 kN load level, the Young's modulus increases from 18254 MPa (T2r_2) to 22411 MPa (T2r_5) and consequently the deflection decreases from 7.453 mm to 5.501 mm.

- The mechanical response of the Type 2 beams is significantly influenced by the web–flange reinforcement, especially in terms of failure load *P*. Specifically, the failure load decreases from 121 kN (T2r_1) to 85 kN (T2_3) for samples whose curing temperature was kept at 15°C, while it decreases from 169 kN (T2r_4) to 70 kN (T2_6) for samples whose curing temperature is set at 28°C.

- Type 2 beams exhibit an excellent performance compared with Type 1 beams in terms of flexural stiffness, while no relevant difference can be observed in terms of failure load.

- The strain profile exhibited by Type 2 beams can be considered almost linear, thus showing that the relative displacements between flange and web panels are negligible.

The good performance of the flexural response of Type 2 beams with respect to Type 1 beams is clearly dependent upon the mechanical properties of the specific adhesive used in the bonding process. In fact, the web–flange junctions are generally a weak zone in pultruded beams, due to the large amount of resin which is typically placed there during the pultrusion process. It is worth noting that mechanical properties of the inner polyester resins are less performing compared to the structural epoxy adhesive considered in this study (*SikaDur-30*).
Finally, in Figure 4.11 the load vs. mid-span flexural deflection curves are reported for all tests, comparing the experimental results with the numerical ones evaluated by eqn. 4.1. The Young's modulus *E* is reported in Table 4.4 while the second moment of area *I* varies according to the Type 1 and 2 cross-sections. The calculation of the flexural stiffness *EI* for all beams tested is reported in Table 4.5.

Table 4.5. Flexural stiffness evaluation.

# Beam	**Young's modulus, E (UNI)** MPa	**Second moment of area *I*** mm⁴	**Flexural stiffness EI** N.mm²
T1_2	20986	23′600′000	495′268′260′932
T1_3	19405	23′600′000	457′953′523′397
T1_4	19885	23′600′000	469′278′019′579
T2r_1	18630	23′973′454	446′628′863′414
T2r_2	18254	23′973′454	437′600′031′850
T2_3	18072	22′900′000	413′854′294′746
T2r_4	19810	23′973′454	474′914′760′286
T2r_5	22411	23′973′454	537′257′265′380
T2_6	23724	22′900′000	510′764′803′209

The second moment of area *I* for the beams strengthened by adding an adhesive curb at the web–flange junction (T2r_1, T2r_2, T2r_4 and T2r_5) was evaluated by scaling the adhesive curb contribution by means of ratio $\frac{E_{adhesive}}{E_{GFRP}} = n$ ($E_{adhesive} = 10400 MPa$).

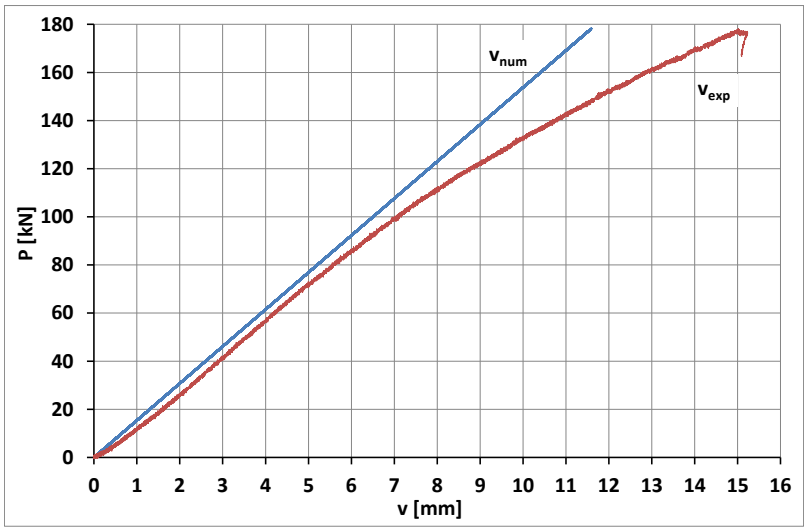
180
160
140
120
100
80
60
40
20
0
P [kN]
0 1 2 3 4 5 6 7 8 9 10 11 12 13 14 15 16
v [mm]
v_{num}
v_{exp}

a)

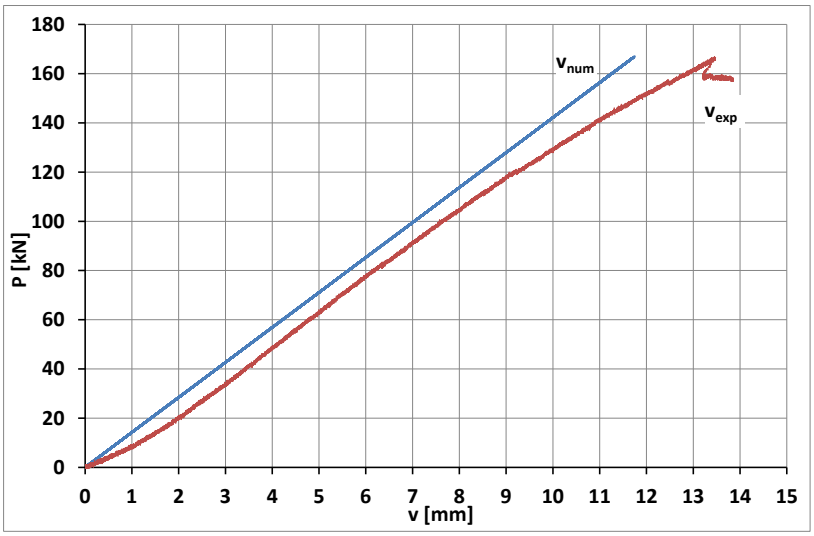
180
160
140
120
100
80
60
40
20
0
P [kN]
0 1 2 3 4 5 6 7 8 9 10 11 12 13 14 15
v [mm]
v_{num}
v_{exp}

b)

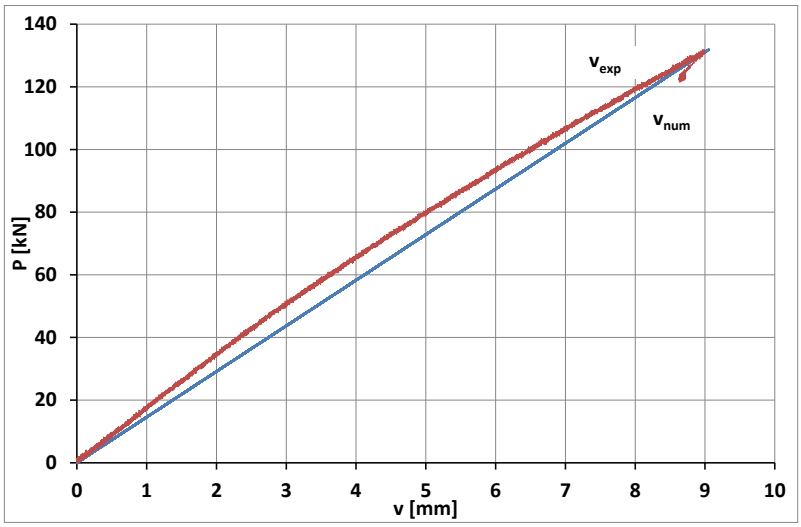

c)

Figure 4.11a. Load vs mid-span flexural deflection curve – comparison between experimental and analytical results: a) T1_2 beam; b) T1_3 beam; c) T1_4 beam.

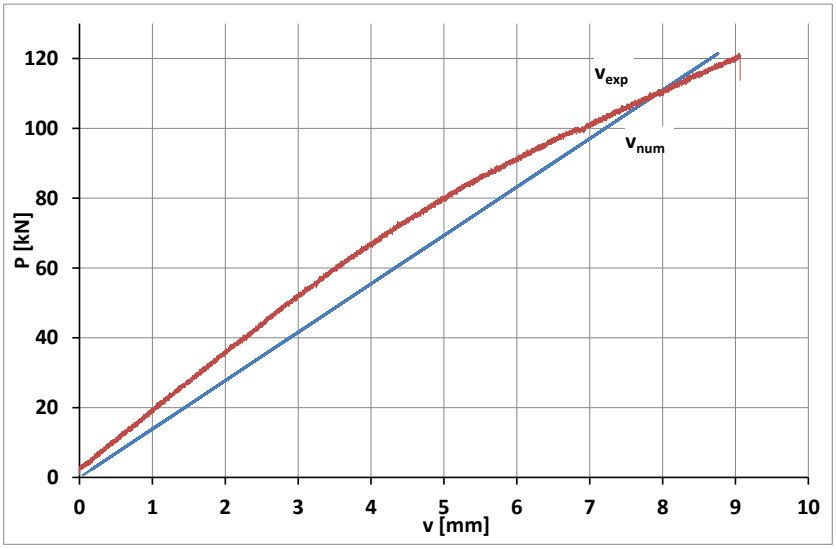

a)

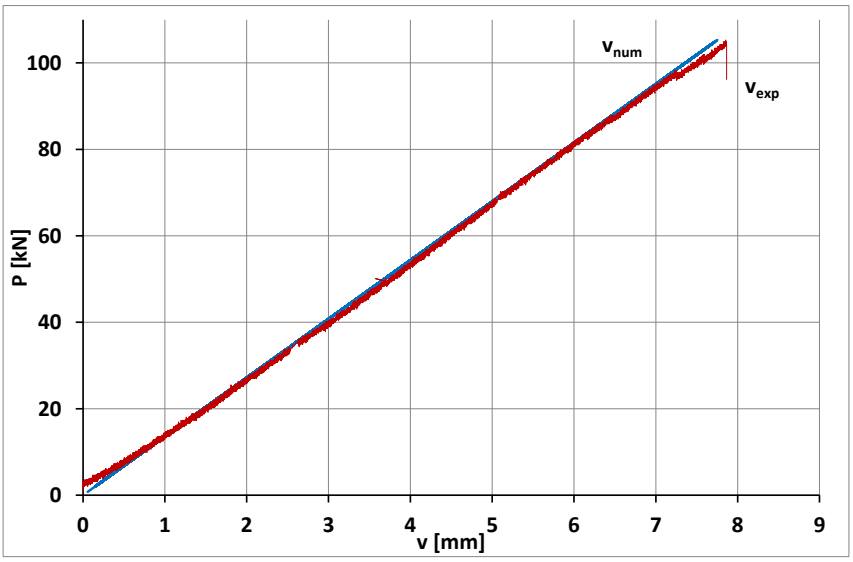

b)

Figure 4.11b. Load vs mid-span flexural deflection curve– comparison between experimental and analytical results: a) T2r_1 beam; b) T2r_2 beam.

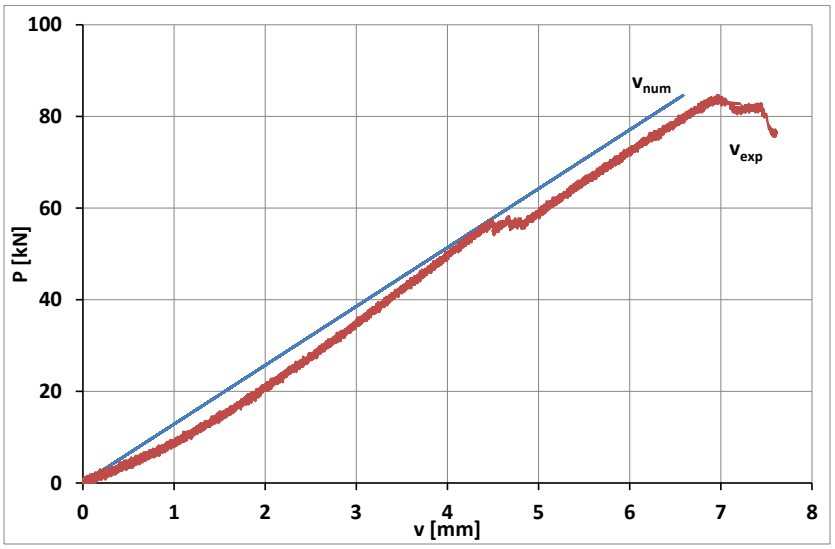

a)

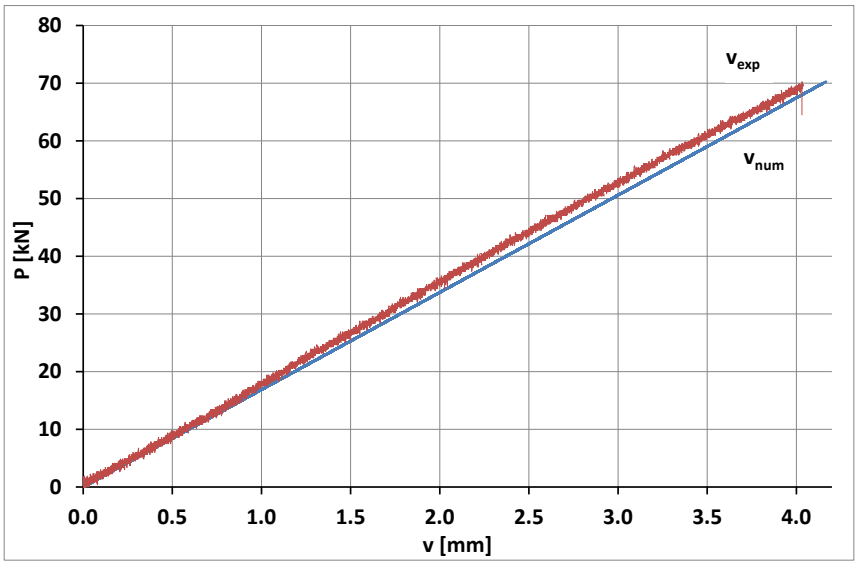

b)

Figure 4.11c. Load vs mid-span flexural deflection curve– comparison between experimental and analytical results: a) T2_3 beam; b) T2_6 beam.

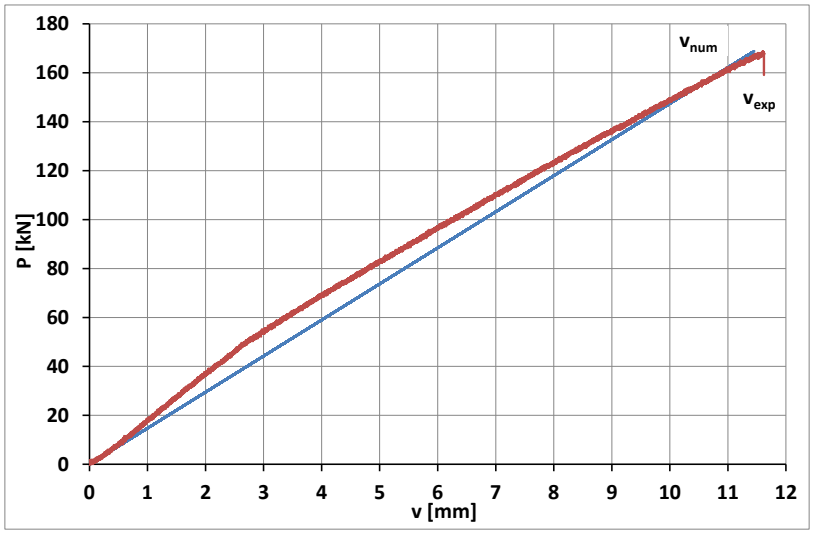

a)

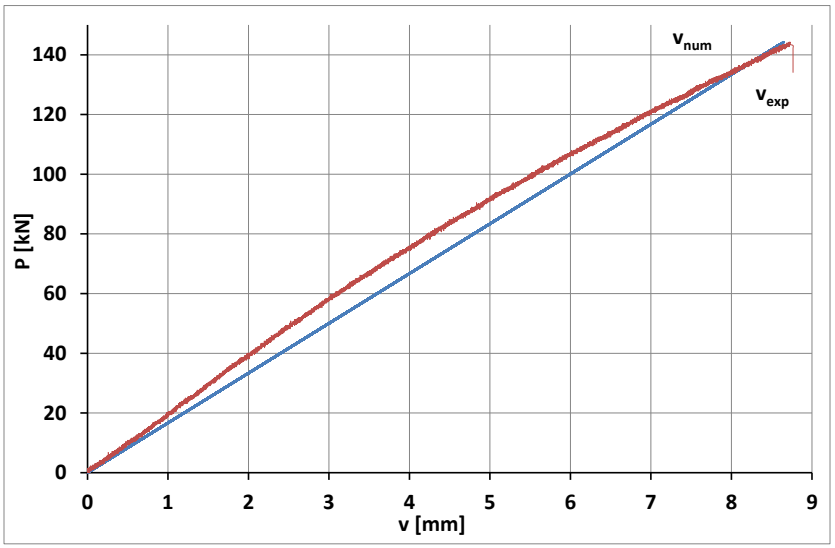

b)

Figure 4.11d. Load vs mid-span flexural deflection curve– comparison between experimental and analytical results: a) T2r_4 beam; b) T2r_5 beam.

The curves depicted in Figure 4.11 allow the following considerations:

- for all beams tested the analytical solution (linear elastic) allows us to evaluate correctly the experimental mid-span flexural deflections;
- for all Type 1 beams (pultruded) the analytical solution seems to underestimate mid-span flexural deflections, especially near the failure load;
- for all Type 2 beams (bonded) the analytical solution seems to slightly overestimate mid-span flexural deflections, especially for load levels equal to 50% of the failure load.

4.4 CONCLUSIONS

In this chapter an experimental campaign was developed in order to evaluate the flexural response of beams created by bonding simple GFRP panels together. The idea of studying this new paradigm of beams is focused on the possibility of achieving complex FRP shapes by means of low-cost designs inspired by modularity. The results obtained now permit us to answer the two questions posed in the introduction.

The first was "*what performance level can be achieved for bonded composite beams compared to similar pultruded ones?*".

Considering the experimental results obtained, it is possible to conclude that bonded beams are characterized by an equivalent failure load and by a stiffness higher than classical pultruded beams, especially at the serviceability limit state.

The second question was "*can the loss of stiffness, due to the bonding, affect the pre-failure response and the failure loads of bonded beams?*".

Differences in flexural mechanical behaviour were observed between the two types of bonded beams tested. The first configuration corresponds to a beam with no reinforcement at the web–flange connection and the second one to a beam strengthened at the same connection with a curb of epoxy resin. The reinforcement plays an important role in contrasting the torsional rotations between the web and flange because a decrease of mechanical response was observed for non-reinforced bonded beams. Furthermore, it is possible to conclude that the connection reinforcement is a better way to contrast the rotational effects than the rounded web–flange connection typical of the pultrusion process.

CHAPTER V

DIFFERENT SHAPES OF THE WEB/FLANGE REINFORCEMENT IN PULTRUDED "BONDED" BEAMS

5. INTRODUCTION

This Chapter presents a wide numerical investigation about the influence of an external reinforcement of the web/flange connection on the performance of bonded beams obtained by bonding simple panels to each other by means of epoxy resin.
Within this framework, two different models were developed: a 2D-model and a 3D-model. The 2D-model was used to understand the role played by the bonding joints in the experimental tests and to understand the influence of different types of reinforcements on the stress distribution in the adhesive layer. The 3D-model was implemented in order to study the influence of different web/flange reinforcements on the mechanical response of bonded beams (experimentally tested) in terms of failure load and flexural stiffness.
The numerical results have shown how it is possible to obtain, for these new bonded beams, levels of performance higher than those of the current pultruded beams, allowing us to consider the bonding system proposed as highly competitive in the field of construction of pultruded profiles.

5.1 2D MODEL: THE ROLE PLAYED BY THE WEB/FLANGE REINFORCEMENT IN BONDED BEAMS

One of the main results of the experimental investigation was the strong role played by the Web/Flange reinforcement with respect to the mechanical response of bonded beams [53]. In particular, in order to study the influence of such reinforcement on theflexural behavior of bonded beams, a wide numerical simulation was performed using the Abaqus FE Code.
In details, the analysis was organized into three steps:

- The first step was devoted to finding the best finite element model for the adhesive layer (connection between web and flanges).

- In the second step a qualitative comparison, in terms of stress distribution in the adhesive layer, between different types of reinforcement varying the geometry was performed.

- In the last step, a qualitative comparison in terms of stress distribution in the adhesive layer, between different types of material reinforcement, was performed. In particular, both the adhesive layer and external reinforcements were assumed to be made of different epoxy resins available on the market.

5.2 ADHESIVE LAYER MODELING – STEP 1

In order to find the best way to model the adhesive layer, 4 different possible models were developed (Figure 5.1a–d):

- *Model* 1: a contact cohesive constitutive law is implemented at the interface between the flange and the web;
- *Model* 2: 2D-cohesive elements with zero thickness are used, useful to model the crack propagation in glue material when it is very thin;
- *Model* 3: 2D-cohesive elements;
- *Model* 4: elastic 2D-elements bonded directly to the web and the flanges by means of a cohesive contact law.

In Models 3 and 4 the total thickness of the adhesive layer is equal to 2 mm, the same value adopted in the experimental campaign.

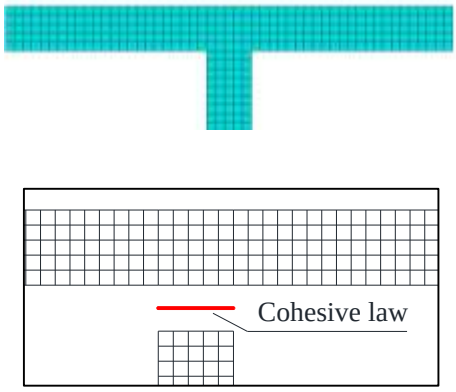

Figure 5.1a. *Model* 1

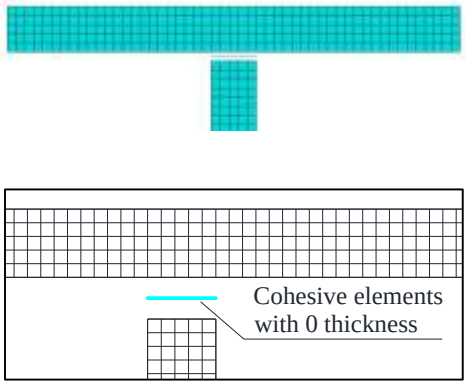

Figure 5.1b. *Model* 2

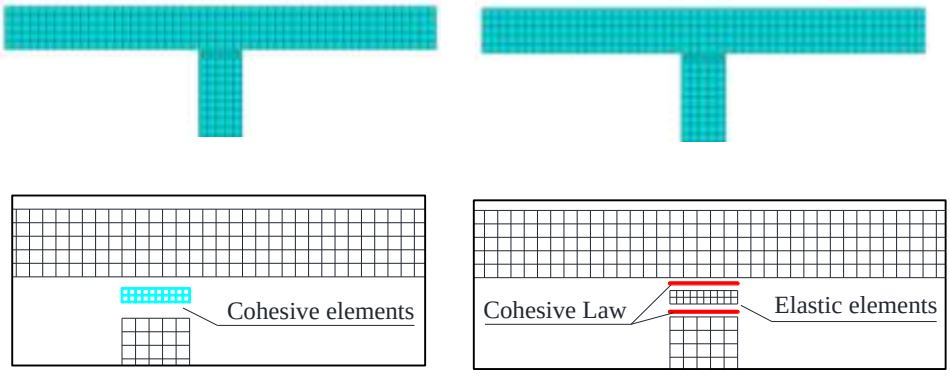

Figure 5.1c. *Model* 3 **Figure 5.1d.** *Model* 4

Figure 5.1. Four different models to describe the adhesive layer behaviour.

The four models introduced above are used to study the qualitative stress distribution along the adhesive layer for beam type 2 (bonded beams). The mechanical and geometrical properties were the same as those introduced in Table 4.2 of Chapter IV. An eccentric vertical displacement u_y, assumed equal to 3mm, is applied at the left end of the upper flange while the lower flange was fully fixed, as is shown in Figure 5.2.

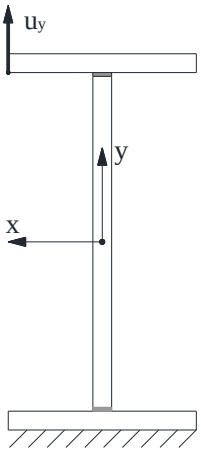

Figure 5.2. Static Scheme of the 2D model.

A CPS 4 - node bilinear - plane stress - quadrilateral element with length 2 mm was used for meshing the cross section of the beam while for meshing the adhesive layer the following meshes were adopted:

- for what concern *Model* 1 the adhesive layer was modeled by means of a cohesive law as depicted in Figure 5.3;

- for what concerns *Models* 2, 3 and 4 a mesh of twenty elements was adopted as described in details in Tables 5.1 and 5.2 and depicted in Figure 5.1. The reference parameter utilized in the convergence test was the stress σ_y along the *y* direction in the adhesive layer.

For what concerns the modelization aspects, more in details, in *Model* 1 the cohesive law representing the damage between the flange and the web was characterized by an elastic linear branch followed by a softing linear branch as depicted in Figure 5.3 relative to Mode I of fracture. By using symbols introduced in Figure 5.3, the quantity σ_I represents the interfacial tensile strength in the normal direction, the quantity K_I represents the elastic stiffness of the interface, the quantity δ_c the displacement at the end of the linear elastic branch while δ_I the displacement (separation) at failure. Finally, the quantity G_I represents the total energy dissipated equal to the area subtended by the curve. The values adopted for the parameters before introduced are summarized in Table 5.3.
Furthermore, relative to *Model* 2 a COH2D4 4-node-two-dimensional-cohesive element was used.
The damage is represented by the increment of the thickness of the cohesive elements starting from zero value by adopting a damage evolution and a limit traction value relative to the adhesive.

Relative to *Model* 3 the same elements as model 2 are used but they are characterized by a thickness. The damage is represented by the deformation of such elements considering the same traction limit value of the adhesive used in model 2 (Table 5.3).
Finally, in *Model* 4 the adhesive layer was modeled by CPS 4- node bilinear - plane stress - quadrilateral element as for the cross section, inserted into two cohesive laws of Figure 5.3.

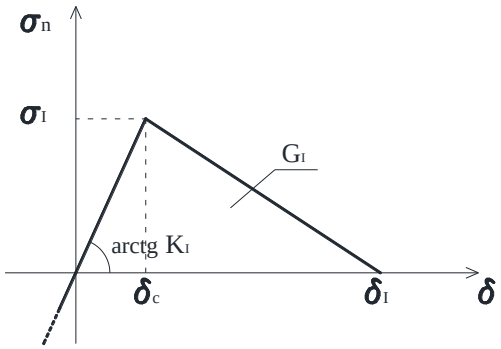

Figure 5.3. Bilinear constitutive law in Mode I.

Table 5.1. Mesh details relative to Models 2 and 3.

Mesh #	Upper Flange	Lower Flange	Web	Adhesive	σ_y [MPa]
1	250	250	440	5	21.9444
2	250	250	440	7	21.685
3	250	250	440	16	21.4675
4	250	250	440	20	21.4025
5	250	250	440	22	21.4009

Table 5.2. Mesh details relative to Model 4.

Mesh #	Upper Flange	Lower Flange	Web	Adhesive	σ_y [MPa]
1	250	250	440	5	20.7679
2	250	250	440	7	20.6863
3	250	250	440	16	20.6761
4	250	250	440	20	20.6699
5	250	250	440	22	20.6695

The results in term of stress σ_y along the *y* direction in the adhesive layer are depicted in Figures 5.4a and 5.4b for all adhesive models considered. It is important to remark that the stress distribution is evaluated with respect to both the nodes belonging to the flange (Figure 5.4a) and to the nodes belonging to the web (Figure 5.4b).

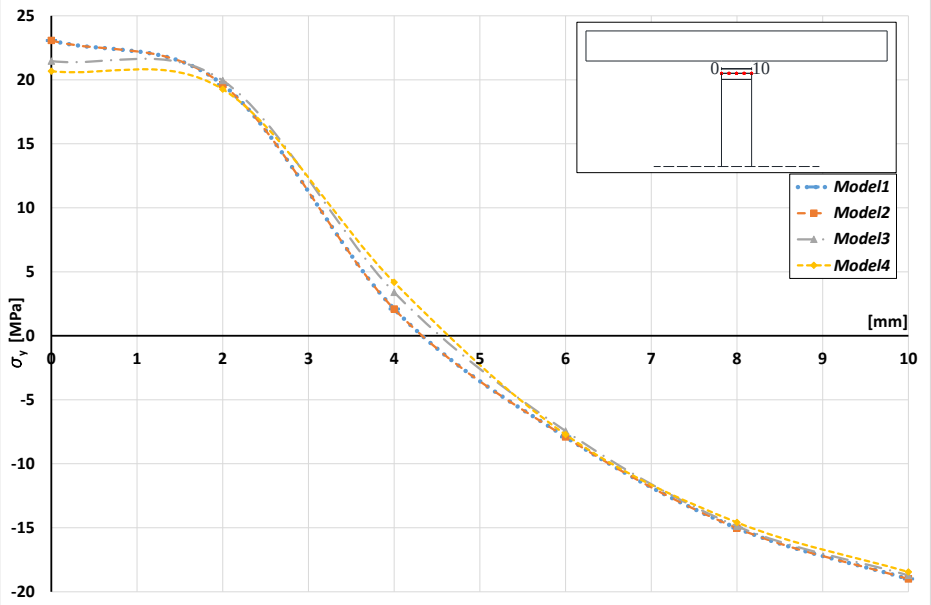

Figure 5.4a. σ_y stress distribution for the 4 models: nodes belonging to Flange.

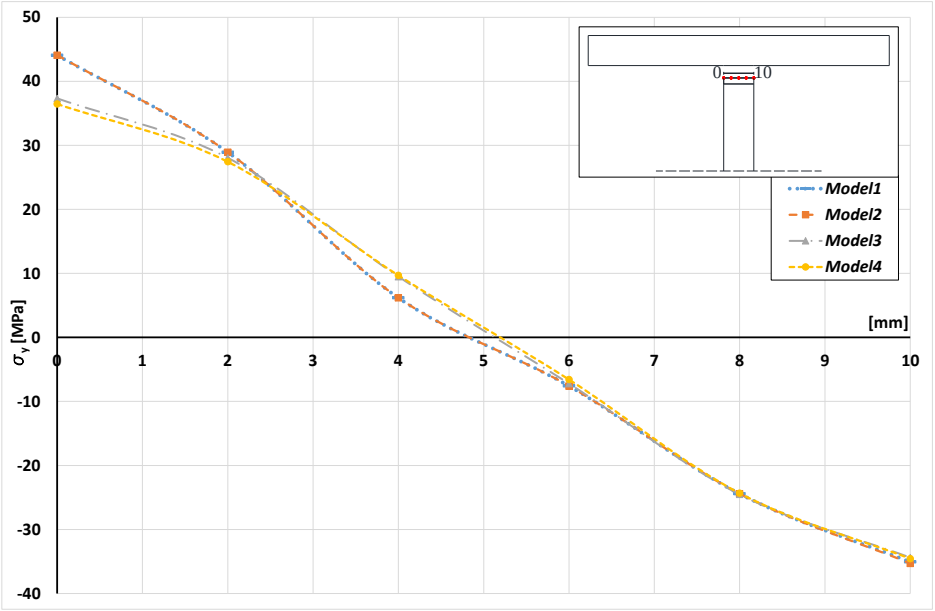

Figure 5.4b. σ_y stress distribution for the 4 models: nodes belonging to Web.

Except the left edge where the displacement is applied no substantial differences emerged between the 4 models introduced. In conclusion the authors have been adopted in the next the *Model* 1 for which the higher tensile stress was recorded.

5.3 WEB/FLANGE REINFORCEMENT SHAPES: STRESS DISTRIBUTION IN THE ADHESIVE LAYER – STEP 2

The aim of this section consists in analyzing numerically the qualitative stress distribution in the adhesive layer for both two types of bonded beams tested experimentally [54] (Type 2 and Type 2r of Section 2) in order to understand the role played by the reinforcements on the better mechanical response of the reinforced beam (Type 2r).
Subsequently, relative to reinforced bonded beams only (Type 2r), the influence of different reinforcement shapes on their flexural response is investigated.

It is important to remark that in the experimental campaign the external web/flange reinforcement was made by the same epoxy resin as that used for the adhesive layer. Then, the same assumption was made in the numerical analyses.

By adopting the 2D-model discussed in the previous section, a comparison between the behavior of Type 2 and Type 2r beams is performed. The geometrical and mechanical properties of these two beams are reported in Table 4.2 of Chapter IV. The static scheme was the same as Section 5.2: the value of the eccentric displacement u_y along the y axis, applied at the left end of the upper flange was equal to 3mm; the lower flange is fully fixed (Figure 5.2).

The results, in terms of the stress distribution σ_y in the adhesive layer for both beams (Type 2 and Type 2r) are depicted in Figure 5.5.

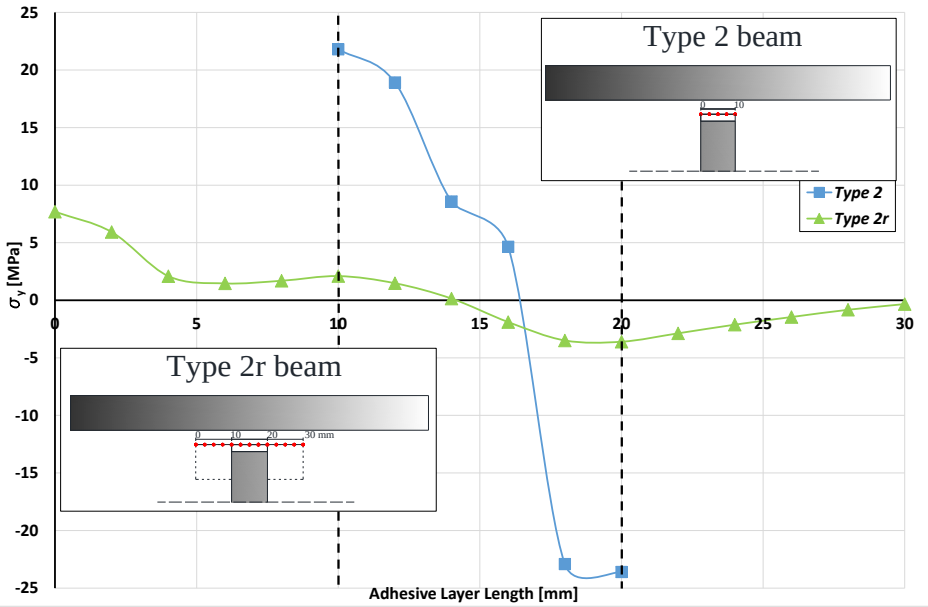

Figure 5.5. Comparison between Type 2 and Type 2r.

It is worth nothing that the presence of an adhesive square curb (Type 2r beam) leads to having a lower stress distribution than that of the Type 2 beam (i.e. absence of reinforcement) as experimentally evaluated (this means higher flexural rigidity of the beam). In particular, relative to Type 2r beam respect to Type 2 beam, the stress at the left edge of adhesive layer is three times smaller; the stress on the right edge of the adhesive layer is quite zero while the stress distribution along the entire adhesive layer assumes values between +8 and -4 MPa.

The numerical analysis previously described and discussed is now extended to several reinforcement shapes taking into account as material both the epoxy resin SikaDur30 and GFRP. In particular, several shapes were considered: square, rectangle, triangle and pluri-rectangle, as depicted in Figure 5.6. These reinforcements are bonded to the cross section by means of epoxy resin SikaDur30.

The results, in terms of the stress distribution σ_y along the horizontal contact line with upper flange are reported for all shapes reinforcement considered. In Figures 5.7–5.10, the reinforcement shapes with minimum and maximum dimensions are depicted. Relative to the reinforcement with rectangle shape the minimum dimension was considered only depending on the major increment of the second moment of area I_x respect to the maximum dimension. This last dimension has been considered in the 3D analysis as reported in the next.

Web/flange Reinforcement		
Geometry	***Dimension***	
	Minimum	***Maximum***
Square	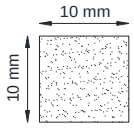	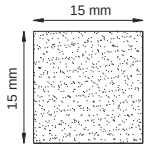
Triangle	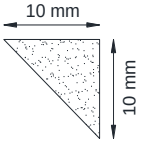	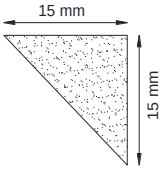
Rectangle	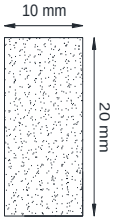	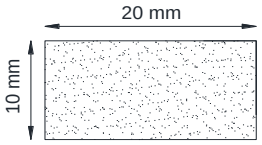
Pluris Rectangle	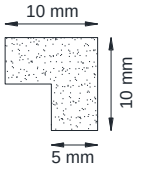	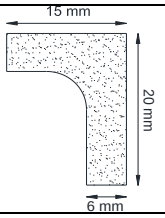

Figure 5.6. Web/Flange Reinforcement shapes.

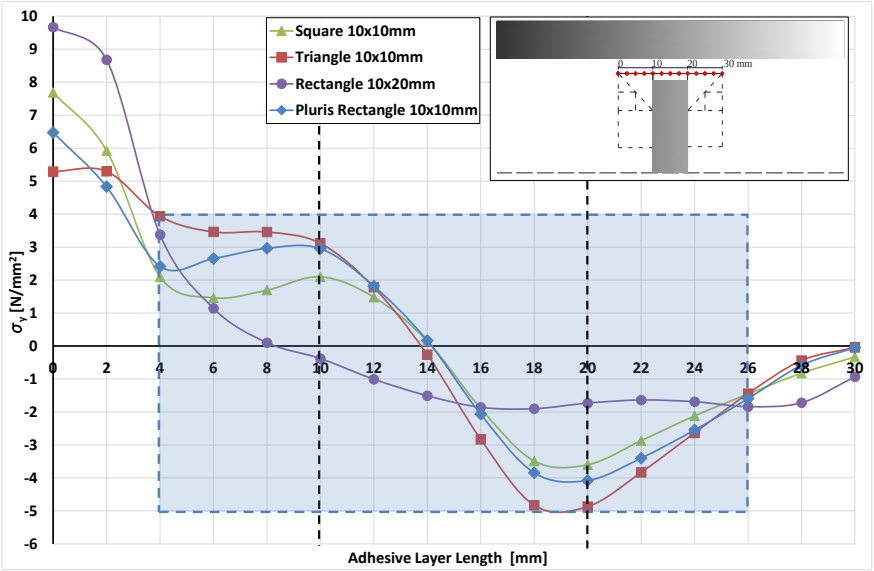

Figure 5.7. Stress distribution σ_y along the contact line between reinforcement and upper flange for different shapes reinforcement made of SikaDur30 (minimum values).

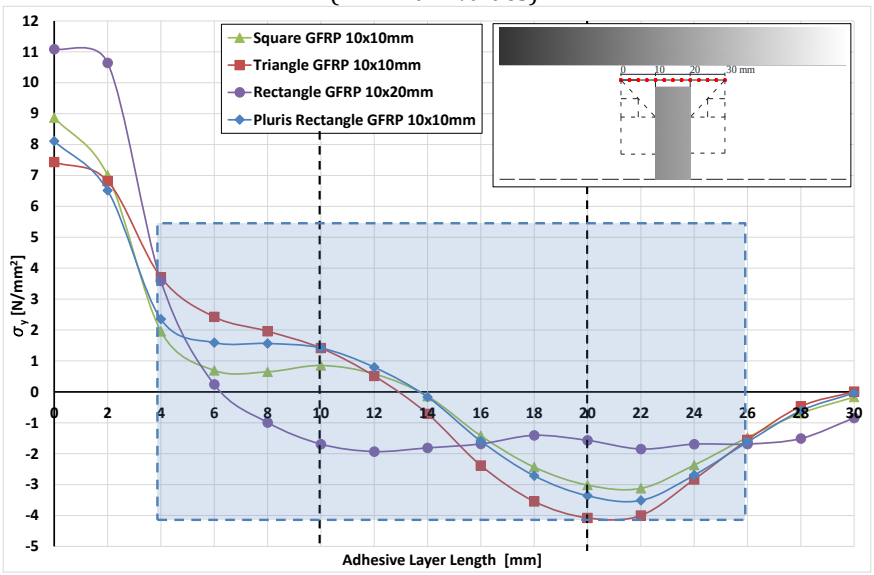

Figure 5.8. Stress distribution σ_y along the contact line between reinforcement and upper flange for different shapes reinforcement made of GFRP (minimum values).

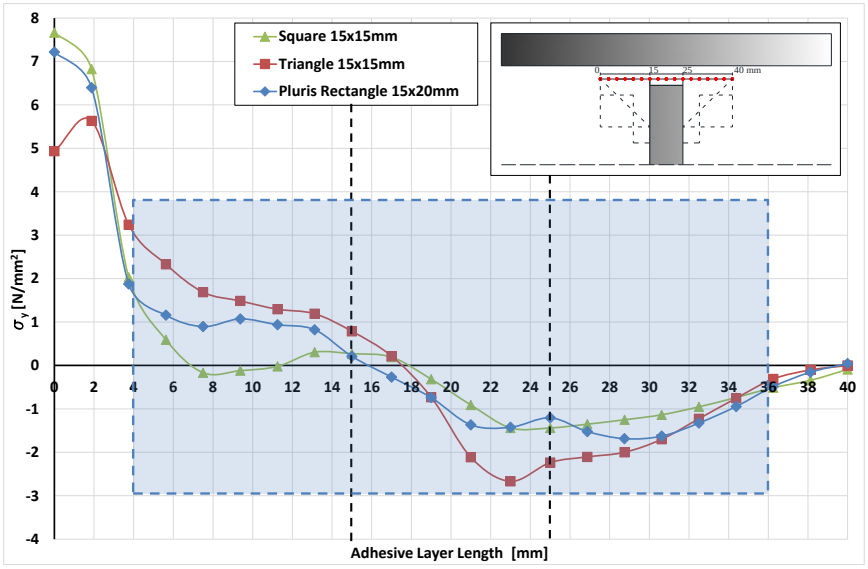

Figure 5.9. Stress distribution σ_y along the contact line between reinforcement and upper flange for different shapes reinforcement made of Sikadur30 (maximum values).

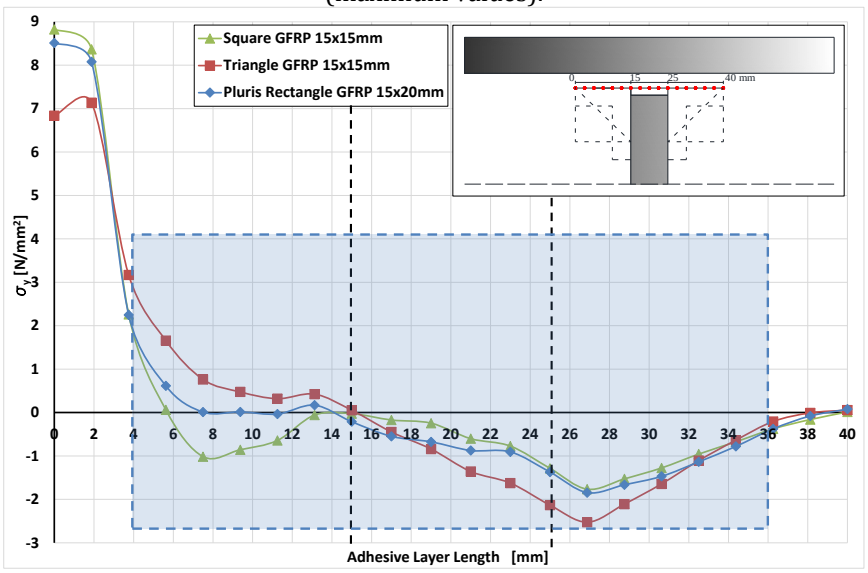

Figure 5.10. Stress distribution σ_y along the contact line between reinforcement and upper flange for different shapes reinforcement made of GFRP (maximum values).

The numerical results allow us to underline the following considerations:

1) For a fixed reinforcement shape, the σ_y stress distribution decreases if GFRP material is considered except of the left edge of the flange close to the point of application of the displacement. As a consequence the web/flange connection strength increases, so an improvement of the bonded beam mechanical response is obtained.

2) For a fixed reinforcement material, the σ_y stress distribution decreases if the second moment of area I_x is increased. This means that the best choice is a reinforcement with the maximum length along the web of the cross section.

5.4 WEB/FLANGE REINFORCEMENT MATERIALS: STRESS DISTRIBUTION IN THE ADHESIVE LAYER – STEP 3

In this section the numerical analysis conducted previously has been extended to the cases where the reinforcement and the adhesive layer were made of different epoxy resins. In particular SikaDur30, Adesilex Pg1 and Kemiepox are considered. The mechanical properties of the adhesives are reported in Table 5.3 where symbols are those introduced in Figure 5.3. Here the square shape for the reinforcement is only considered. Furthermore, the case in which the reinforcement is in GFRP and adhesive layer is made of different epoxy resins is also studied. The results in terms of σ_y stress distributions along the adhesive layer are reported in Figures 5.11–5.12.

Table 5.3. Mechanical properties of the adhesive provided by the producer**.**

SikaDur30		**unit**	**value**
Elastic Stiffness	K_I	N/mm	10400
Tensile strength	σ_I	MPa	31
Fracture Energy	G_I	KJ/m^2	3
Adesilex Pg1		**unit**	**value**
Elastic Stiffness	K_I	N/mm	6000
Tensile strength	σ_I	MPa	18
Fracture Energy	G_I	KJ/m^2	1
Kemiepox		**unit**	**value**
Elastic Stiffness	K_I	N/mm	3500
Tensile strength	σ_I	MPa	40
Fracture Energy	G_I	KJ/m^2	1

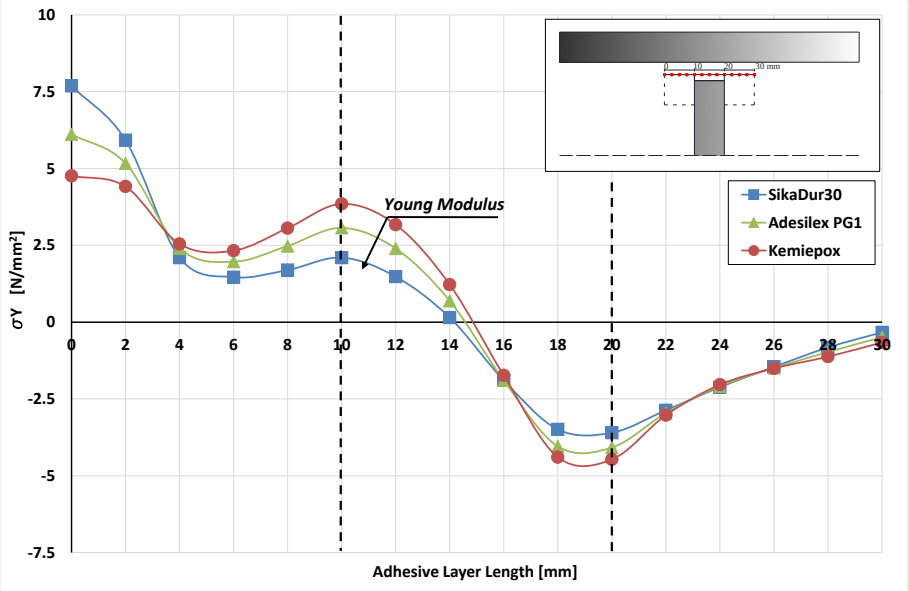

Figure 5.11. Stress distribution σ_y relative to square reinforcement made of different epoxy resins.

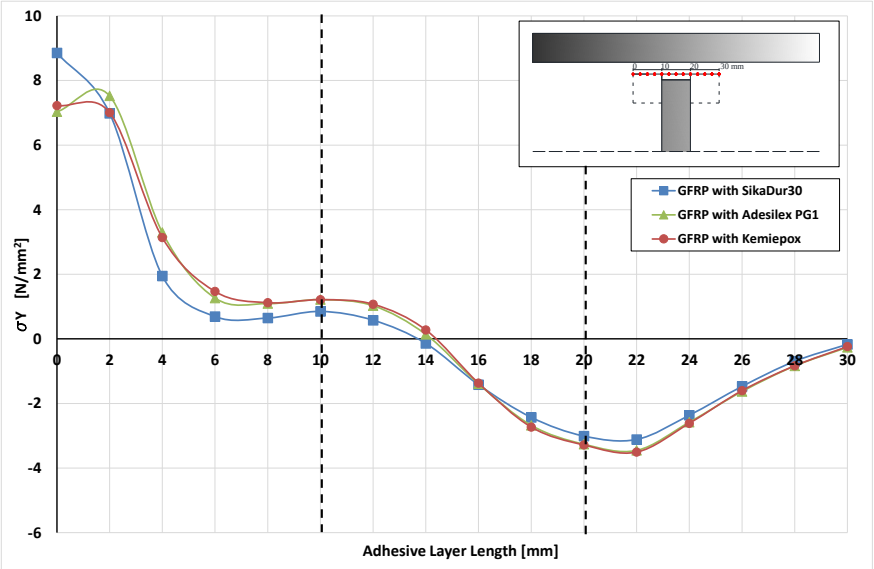

Figure 5.12. Stress distribution σ_y relative to square reinforcement made of GFRP and adhesive layers made of different epoxy resins.

The numerical results allow us to underline the following considerations:

1) The σ_y stress distribution decreases when reinforcement material is GFRP and not epoxy resin except of the left edge of adhesive layer near the point of the displacement applied;

2) Considering external reinforcement in GFRP, the σ_y stress distribution decreases when SikaDur30 epoxy resin is used to bond it to the cross section except for the left edge of the adhesive layer.

5.5 3D MODEL: THE INFLUENCE OF THE WEB/FLANGE REINFORCEMENT ON THE MECHANICAL RESPONSE OF BONDED BEAMS

In this section a 3D-model in the FE Abaqus Code is performed in order to study the influence of different web/flange reinforcements on the mechanical response of bonded beams in terms of failure load and flexural stiffness. In particular, all reinforcement shapes of the 2D analysis were considered.
In order to predict the failure load as well as the flexural displacements evaluated in the experimental campaign, the four-point bending test was simulated by adopting a 3D-model in Abaqus.
Thanks to the two axes of symmetry (x,y and y,z) depicted in Figure 5.13, only a quarter of beam is simulated, reducing computation time and memory.
The aforementioned symmetries were implemented by inhibiting the displacements, *u*, orthogonal to the symmetry planes as follows:

- relative to plane $\{x, y\}$ the displacements $u(x)$ and $u(z)$ assume zero value;
- relative to plane $\{y, z\}$ the displacement $u(x)$ assumes zero value.

C3D 8-node linear brick elements with a length equal to 2.5 mm are used for meshing the quarter of the beam (Figure 5.14). The mesh details are reported in Table 5.4.

Table 5.4. 3D-model mesh detail (beam).

	Number of finite elements		
Model	**Upper Flange**	**Lower Flange**	**Web**
1	22400	22400	20834

Furthermore, the mesh adopted for any type of reinforcement considered is reported in Table 5.5.

Table 5.5. 3D-model mesh detail (reinforcement).

Reinforcement	**Number of finite elements**
Square 10x10	4480
Square 15x15	10080
Rectangle 10x20	8960
Rectangle 20x10	8960
Triangle 10x10	2240
Triangle 15x15	5040
Pluris Rectangle 10x10	3360
Pluris Rectangle 15x20	11828

To simulate the adhesive layer the cohesive law introduced in Section 5.2 was used.
The damage occurs only in the adhesive layer and its evolution is governed by energy in Mode I (G_I) dissipated.
Finally, due to the symmetry a quarter of the active vertical force is applied on the quarter of beam.

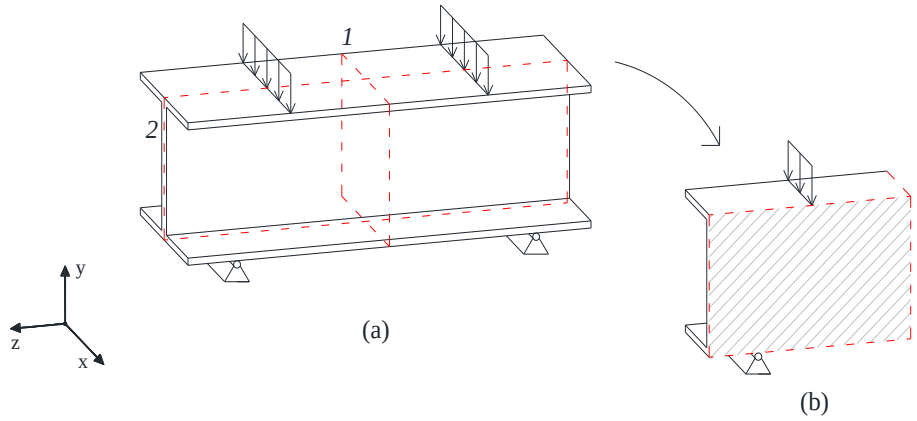

Figure 5.13. Symmetry planes.

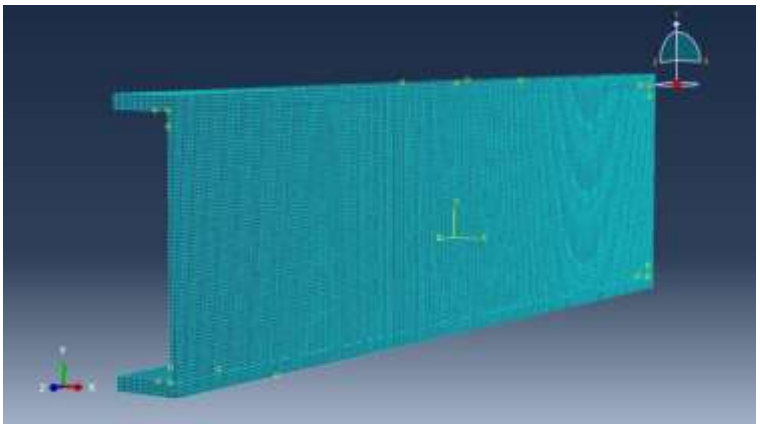

Figure 5.14. 3D view mesh – Abaqus FEM model.

Considering the symmetries conditions before introduced the external force, F_m, applied in *y* direction on the model (Figure 5.13), correspond to a total force *F*, acting on the structure ($F = 4F_m$).

In order to verify the accuracy of the present model, a comparison with the experimental results is performed. In particular, numerical results were compared to experimental ones [53] relative to the four-point bending test of Type 2 beam (T2_6 test) and Type 2r beam (T2r_5 test) as depicted in Figures 5.15–5.16, respectively. It is important to underline that the experimental results considered are relative to beams with a curing temperature equal to 28 °C.

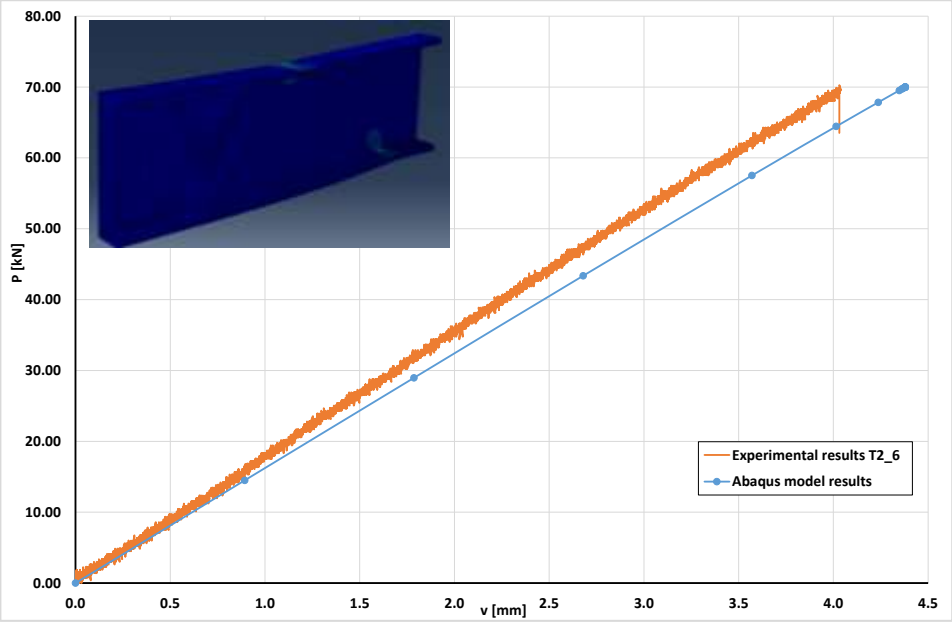

Figure 5.15. Comparison between results of T2_6 beam and FE model.

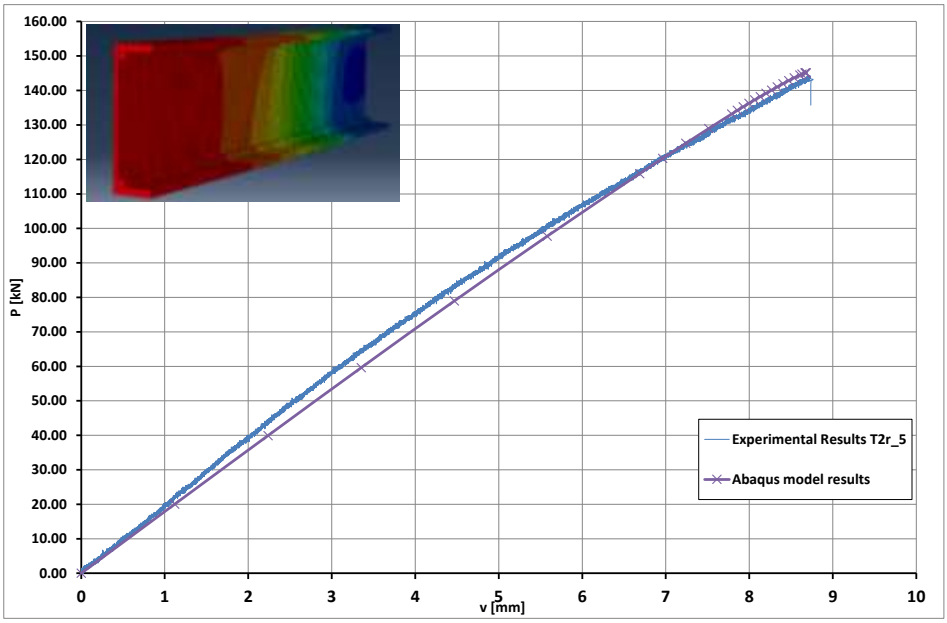

Figure 5.16. Comparison between results of T2r_5 beams and FE model.

As it is possible to verify from the load-displacements graphs, the numerical results are in good agreement with experimental data for what concern the reinforced beams highlighting the non-linear behavior and the loss of stiffness when the load increases as experimentally shown.

The numerical evaluation of the load peak value is obtained when the total fracture energy G_I is dissipated (equal to the area subtended by the curve in Figure 5.3).

In particular, with respect to bonded beams without reinforcement (Figure 5.16), the predictive analysis is in good agreement with experimental results for what concerns failure load; and it is less conservative with respect to the deformability. Furthermore, with respect to bonded beams with reinforcement, the predictive analysis is in perfect agreement with the T2r_5 beam experimental results both in terms of failure load and deformability.

5.6 PREDICTIVE ANALYSIS

Based on 3D-model presented in the previous section a numerical analysis is developed in order to predict the failure load and flexural strains relative to bonded beams varying the geometry and mechanical properties of the Web/Flange reinforcement.
In particular, the reinforcement was made of both SikaDur30 epoxy resin and GFRP.
The numerical results are presented in Figures 5.17–5.20 where load-vertical displacement curves are depicted.
The results in terms of failure loads and vertical flexural displacement are also summarized in Table 5.6. In particular, the second moment of area *I* for each bonded beams is evaluated by scaling the adhesive reinforcement (when made of epoxy resin) by means of ratio $E_{adhesive}/E_{GFRP}=n$ ($E_{adhesive}=10400MPa$).
Furthermore, the Young's Modulus, *E*, was evaluated in accordance with the European Standard UNI EN 13706-2 indications, considering the following two experimental points of coordinates (v_1,P_1) and (v_2,P_2) with $v_1=L/500=2.36mm$ and $v_2=L/200=5.90mm$. The final formula is:

$$E=\alpha\frac{L^3}{I}\frac{(P_2-P_1)}{(v_2-v_1)} \text{ with } \alpha\approx\frac{15}{384} \tag{5.1}$$

In Equation (5.1), $P_1=P_1(v_1)$ and $P_2=P_2(v_2)$ are the loads corresponding to the flexural mid-span deflections v_1 and v_2, respectively; the symbol *I* denotes the second moment of area of the profile. Coefficient α accounts for shear deformability according to the Timoshenko beam model and depends on the static scheme considered.

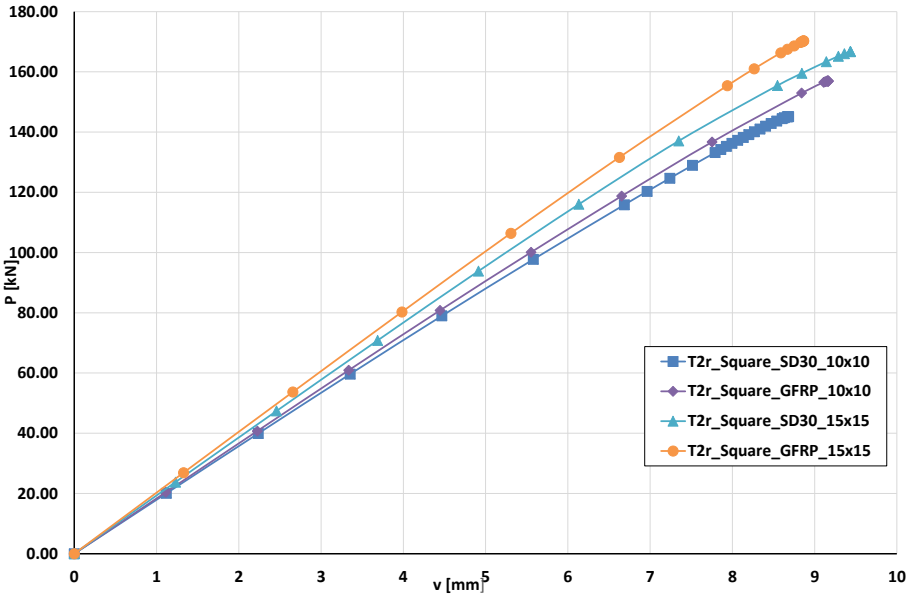

Figure 5.17. Load vs. mid-span flexural deflection curve – (square reinforcement).

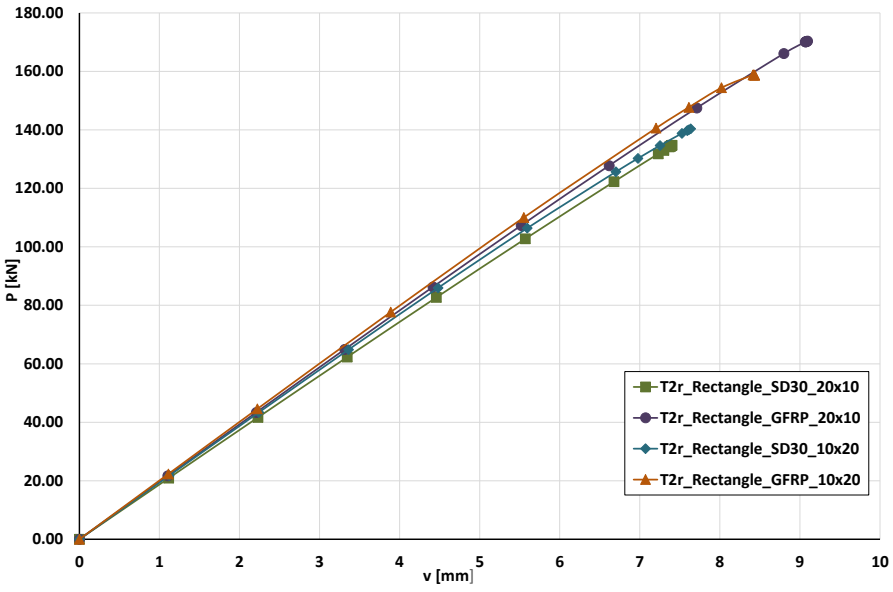

Figure 5.18. Load vs. mid-span flexural deflection curve – (rectangle reinforcement).

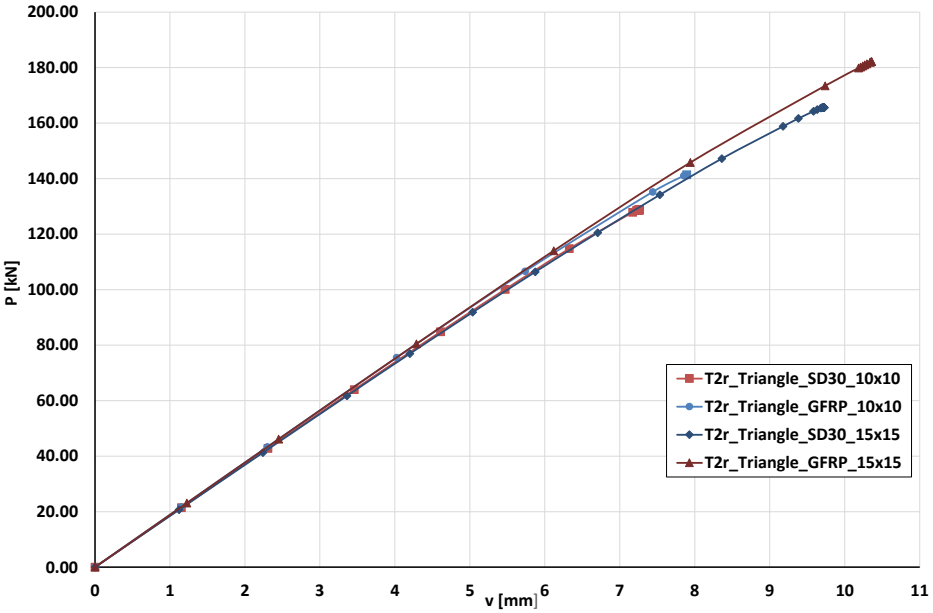

Figure 5.19. Load vs. mid-span flexural deflection curve – (triangle reinforcement).

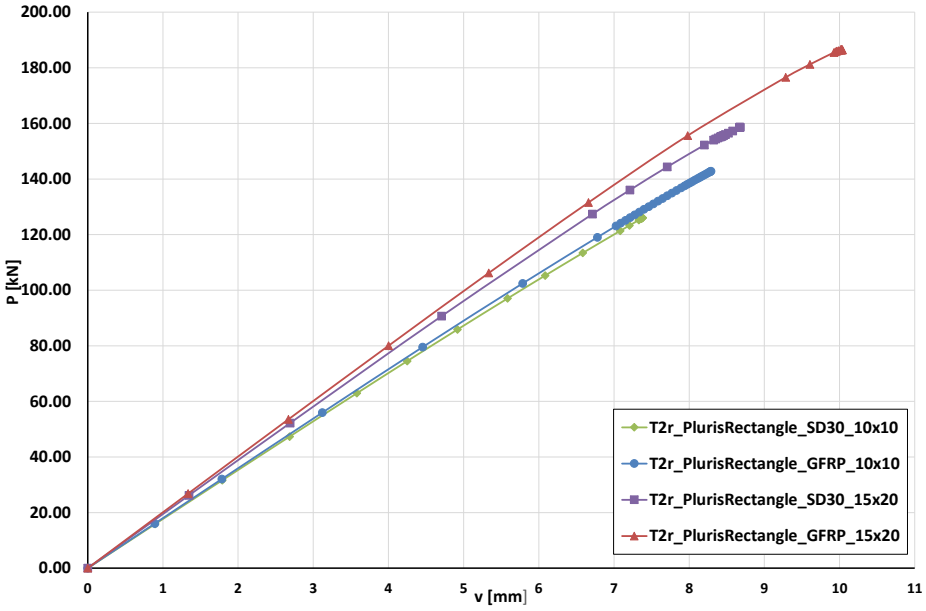

Figure 5.210. Load vs. mid-span flexural deflection curve – (pluris rectangle reinforcement).

Table 5.5. Flexural stiffness and failure load.

Beam							
Type	***Area***	***Material***	***E***	***I***	***EI***	P_{max}	***v***
	[mm²]		**[Mpa]**	**[mm⁴]**	**[Nm²]**	**[kN]**	**[mm]**
Square	100.0	SikaDur30	23'232	23'974'667	556'977	145.11	8.69
		GFRP	22'279	25'793'333	574'640	156.88	9.16
	225.0	SikaDur30	23'893	25'181'500	601'660	166.75	9.44
		GFRP	22'057	29'042'500	640'596	170.31	8.86
Rectangle	200.0	SikaDur30	23'528	25'049'333	589'359	134.73	7.40
		GFRP	21'700	28'686'667	622'488	170.40	9.11
	200.0	SikaDur30	24'401	24'811'619	605'437	140.52	7.68
		GFRP	22'587	28'046'667	633'503	158.83	8.44
Triangle	50.0	SikaDur30	24'867	23'458'381	583'333	128.68	7.26
		GFRP	24'292	24'403'333	592'801	141.29	7.89
	112.5	SikaDur30	23'959	24'109'696	577'647	165.66	9.73
		GFRP	22'791	26'156'875	596'152	182.17	10.36
Pluris Rectangle	75.0	SikaDur30	23'276	23'721'786	552'143	126.09	7.38
		GFRP	22'378	25'112'500	561'960	142.80	8.29
	174.0	SikaDur30	24'473	24'774'270	614'570	158.58	8.67
		GFRP	22'780	27'946'112	636'608	186.44	10.04

The results summarized in Table 5.5 allow us to make the following conclusions:

1) The 3D numerical analyses confirm the 2D numerical results. In fact, for a fixed reinforcement geometry, the GFRP material gives a better mechanical response, in terms of failure load and flexural stiffness, than epoxy resin material.

2) The maximum value of the flexural stiffness was obtained for the square and pluris rectangle reinforcements in GFRP (more or less 640000 Nm^2 with respect to the mean value of 500000 Nm^2 obtained experimentally).

3) The maximum value of the failure load was obtained for the square and pluris rectangle reinforcements in GFRP: 170 kN was obtained in case of square reinforcement and 186 kN in case of pluris rectangle reinforcement respect to the mean value of 157 kN obtained experimentally.

The choice of the best reinforcement, in general, depends on the cost and manpower also. In fact, the square reinforcement presents more material than the pluris rectangle reinforcement (200mm^2 against 175mm^2) but the surface to bond is less for the square than for the pluris rectangle (30mm against 35mm). The greater the surface to be bonded, the greater will be the risk of imperfections.

5.7 CONCLUSIONS

In the Chapter V a wide numerical investigation has been developed in order to evaluate the mechanical response of bonded beams (obtained by bonding simple pultruded panels each other) when a reinforcement at the web-flange junction was considered. Within this framework, the Abaqus FEA code was used.

In particular, the numerical investigation consisted of two different models: a 2D model and a 3D model.

The 2D-model was used to study the stress distribution in the adhesive layer when different types (varying the geometry) of reinforcement were used.

The 3D-model was implemented in order to study the influence of such different reinforcements on the mechanical response of bonded beams in terms of failure load and flexural stiffness making a comparison with the experimental results.

The numerical results have shown how it is possible to obtain, for these new bonded beams, levels of performance higher than those of the current pultruded beams. In detail, increments of 20% and 12% were reached with respect to failure load and flexural stiffness, respectively.

APPENDIX A

In this Appendix A the further numerical results about the cantilever beam as well as the results about the simply supported beam static scheme are reported schematically.

Cantilever beam

In Table A1 the results in terms of buckling loads and different GFRP cross section geometries relative to cases B1, C1,C2 and C3 are reported. These results can be appreciated more by reference to the detailed discussion presented within the body of the Chapter 3.

Table A1. Cantilever beam : cross sections and pertinent buckling loads.

Case studied		Cross sections *dimension in mm*	Load^{crit}	$\frac{L^{crit}_{GFRPi}}{L^{crit}_{GFRP}}$	$\frac{V_{GFRPi}}{V_{GFRP}}$	η
		(H x B x s_1 x s_2)	**q^{crit} [N/mm]**	**[-]**	**[-]**	**[-]**
B1 (I-)	Steel	(200 x 100 x 8.5 x 5.6)	18.00	-	-	-
	GFRP	(200 x 100 x 8.5 x 5.6)	1.50	1.00	1.00	1.00
	GFRP*1*	(200 x 100 x 17 x 11.2)	5.50	3.66	1.93	1.90
	GFRP*2*	(400 x 100 x 8.5 x 5.6)	1.40	0.93	1.41	0.66
	GFRP*3*	(200 x 100 x 25.5 x 16.8)	12.00	8.00	2.79	2.87
	GFRP*4*	(200 x 200 x 8.5 x 5.6)	5.50	3.66	1.62	2.25
	GFRP*5*	(200 x 200 x 17 x 11.2)	16.00	10.66	3.18	3.35
		(H x B x s)	**N^{crit} [kN]**	**[-]**	**[-]**	**[-]**
C1 (L-)	Steel	(100 x 100 x 10)	12.00	-	-	-
	GFRP	(100 x 100 x 10)	1.00	1.00	1.00	1.00
	GFRP*1*	(100 x 100 x 20)	4.00	4.00	2.00	2.00
	GFRP*2*	(200 x 200 x 10)	0.80	0.80	2.00	0.40
	GFRP*3*	(proposed new shape, see Figure B3)	9.00	9.00	1.71	5.27
		(H x B x s)	**N^{crit} [kN]**	**[-]**	**[-]**	**[-]**
C2 (T-)	Steel	(80 x 80 x 9)	20.00	-	-	-
	GFRP	(80 x 80 x 9)	2.15	1.00	1.00	1.00
	GFRP*1*	(80 x 160 x 9)	6.50	3.02	1.53	1.97
	GFRP*2*	(80 x 80 x 18)	4.00	1.86	1.88	0.99
	GFRP*3*	(160 x 80 x 9)	2.15	1.00	1.53	0.65
	GFRP*4*	(80 x 160 x 18)	14.00	6.51	2.94	2.21

follow…

continue…

Case studied		**Cross sections** *dimension in mm*	**Load^{crit}**	$\frac{L^{crit}_{GFRPi}}{L^{crit}_{GFRP}}$	$\frac{V_{GFRPi}}{V_{GFRP}}$	η
		(H x B x s_1 x s_2)	**N^{crit} [kN]**	**[-]**	**[-]**	**[-]**
C3 (I-)	Steel	(200 x 100 x 8.5 x 5.6)	70.00	-	-	-
	GFRP	(200 x 100 x 8.5 x 5.6)	8.00	1.00	1.00	1.00
	GFRP*1*	(200 x 200 x 8.5 x 5.6)	58.00	7.25	1.62	4.46
	GFRP*2*	(200 x 100 x 17 x 11.2)	15.00	1.87	1.93	0.97
	GFRP*3*	(400 x 100 x 8.5 x 5.6)	7.00	0.88	1.41	0.62
	GFRP*4*	(200 x 150 x 12.75 x 8.4)	42.00	5.25	1.94	2.70

CASE B1

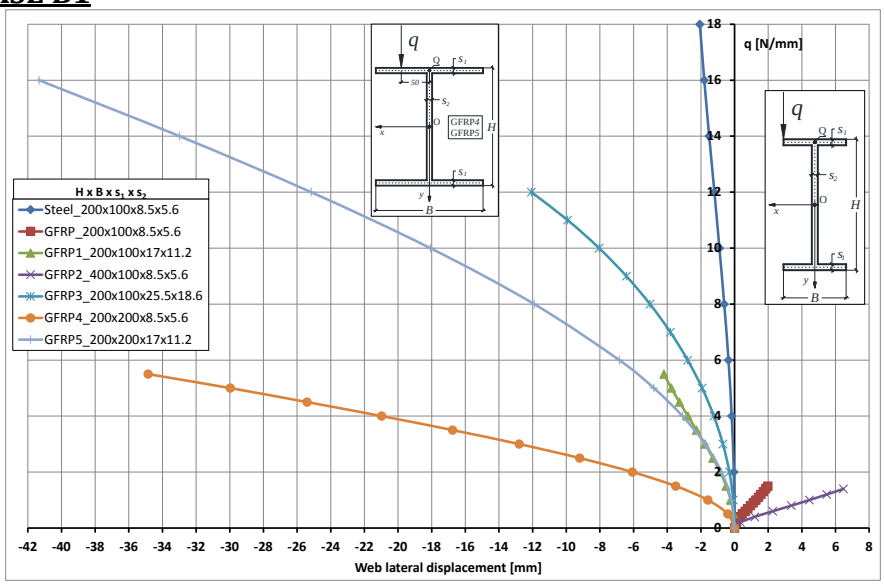

Figure A1a. Case B1 - Load q versus lateral displacements u of point O on the web.

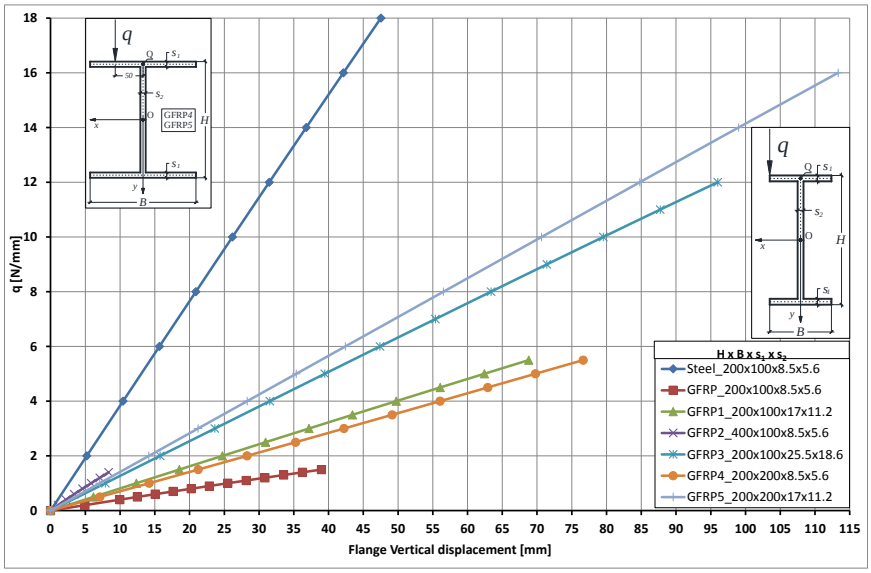

Figure A1b. Case B1 - Load q versus vertical displacements v of point Q on the flange.

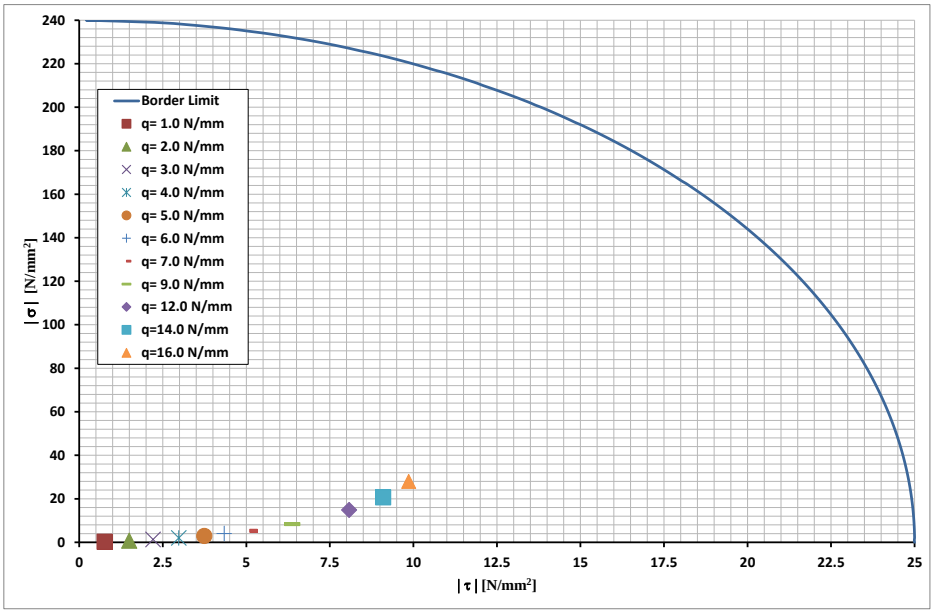

Figure A2. Case B1 – Actual stresses at buckling and failure envelope of "GFRP*5*" section.

CASE C1

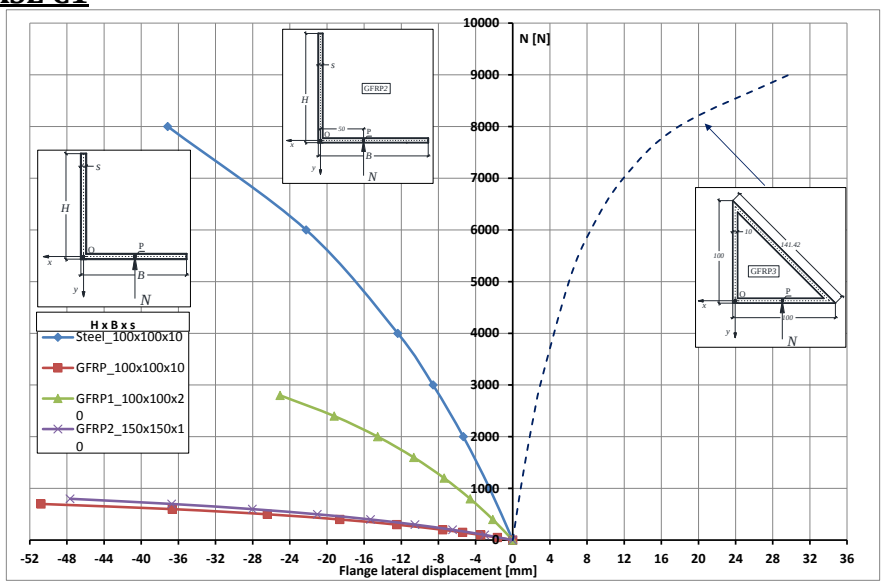

Figure A3a. Case C1 - Load *N* versus lateral displacements *u* of point P on the flange.

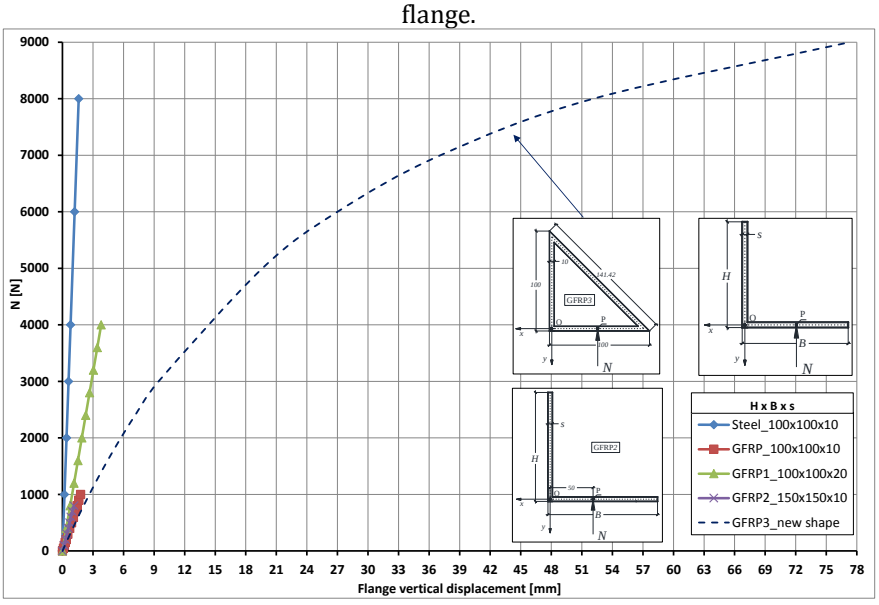

Figure A3b. Case C1 - Load *N* versus vertical displacements *v* of point P on the flange.

CASE C2

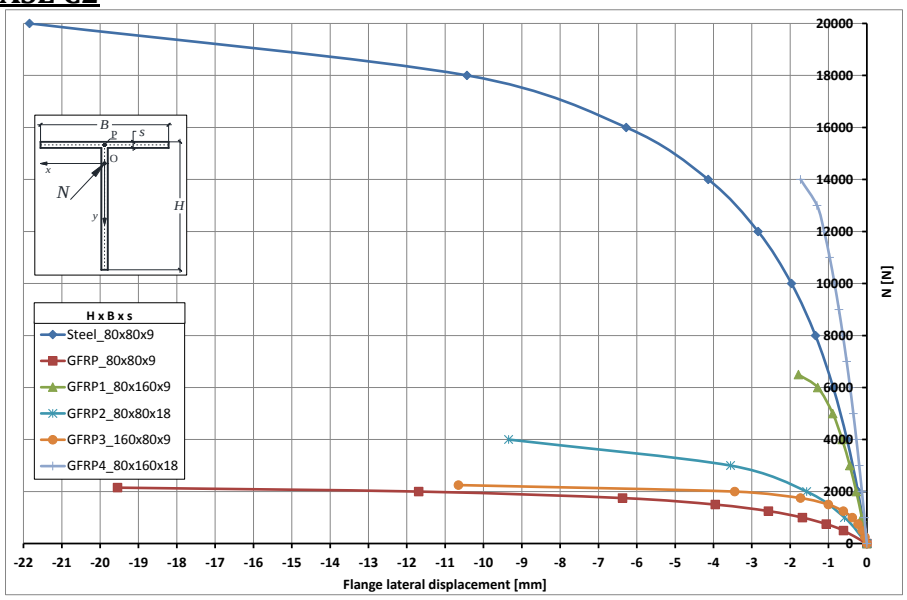

Figure A4a. Case C2 - Load N vs Flange lateral displacements u of point P curve.

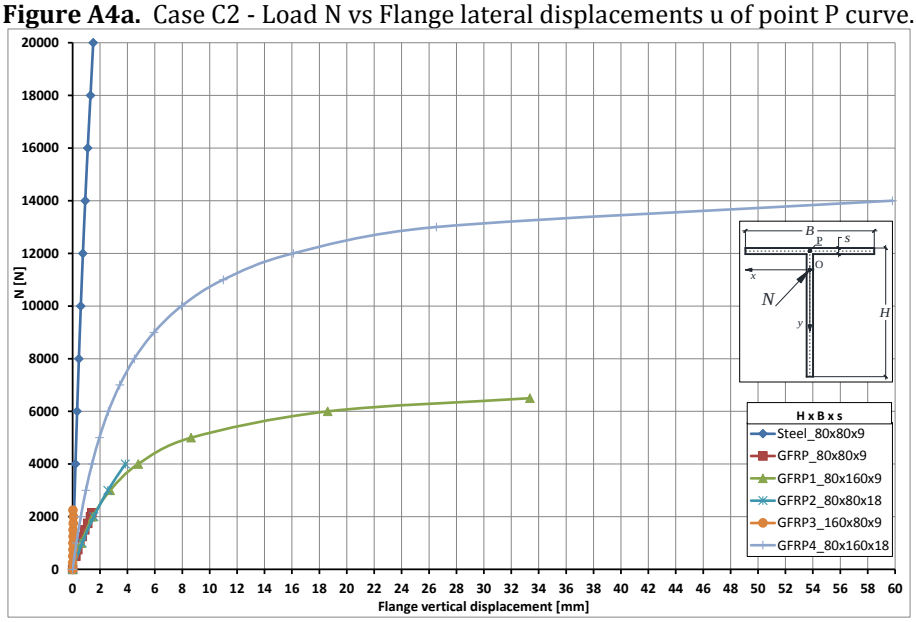

Figure A4b. Case C2 - Load *N* versus vertical displacements *v* of point Q on the flange.

CASE C3

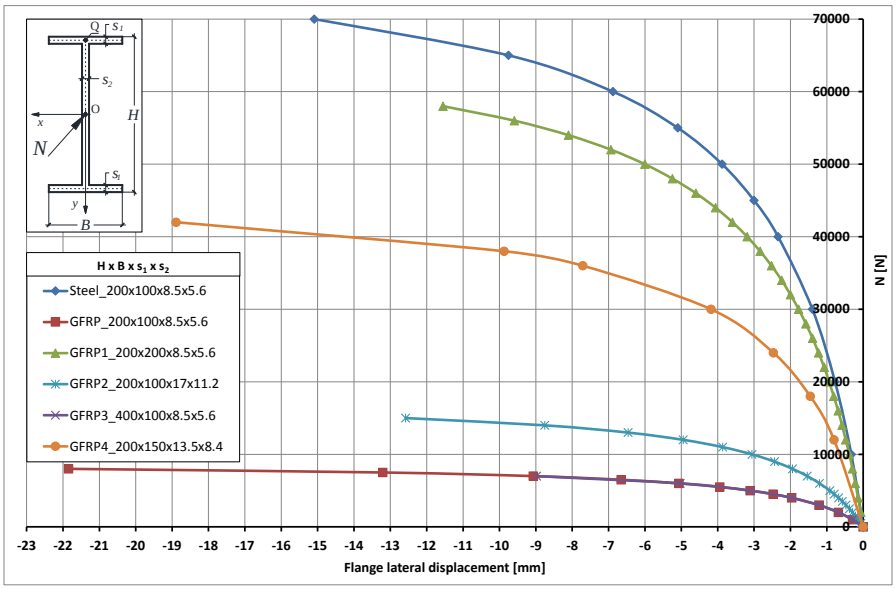

Figure A5. Case C3 - Load *N* versus lateral displacements *u* of point Q on the flange.

Simply supported beam

In Table A2 the results in terms of buckling loads and different GFRP cross section geometries relative to cases D1,D2,E1,F1,F2 and F3 are reported.

Table A2. Simply supported beams: cross sectional dimensions and pertinent buckling loads.

Case studied	**Cross sections** *dimension in mm*		**Load**^{crit}	$\frac{L^{crit}_{GFRPi}}{L^{crit}_{GFRP}}$	$\frac{V_{GFRPi}}{V_{GFRP}}$	η
		(H x B x s)	**F^{crit}**			
			[kN]	**[-]**	**[-]**	**[-]**
D1 (T-)	Steel	(80 x 80 x 9)	16.00	-	-	-
	GFRP	(80 x 80 x 9)	1.00	1.00	1.00	1.00
	GFRP*1*	(80 x 80 x 18)	3.80	3.80	1.88	2.02
	GFRP*2*	(160 x 80 x 9)	1.20	1.20	2.94	0.41
	GFRP*3*	(80 x 80 x 27)	5.60	5.60	2.64	2.12
	GFRP*4*	(120 x 80 x 13.5)	3.20	3.20	1.85	1.73
	GFRP*5*	(80x 120 x 9)	1.40	1.40	1.26	1.11
	GFRP*6*	(80 x 120 x 13.5)	4.00	4'00	1.85	2.16
		(H x B x s_1 x s_2)	**F^{crit}**			
			[kN]	**[-]**	**[-]**	**[-]**
D2 (I-)	Steel	(200 x 100 x 8.5 x 5.6)	40.00	-	-	-
	GFRP	(200 x 100 x 8.5 x 5.6)	4.00	1.00	1.00	1.00
	GFRP*1*	(200 x 100 x 17 x 11.2)	15.00	3.75	1.93	1.94
	GFRP*2*	(400 x 100 x 8.5 x 5.6)	6.50	1.63	1.41	1.16
	GFRP*3*	(200 x 100 x 25.5 x 16.8)	33.00	8.25	2.79	2.96
	GFRP*4*	(200 x 200 x 8.5 x 5.6)	16.00	4.00	1.62	2.46
	GFRP*5*	(200 x 200 x 17 x 11.2)	56.00	14.00	3.18	4.41

follow…

continue…

Case studied		**Cross sections** *dimension in mm*	**Load^{crit}**	$\frac{L^{crit}_{GFRPi}}{L^{crit}_{GFRP}}$	$\frac{V_{GFRPi}}{V_{GFRP}}$	η
		(H x B x s)	**F^{crit}**			
			[kN]	**[-]**	**[-]**	**[-]**
	Steel	(100 x 100 x 8)	60.00	-	-	-
D3	GFRP	(100 x 100 x 8)	5.60	1.00	1.00	1.00
(Box)	GFRP*1*	(100 x 100 x 16)	17.00	3.04	1.83	1.66
	GFRP*2*	(100 x 200 x 8)	9.00	1.61	1.54	1.04
	GFRP*3*	(200 x 100 x 8)	13.00	2.32	1.54	1.50
	GFRP*4*	(200 x 200 x 10)	32.50	5.80	2.58	2.25
		(H x B x s_1 x s_2)	**q^{crit}**			
			[N/mm]	**[-]**	**[-]**	**[-]**
	Steel	(200 x 100 x 8.5 x 5.6)	35.00	-	-	-
E1 (I-)	GFRP	(200 x 100 x 8.5 x 5.6)	3.00	1.00	1.00	1.00
	GFRP*1*	(200 x 100 x 17 x 11.2)	9.00	3.00	1.93	1.55
	GFRP*2*	(400 x 100 x 8.5 x 5.6)	7.00	2.33	1.41	1.65
	GFRP*3*	(200 x 100 x 25.5 x 16.8)	20.00	6.67	2.79	2.39
	GFRP*4*	(200 x 200 x 8.5 x 5.6)	14.00	4.66	1.62	2.87
	GFRP*5*	(200 x 200 x 17 x 11.2)	52.00	17.33	3.18	5.45
		(H x B x s)	**N^{crit}**			
			[kN]	**[-]**	**[-]**	**[-]**
F1 (L-)	Steel	(100 x 100 x 10)	140.00	-	-	-
	GFRP	(100 x 100 x 10)	15.00	1.00	1.00	1.00
	GFRP*1*	(100 x 100 x 20)	30.00	2.00	2.00	1.00
	GFRP*2*	(200 x 200 x 10)	35.00	2.33	2.00	1.17

follow…

continue…

Case studied		**Cross sections** *dimension in mm*	**Load^{crit}**	$\frac{L^{crit}_{GFRPi}}{L^{crit}_{GFRP}}$	$\frac{V_{GFRPi}}{V_{GFRP}}$	η
		(H x B x s)	**N^{crit}**			
			[kN]	**[-]**	**[-]**	**[-]**
F1 (L-)	Steel	(100 x 100 x 10)	140.00	-	-	-
	GFRP	(100 x 100 x 10)	15.00	1.00	1.00	1.00
	GFRP*1*	(100 x 100 x 20)	30.00	2.00	2.00	1.00
	GFRP*2*	(200 x 200 x 10)	35.00	2.33	2.00	1.17
		(H x B x s)	**N^{crit}**			
			[kN]	**[-]**	**[-]**	**[-]**
F2 (T-)	Steel	(80 x 80 x 9)	72.00	-	-	-
	GFRP	(80 x 80 x 9)	9.00	1.00	1.00	1.00
	GFRP*1*	(80 x 160 x 9)	24.00	2.67	1.53	1.75
	GFRP*2*	(80 x 80 x 18)	18.00	2.00	1.88	1.06
	GFRP*3*	(160 x 80 x 9)	9.00	1.00	1.53	0.65
	GFRP*4*	(80 x 160 x 18)	48.00	5.33	2.94	1.81
		(H x B x s_1 x s_2)	**N^{crit}**			
			[kN]	**[-]**	**[-]**	**[-]**
F3 (I-)	Steel	(200 x 100 x 8.5 x 5.6)	240.00	-	-	-
	GFRP	(200 x 100 x 8.5 x 5.6)	26.00	1.00	1.00	1.00
	GFRP*1*	(200 x 200 x 8.5 x 5.6)	220.00	8.46	1.62	5.21
	GFRP*2*	(200 x 100 x 17 x 11.2)	60.00	2.31	1.93	1.20
	GFRP*3*	(400 x 100 x 8.5 x 5.6)	30.00	1.15	1.41	0.82
	GFRP*4*	(200 x 150 x 12.75 x 8.4)	160.00	6.15	1.94	3.17

CASE D1

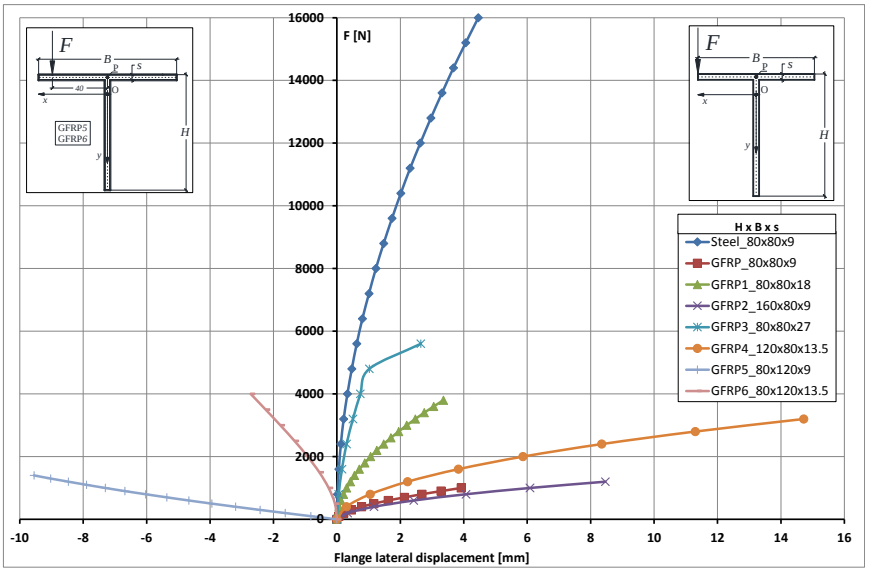

Figure A6a. Case D1 - Load *F* versus lateral displacements *u* of point P on the flange.

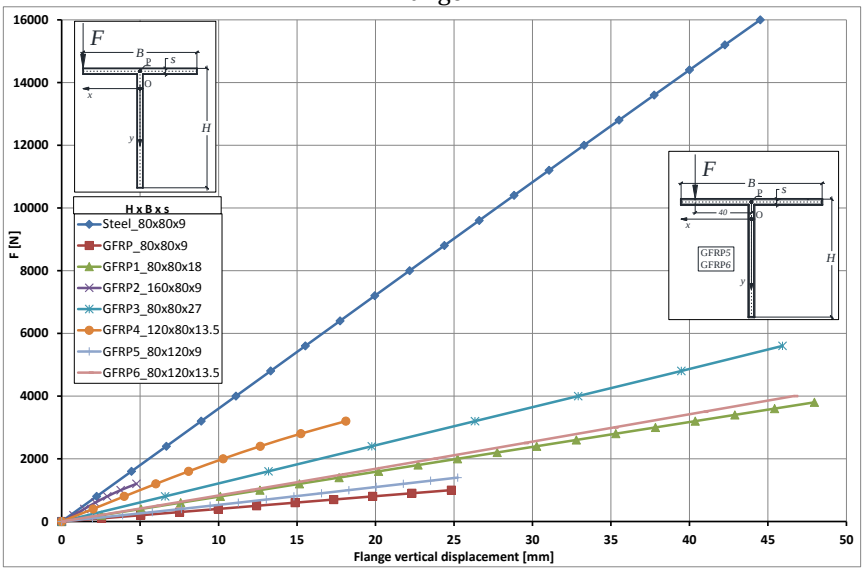

Figure A6b. Case D1 - Load *F* versus vertical displacements *v* of point P on the flange.

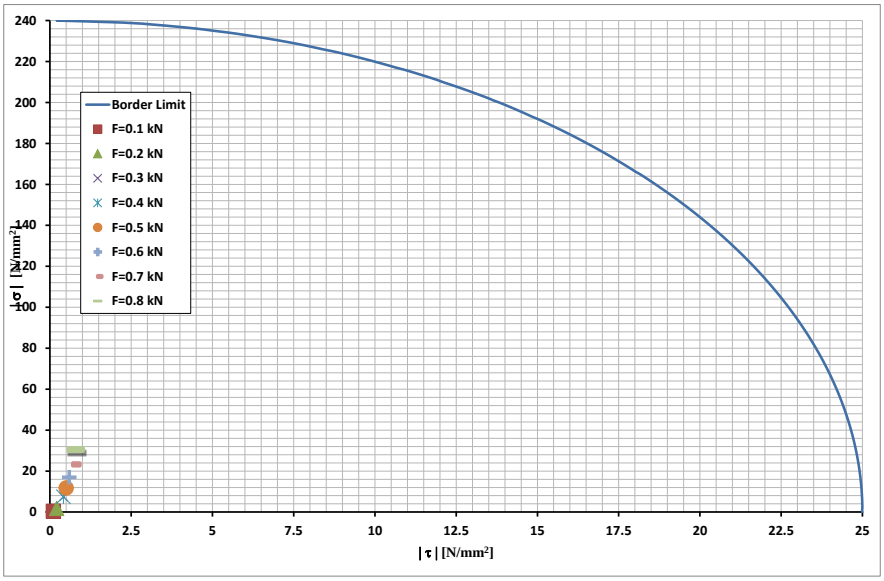

Figure A7. Case D1 – Actual stresses at buckling and failure envelope of section "GFRP3" .

CASE D2

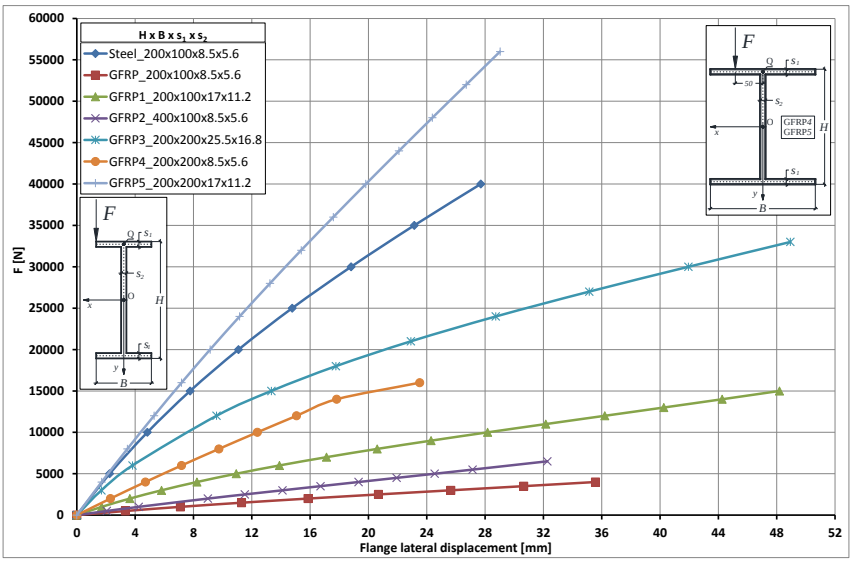

Figure A8a. Case D2 - Load *F* versus lateral displacements *u* of point Q on the flange.

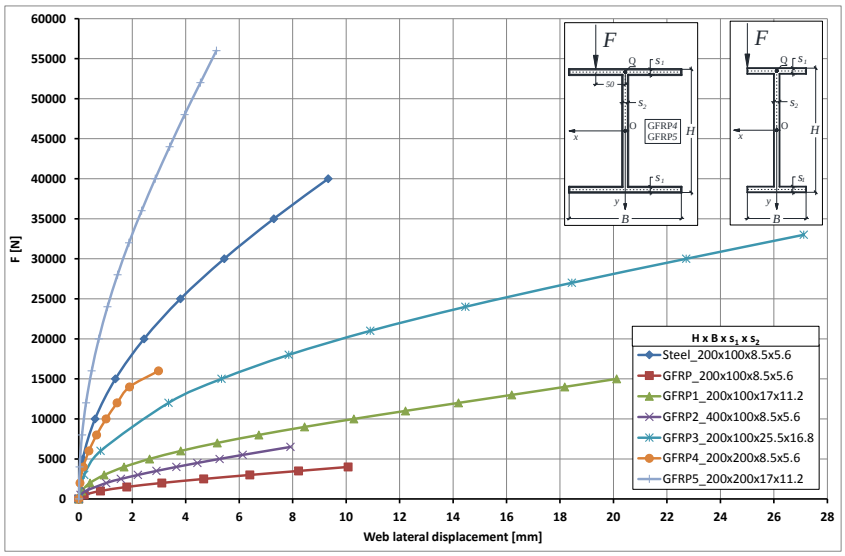

Figure A8b. Case D2 - Load F versus lateral displacements u of point P on the web.

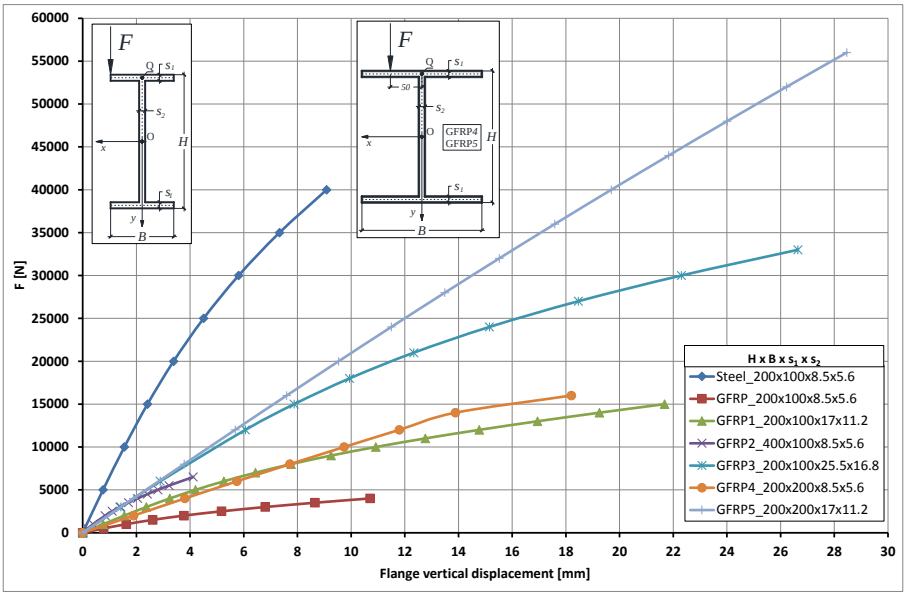

Figure A8c. Case D2 - Load *F* versus vertical displacements *v* of point Q on the flange.

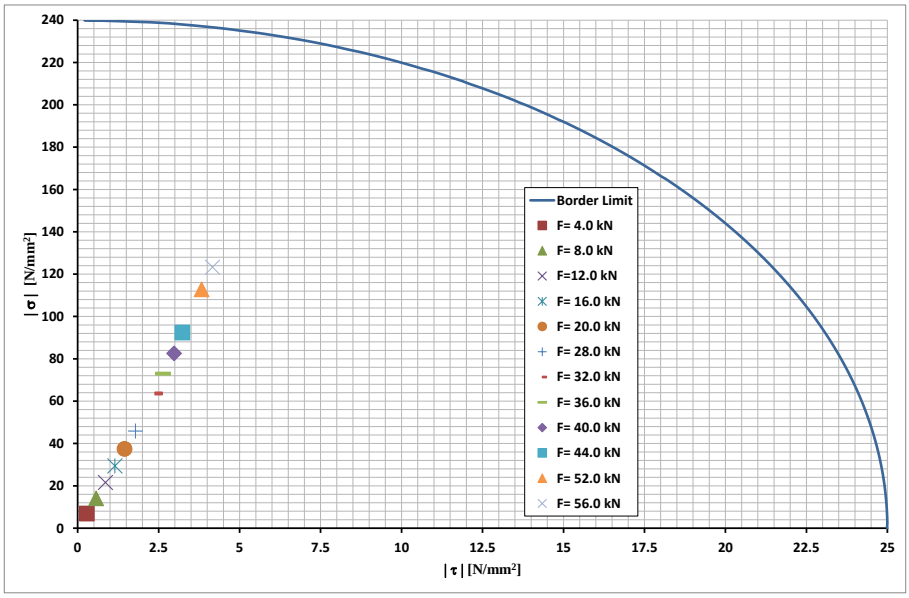

Figure A9. Case D2 – Actual stresses before buckling and failure envelope od "GFRP5" section.

CASE D3

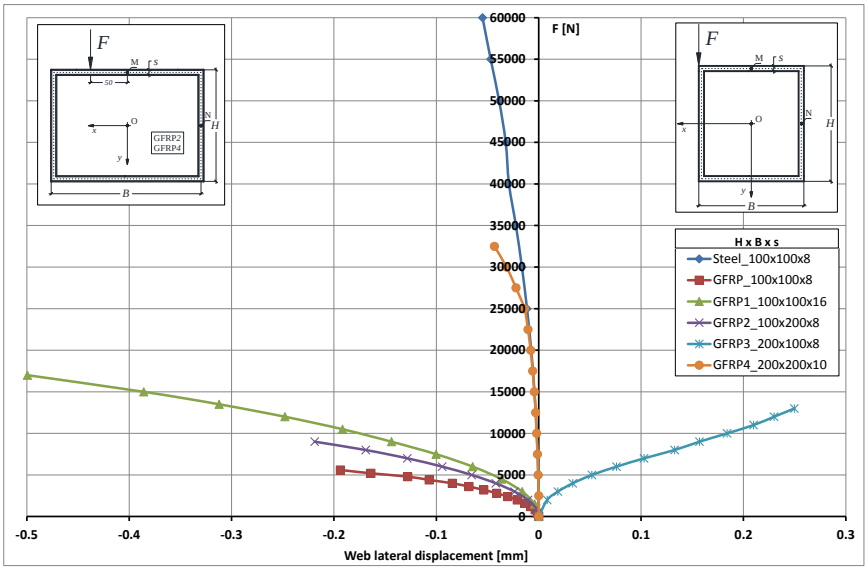

Figure A10a. Case D3 - Load *F* versus lateral displacements *u* of point P on the right web.

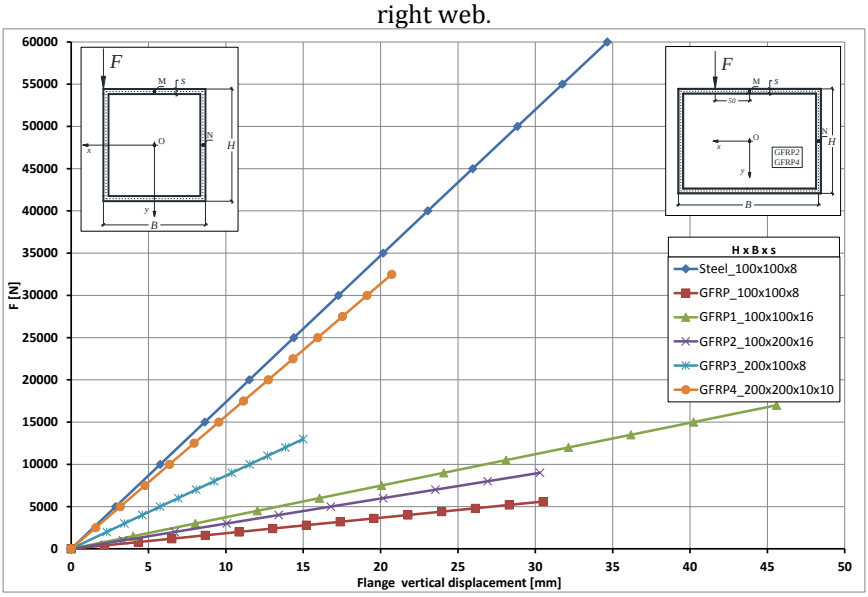

Figure A10b. Case D3 - Load *F* versus lateral displacements *u* of point P on the web.

CASE E1

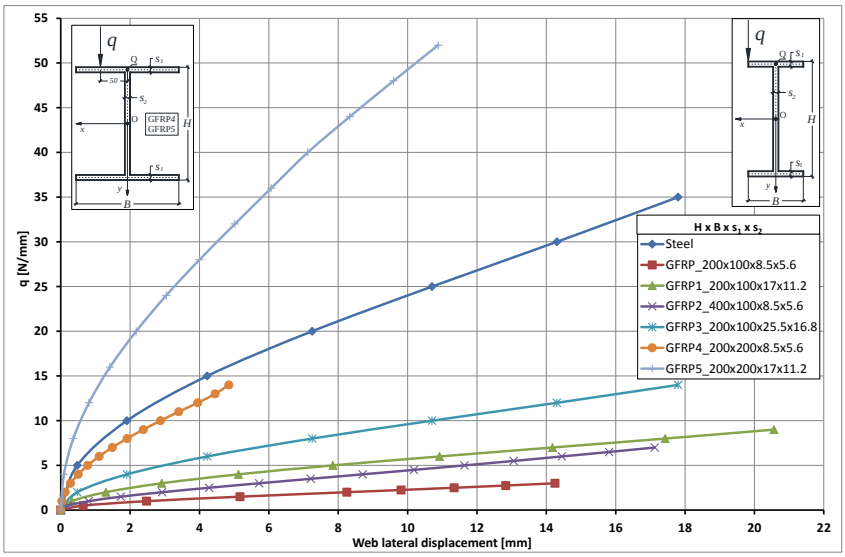

Figure A11a. Case E1 - Load *q* versus lateral displacements *u* of point O on the web.

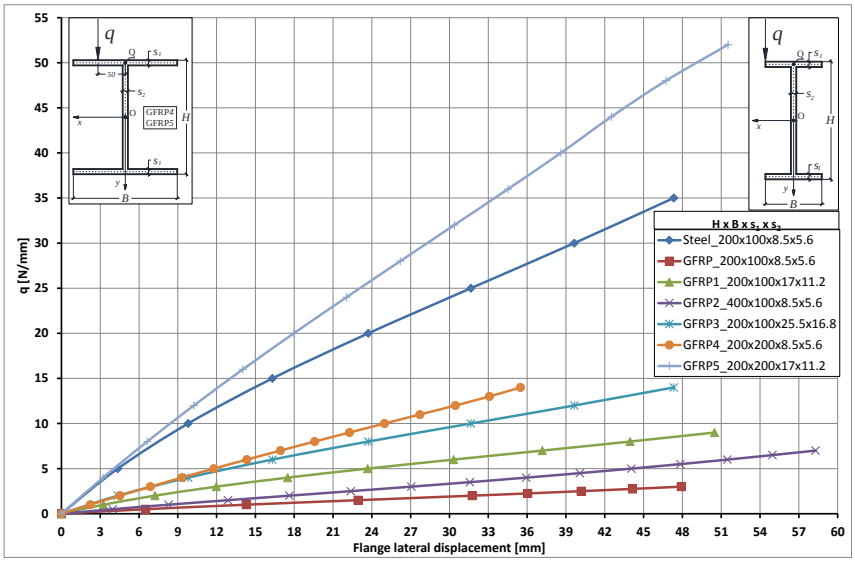

Figure A11b. Case E1 - Load q versus lateral displacements u of point Q on the flange.

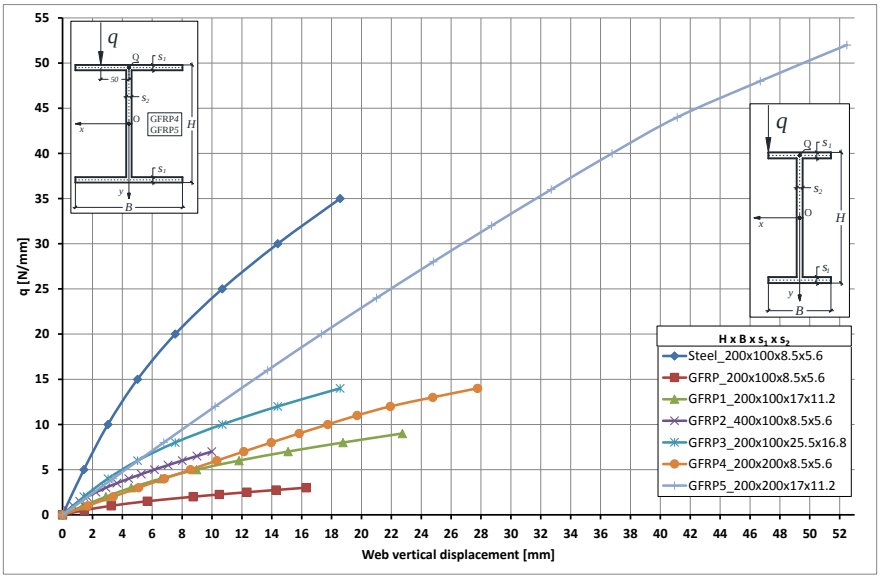

Figure A11c. Case E1 - Load *q* versus vertical displacements *v* of point O on the web.

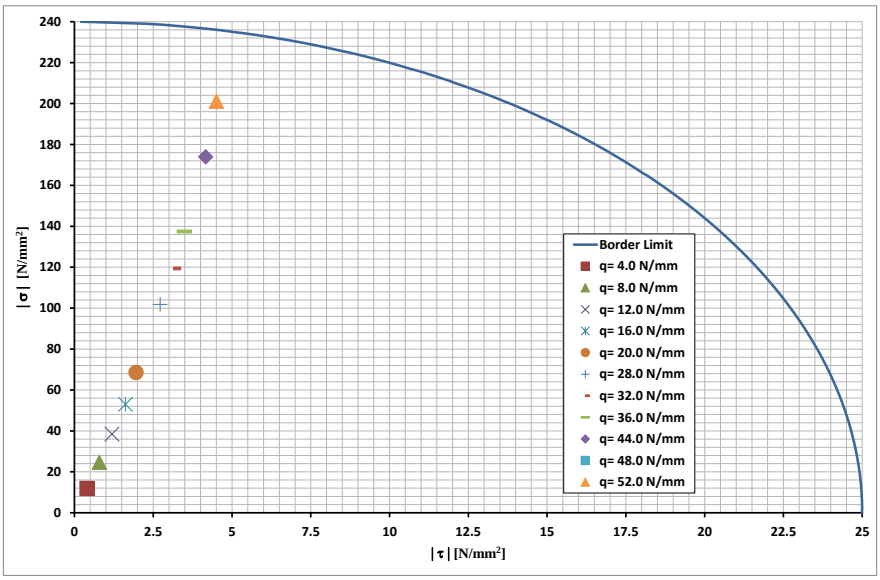

Figure A12. Case E1 – Actual stress at buckling and the failure envelope of the "GFRP*5*" section.

CASE F1

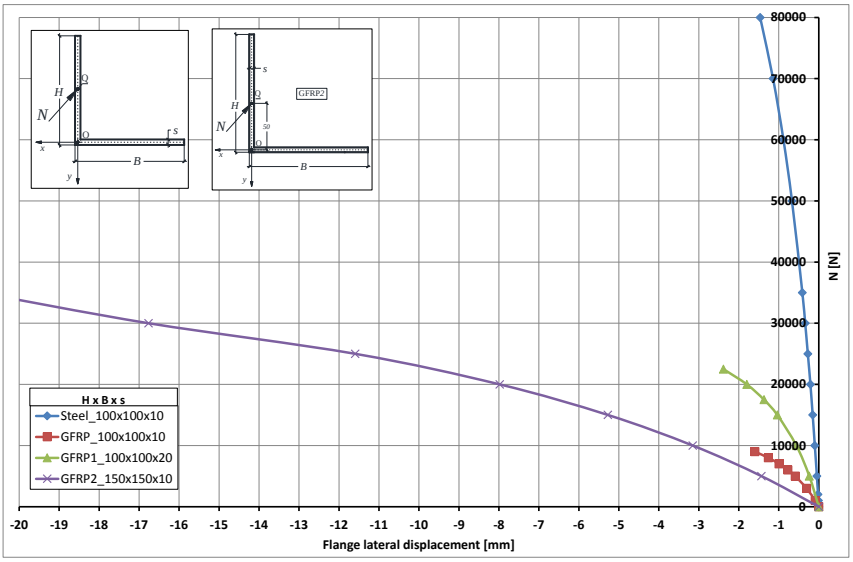

Figure A13a. Case F1 - Load *N* versus lateral displacements *u* of point Q on the flange.

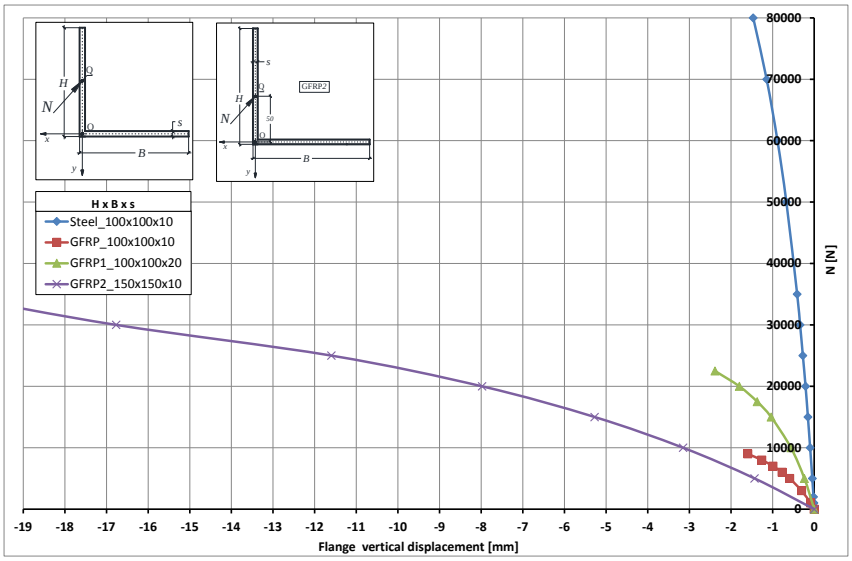

Figure A13b. Case F1 - Load N versus vertical displacements v of point Q on the flange.

CASE F2

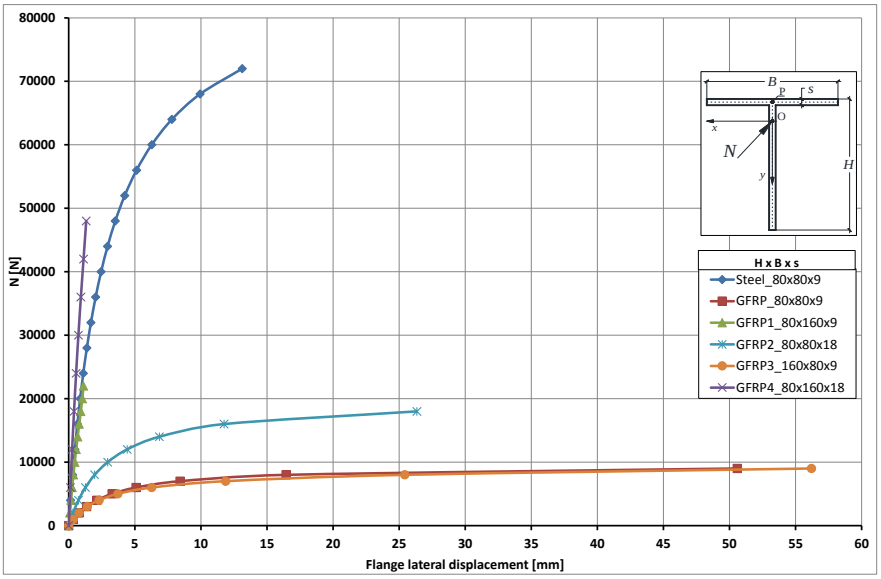

Figure A14a. Case F2 - Load *N* versus lateral displacements *u* of point P on the flange.

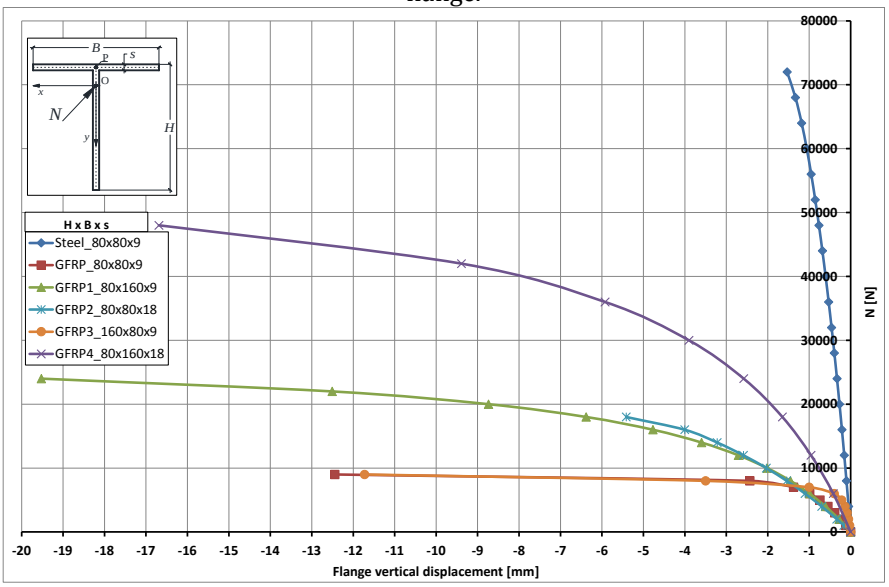

Figure A14b. Case F2 - Load *N* versus vertical displacements *v* of point P on the flange.

CASE F3

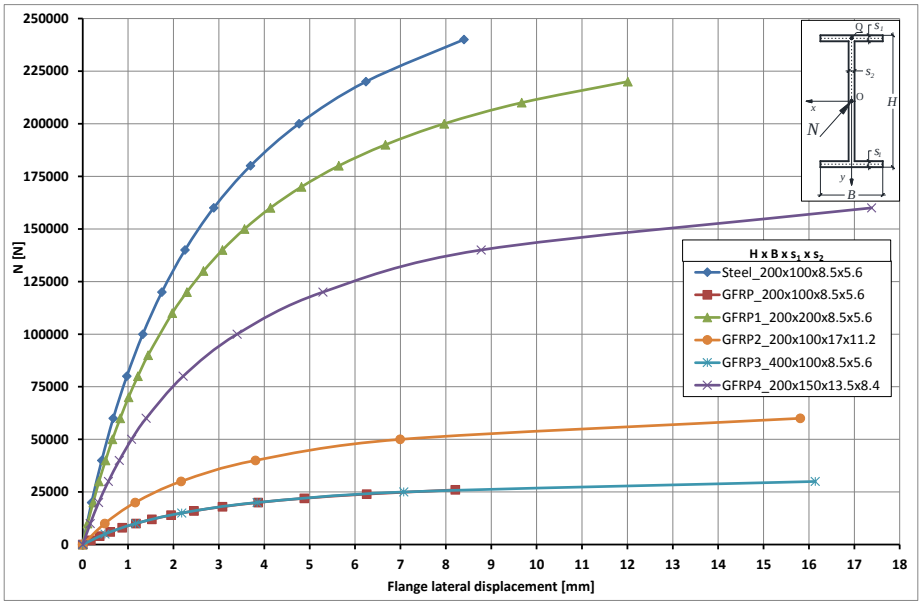

Figure A15. Case F3 - Load *N* versus lateral displacements *u* of point Q on the flange.

REFERENCES

INTRODUCTION

[1] Advisory Committee on Technical Recommendations for Constructions, Italian National Research Council (2007) CNR DT205/2007. Guide for the Design and Construction of Structures made of FRP Pultruded Elements.

[2] Canadian Standard Association (2002) CAN/CSA S806_02-2002. Design and Construction of Building Components with fibre-reinforced polymers. Rexdale, Canada.

[3] JSCE (1997). Recommendation for Design and Construction of Concrete Structures using Continuous Fiber Reinforcing Materials. Japan Society of Civil Engineering.

[4] American Concrete Institute (2006) ACI 440.1R-06-2006. Guide for the Design and Construction of Concrete Reinforced with FRP Bars.

[5] Halliwell S M. Polymer composites in construction, BRE/DETR UK, BR405, Building Research Establishment, UK, 2000.

[6] Borri A, Castori G, Corradi M, Speranzini E. Durability analysis for FRP and SRG composites in civil applications. Key Engineering Materials (2015): 624, 421-428.

[7] Hollaway L.C. Applications of fibre-reinforced polymer composite materials. In ICE manual of construction materials: Polymers and Polymer Fibre Composites. London: Thomas Telford Limited, 2010, 109–127.

[8] Bank L.C. Composites for Construction—Structural Design with FRP Materials. New Jersey: John Wiley & Sons, 2006.

[9] Zhao L, Burguono R, Rovere H L, Seible F, Karbhari V. Preliminary evaluation of the hybrid tube bridge system. Technical Report No TR-2000/4–59AO032, California Department of Transportation. 2000.

[10] Ascione F. Modellazione di Giuti di FRP. PhD thesis, Tor Vergata University, 2008.

[11] Eurocomp design code and handbook. Structural design of polymer composites. The European Structural Polymeric Composites Group; 1996.ISBN 0419194509.

[12] European Committee for Standardization (CEN). EN 13706: Reinforced plastics composites – Specifications for pultruded profiles. Part 1: Designation; Part 2: Methods of test and general requirements; Part 3: Specific requirements, Brussels: CEN; 2002.

[13] Technical Document CNR-DT 205/2007. Guide for the design and construction of structures made of FRP pultruded elements. Rome: Italian National Research Council (CNR); 2008.

[14] Mosallam A. S., Design guide for FRP composite connections. Manuals of Practice (MOP) 102. American Society of Civil Engineers (ASCE); 2011. ISBN9780784406120: 624.

[15] Methods of test and general requirements; Part 3: Specific requirements. Brussels: CEN; 2002.

[16] Lofrano, E., Paolone, A. & Ruta, G. (2013) A numerical approach for the stability analysis of open thin-walled beams. Mechanics Research Communications, 48, 76–86.

[17] Pignataro, M., Ruta, G., Rizzi, N. & Varano, V. (2009) Effects of warping constraints and lateral restraint on the buckling of thin-walled frames. ASME 2009 International Mechanical Engineering Congress and Exposition, Volume 10: Mechanical Systems and Control, Parts A and B, Lake Buena Vista, Florida, USA, November 13–19, 2009

[18] Chataigner S, Caron J F, Diaz A, Aubagnac C, Benzarti K. Non-linear failure criteria for a double lap bonded joint. International Journal of Adhesion & Adhesives 2010; 30: 10-20

[19] Cognard J Y, Devaux H, Sohier L. Numerical analysis and optimization of cylindrical adhesive joints under tensile loads. International Journal of Adhesion & Adhesives 2010; 30: 706-719

[20] Freddi F, Sacco E. Mortar joints influence in debonding of masonry element strengthened with FRP. Key Engineering Materials 2015; 624: 197-204

[21] Carrara P, Freddi F. Statistical assessment of a design formula for the debonding resistance of FRP reinforcements externally glued on masonry units. Composites Part B 2014; 66: 65-82.

[22] D'Aniello M, Portioli F, Landolfo R. Lap shear tests on hot-driven steel riveted connections strengthened by means of C-FRPS. Composites Part B 2014; 59C: 140-152.

[23] Ascione F. Adhesive lap-joints: a micro-scale numerical investigation. Mechanics Research Communications 2010; 37:169-172.

[24] Ascione F. A preliminary numerical and experimental investigation on the shear stress distribution on multi-row bolted FRP joints. Mechanics Research Communications 2010; 37:164-168.

PART I

[25] Vlasov, V.Z. (1961) *Thin-walled Elastic Beams*. 2nd ed. Jerusalem (Israel): Israel Program for Scientific Translation.

[26] Gjelsvik, A. (1981) The Theory of Thin-walled Bars. New York: John Wiley and Sons Inc.

[27] Bauld, N.R. & Tzeng, L.S. (1984) A Vlasov theory for fiber-reinforced beams with thin-walled open cross section. International Journal of Solids and Structures, 20(3), 277–97.

[28] Davalos, J.F., Salim, H.A., Qiao, P. & Lopez-Anido, R. (1996) Analysis and design of pultruded FRP shapes under bending. Composites: Part B, 27B, 295–305.

[29] Ascione, L., Feo, L. & Mancusi, G. (2000) On the statical behavior of fiber-reinforced polymer thin-walled beams. Composites: Part B, 31B, 643–654.

[30] Feo, L. & Mancusi, G. (2010) Modeling shear deformability of thin-walled composite beams with open cross-section. Mechanics Research Communications, 37, 320–325.

[31] Lee, J. & Lee, S. (2004) Flexural-torsional behaviour of thin walled composite beams. Thin-walled Struct., 42(9), 1293–1305.

[32] Vo, T.P. & Lee, J. (2008) Flexural-torsional behaviour of thin-walled composite box beams using shear-deformable beam theory. Engineering Structures, 30, 1958–1968.

[33] Vo, T.P. & Lee, J. (2010) Geometrically nonlinear theory of thin-walled composite box beams using shear-deformable beam theory. International Journal of Mechanical Sciences, 52, 65–74.

[34] Mancusi, G. & Feo, L. (2013) Non-linear pre-buckling behavior of shear deformable thin-walled composite beams with open cross-section. Composites: Part B, 47, 379–390.

[35] Ascione, L., Berardi, V.P., Giordano, A. & Spadea, S. (2013) Buckling failure modes of FRP thin-walled beams. Composites: Part B, 47, 357–364.

[36] Ascione, L., Berardi, V.P., Giordano, A. & Spadea, S. (2013) Local buckling behavior of FRP thin-walled beams: A mechanical model. Composite Structures, 98, 111–120.

[37] Ascione, L., Giordano, A. & Spadea, S. (2001) Lateral buckling of pultruded FRP beams. Composites Part B, 42, 819–824.

[38] Mosallam, A.S., Elsadek, A.A. & Pul, S. (2009) Semi-rigid behaviour of web-flange junctions of open-web pultruded composites. Proceedings of the International Conference on FRP Composites 2009, San Francisco, California.

[39] Feo, L, Mosallam, A.S. & Penna R. (2013) Mechanical behavior of web-flange junctions of thin-walled pultruded I-profiles: An experimental and numerical evaluation. Composites: Part B, 48, 18–39.

[40] Lee, J. & Kim, S. (2001 Flexural-torsional buckling of thin-walled I-section composites. Computers and Structures, 79(10), 987–95.

[41] Brooks, R.J. & Turvey, G.J. (1995) Lateral buckling of pultruded GRP I-section cantilever. Composite Structures, 32, 203–15.

[42] Cortinez, V.H. & Piovan, M.T. (2006) Stability of composite thin-walled beams with shear deformability. Computers and Structures, 84, 978–990.

[43] Ascione, F. (2014) Influence of initial geometric imperfections in the lateral buckling problem of thin walled pultruded GFRP I-profiles. Composite Structures doi: 10.1016/j.compstruct.2014.02.002.

[44] Mancusi G, Ascione F, Lamberti M. Pre-buckling behavior of composite beams: A mechanical innovative approach. Composite Structures (2014), 117: 396–410.

PART II

[45] Kollár LP, Springer GS. Mechanics of composites structures. Cambridge University Press; 2003.

[46] Barbero EJ. Introduction to composite material design. Philadelphia: Taylor & Francis; 1998.

[47] Ascione L, Berardi VP, Giordano A, Spadea S. Local buckling behavior of FRP thin-walled beams: A mechanical model. Composite Structures (2013), 98: 111-120.

[48] Ascione L, Berardi VP, Giordano A, Spadea S. Macro-scale analysis of local and global buckling behavior of T and C composite sections. Mechanics Research Communications (2014), 58: 105-111.

[49] Ascione L, Berardi VP, Giordano A, Spadea S. Pre-buckling imperfection sensitivity of pultruded FRP profiles Composites Part B Engineering (2015) Composites Part B: Engineering, 72: 206-212.

[50] Ascione, F. & Mancusi, G. (2013) The influence of the web-flange junction stiffness on the mechanical behavior of thin-walled pultruded beams. Composites: Part B, 55, 599–606.

[51] Cocheteau N, Maurel-Pantel A, Lebon F, Rosu I, Prieto E, Ait-Zaid S, Savin de Larclause I, Salaun Y. Process parameters influence on mechanical strength of direct bonded surfaces for both materials: silica and Zerodur® glasses Journal of Adhesion Science and Technology (2014), 28 (10): 915-934.

[52] Turvey GJ, Zhang Y. A computational and experimental analysis of buckling, post buckling and initial failure of pultruded GRP columns. Computers and Structures (2006), 84:1527–1537.

[53] Lamberti M, Ascione F , Maurel-Pantel A, Lebon F. Influence of web/Flange reinforcement on the GFRP bonded beams mechanical response: A comparion with experimental results and a numerical prediction. Composite Structures 2016; 147: 247-259.

[54] Ascione F , Mancusi G, Spadea S, Lamberti M, Lebon F, Maurel-Pantel A. On the flexural behavior of GFRP beams obtained by bonding simple panels: an experimental investigation. Composite Structures 2015; 131: 55-65.